HAL
open science

# Analyse structurales de pseudo-substrats Gap/Si et d'hétérostructures CIGS/GaP/Si pour des applications photovoltaïques

Ang Zhou

## To cite this version:

Ang Zhou. Analyse structurales de pseudo-substrats Gap/Si et d'hétérostructures CIGS/GaP/Si pour des applications photovoltaïques. Matériaux. INSA de Rennes, 2019. Français. NNT : 2019ISAR0027 . tel-02924619

**HAL Id: tel-02924619**

**https://theses.hal.science/tel-02924619**

Submitted on 28 Aug 2020

**HAL** is a multi-disciplinary open access archive for the deposit and dissemination of scientific research documents, whether they are published or not. The documents may come from teaching and research institutions in France or abroad, or from public or private research centers.

L'archive ouverte pluridisciplinaire **HAL**, est destinée au dépôt et à la diffusion de documents scientifiques de niveau recherche, publiés ou non, émanant des établissements d'enseignement et de recherche français ou étrangers, des laboratoires publics ou privés.

UNIVERSITE BRETAGNE LOIRE / MATIERE MOLECULES ET MATERIAUX

INSA RENNES

# THESE DE DOCTORAT DE

L'INSTITUT NATIONAL DES SCIENCES APPLIQUEES RENNES
COMUE UNIVERSITE BRETAGNE LOIRE

ECOLE DOCTORALE N° 596
*Matière, Molécules, Matériaux*
Spécialité : « *Sciences des Matériaux* »

Par
**Ang ZHOU**

# Analyses structurales de pseudo-substrats GaP/Si et d'hétérostructures CIGS/GaP/Si pour des applications photovoltaïques

**Thèse présentée et soutenue à Rennes, le « 13/12/2019 »**
**Unité de recherche : Institut FOTON – UMR 6082**
**Thèse N° : D19-35 / 19ISAR 35**

**Rapporteurs avant soutenance :**

**Stéphanie Escoubas**
MCF HDR IM2NP Aix Marseille Université

**Laurent Le Brizoual**
Professeur IETR Université de Rennes 1

**Composition du Jury :**

**Stéphanie Escoubas**
MCF-HDR IM2NP Aix Marseille Université / Rapportrice
**Laurent Le Brizoual**
Professeur IETR Université de Rennes 1 / Rapporteur
**Daniel Lincot**
Directeur de recherche IPVF CNRS / Président
**Nicolas Barreau**
MCF-HDR IMN Université de Nantes / Examinateur
**Olivier Durand**
Professeur Institut FOTON INSA-Rennes / Directeur de thèse
**Antoine Létoublon**
MCF Institut FOTON INSA-Rennes / Co-encadrant

**Intitulé de la thèse :**

Analyses structurales de pseudo-substrats GaP/Si et d'hétérostructures

CIGS/GaP/Si pour des applications photovoltaïques

**Ang ZHOU**

**En partenariat avec :**

*Document protégé par les droits d'auteur*

UNIVERSITE BRETAGNE LOIRE / MATIERE MOLECULES ET MATERIAUX

INSA RENNES

# Acknowledgement

Firstly, I would like to express my deep acknowledgement to my supervisor Prof. DURAND Olivier and my second supervisor Dr. LÉTOUBLON Antoine. I am appreciated to have the opportunity to perform my Ph.D. project under their guidance, advices and pedagogy. In the long trip, their solid knowledge has led me through the mist of ignorantness and their encouragement has carried me out the sea of vastness.

I want to thank ESCOUBAS Stephanie, LE BRIZOUAL Laurent, LINCOT Daniel and BARREAU Nicolas for being the members of my jury of defense, for their time, their patience and their valuable opinions during the defense. I also want to specially thank ESCOUBAS Stephanie and LE BRIZOUAL Laurent for reviewing my thesis documents.

I'm thankful to members of epitaxy group, CORNET Charles, ROHEL Tony, GAUTHERON-BERNARD Rozenn and others, for their help in the sample growth. My thanks also go to LE CORRE Alain, LÉGER Yoan, PEDESSEAU Laurent, TAVERNIER Karine, EVEN Jacky and all the other colleagues in our laboratory, for teaching me research skills and giving me selfless help in the work. I am appreciated to WANG Yanping, MICKAEL Da Silva, TREMBLAY Ronan, LUCCI Ida, BRÉVALLE Gaëlle, CHEN Lipin, LORENZO RUIZ Alejandro and all the other Ph.D. students, too. I have spent an unforgettable warm time with them.

Many collaborators contributed to this research. I have had the chance to cooperate with the members on the ID01 beamline at the European Synchrotron Radiation Facility, especially Tobias Tschulli, Gilbert Chahine, Vincent Favre- Nicolin and Joël Eymery. I also acknowledge Valérie Demange from ICSR for providing us the access to their X-ray Diffractometer. In particular I would like to thank BARREAU Nicolas from IMN for the EDX/(S)TEM images on the analysis of CIGS grown on GaP, Gilles Patriarche, Mounib Bahri, Ludovic Largeau from LPN for the beautiful TEM images on the analysis of GaP on Si.

Finally, I'm deeply indebted to my families for their selfless love and unconditional support throughout my whole life and my study.

# CONTENTS


..... I

**ANALYSES STRUCTURALES DE PSEUDO-SUBSTRATS GAP/SI ET D'HETEROSTRUCTURES CIGS/GAP/SI POUR DES APPLICATIONS PHOTOVOLTAÏQUES** ..... I

CONTENTS ..... III

LIST OF FIGURES ..... V

LIST OF ABBREVIATIONS ..... VIII

CHAPITRE 1. INTRODUCTION ..... 1

*1.1. Towards a better world ..... 2*

*1.2. Heteroepitaxy of GaP and Si ..... 3*

*1.3. Crystallographic defect ..... 6*

1.3.1. Point defects ..... 6

1.3.2. Line defects ..... 8

1.3.3. Planar defects ..... 8

1.3.4. Volume defects ..... 9

*1.4. Principle crystallographic defects in GaP/Si pseudo-substrate ..... 9*

1.4.1. Dislocation ..... 11

1.4.2. Microtwins ..... 13

1.4.3. Antiphase Domain ..... 14

1.4.4. Mosaic ..... 15

*1.5. The organization of the thesis ..... 16*

*References ..... 17*

CHAPITRE 2. GAP/SI EPITAXY AND CHARACTERIZATION TECHNIQUES ..... 26

*2.1. Epitaxy of the GaP/Si pseudo-substrate ..... 27*

2.1.1. Growth cluster UHV/CVD – MBE ..... 27

2.1.2. The preparation of Si wafers ..... 28

*2.2. X-ray diffraction characterization ..... 28*

2.2.1. X-ray diffraction setup ..... 29

2.2.2. Longitudinal scan ..... 31

2.2.3. Reciprocal Space Mapping ..... 35

2.2.4. Pole Figure ..... 40

2.2.5. Sub-Micrometer-Beam Scanning Synchrotron X-Ray Diffraction ..... 43

*2.3. Other Characterization Methods ..... 47*

2.3.1. Atomic Force Microscope ..... 47

2.3.2. Transmission electron microscope and Scanning Transmission electron microscope ..... 48

*References ..... 49*

CHAPITRE 3. SUB-MICROMETER-BEAM X-RAY DIFFRACTION ON GAP/SI PSEUDO-SUBSTRATE FOR LOCAL DISLOCATION DISTRIBUTIONS 54

*3.1. Previous structural optimization on GaP/Si pseudo-substrate* ..... *55*
3.1.1. Micro-twin quantification and corresponding growth condition optimization ..... 55
3.1.2. Anti-phase Domain quantification and corresponding growth condition optimization ..... 56
*3.2. Characterization of a 200 nm GaP/Si sample* ..... *60*
3.2.1. Sample growth and lab setup characterization ..... 60
3.2.2. Performance of K-Map ..... 61
3.2.3. Data processing ..... 64
3.2.4. The measurement resolution ..... 66
*3.3. The local structural characterization with sub-micrometer-beam X-ray diffraction* ..... *68*
*3.4. Other observation and discussion on the line profile of the scattering spot along Qy* ..... *73*
*3.5. Summary* ..... *80*
*References* ..... *81*
CHAPITRE 4. X-RAY DIFFRACTION CHARACTERIZATION ON THE CIGS GROWN ON GAP/SI PSEUDO-SUBSTRATE ..... 85
*4.1. CIGS on GaP/Si pseudo-substrate for photo-voltaic application* ..... *87*
*4.2. Characterization of the CIGS grown on GaP/Si pseudo substrate.* ..... *88*
4.2.1. CIGS structural description ..... 88
4.2.2. Sample preparation ..... 89
4.2.3. ω/2θ scans and reciprocal space mapping ..... 90
4.2.4. Epitaxy of CIGS on the GaP/Si platform. ..... 98
4.2.5. Study of the Pole figures ..... 100
*4.3. First try of CIGSe solar cell on the GaP/Si (001) platform* ..... *106*
*4.4. Summary* ..... *107*
*References* ..... *109*
CHAPITRE 5. GENERAL CONCLUSIONS AND PERSPECTIVE WORK ..... 113
*5.1. Summary and conclusions* ..... *113*
*5.2. Suggestions for future works* ..... *114*
*References* ..... *115*
APPENDICES ..... 116
***A1. Performance of PF scans for Microtwin (MT) quantification*** ..... *116*
RESUME DE THESE ..... 119

# LIST OF FIGURES

FIGURE 1-1 BAND GAP ENERGY (WAVELENGTH) VERSUS LATTICE CONSTANTS FOR SILICON AND MOST COMMON III-V SEMICONDUCTORS. ..... 4
FIGURE 1-2 A SCHEMATIC REPRESENTATION OF TYPICAL POINT DEFECTS IN THE LATTICE STRUCTURE. ..... 7
FIGURE 1-3 STACKING SEQUENCE OF HEXAGONAL CLOSE PACKED STRUCTURE (HCP) AND FACE CENTERED CUBIC STRUCTURE (FCC)... 8
FIGURE 1-4 A TEM IMAGE WHICH SHOW THE GRAIN BOUNDARIES IN CIGS GROWN ON MO/GLASS. [80] ..... 9
FIGURE 1-5 THE SKETCH OF THE LATTICE STRAIN OF GAP THIN LAYER ON A) NOMINAL AND B)VICINAL SI SUBSTRATE. [81] ..... 10
FIGURE 1-6 THE SKETCH OF THE A) EDGE DISLOCATION AND B) SCREW DISLOCATION. [91] ..... 12
FIGURE 1-7 A SKETCH OF 60° DISLOCATIONS IN HETEROEPITAXY LAYER ON VICINAL SUBSTRATE. [92] ..... 12
FIGURE 1-8 A SKETCH OF FOUR MICROTWINS IN GAP THIN LAYER ON VICINAL SI SUBSTRATE [87], AND GAP IN THE RECIPROCAL SPACE. STRONG, MEDIUM AND WEAK REFLECTIONS ARE LABELLED WITH BLACK, BLUE AND RED POINTS. MT-A AND MT-C ARE LABELLED WITH GREEN AND ORANGE ELLIPSOIDS. ..... 14
FIGURE 1-9 THE APD IN GAP EPITAXY LAYERS ON SILICON SUBSTRATES WITH MONO-ATOMIC STEPS. ..... 15
FIGURE 1-10 A SKETCH OF MOSAICS WITH LIMITED LATERAL COHERENCE LENGTH, TILT OR TWIST IN GAP HETEROEPITAXY LAYER ON SI SUBSTRATE. ..... 16
FIGURE 2-1 UHV/CVD-MBE CLUSTER IN FOTON FOR GAP/SI PSEUDO-SUBSTRATE EPITAXY. ..... 27
FIGURE 2-2 SCHEMATIC DIAGRAM OF THE LAB SETUP X-RAY DIFFRACTOMETER IN THE LOW-RESOLUTION MODE. ..... 30
FIGURE 2-3 SCHEMATIC DIAGRAM OF THE LAB SETUP X-RAY DIFFRACTOMETER IN THE HIGH-RESOLUTION MODE. ..... 30
FIGURE 2-4 GONIOMETER GEOMETRY OF THE XRD LAB SETUP WITH FOUR ROTATIONAL DEGREES OF FREEDOM. ..... 31
FIGURE 2-5 SCHEMATIC DIAGRAM OF Ω/2Θ LONGITUDINAL SCAN ..... 31
FIGURE 2-6 Ω/2Θ SCAN ON CIGS GROWN ON GAP/SI PSEUDO SUBSTRATE. ..... 34
FIGURE 2-7 2D RECIPROCAL SPACE AND EDWARD SPHERE DIAGRAM OF A SIMPLE CUBIC STRUCTURE CRYSTAL. ..... 36
FIGURE 2-8 SCHEMATIC DIAGRAM OF A) A NORMAL CRYSTAL PLANE FAMILY B) A CRYSTAL PLANE FAMILY A TILT OR C) WITH A DIFFERENT LATTICE CONSTANT, I.E. A STRAIN STATE. ..... 38
FIGURE 2-9 SCHEMATIC DIAGRAM OF RELATIONSHIP BETWEEN RSM AND CRYSTAL PLANE PARAMETERS DHKL AND TILT $\delta$. ..... 39
FIGURE 2-10 SPHERICAL PROJECTION OF THE {100} POLES OF A CUBIC CRYSTAL. ..... 40
FIGURE 2-11 EXAMPLE OF STEREOGRAPHIC PROJECTION OF A CUBIC CRYSTAL. ..... 41
FIGURE 2-12 EXAMPLE OF A POLE FIGURE. [19] ..... 42
FIGURE 2-13 EXAMPLE OF POLE FIGURE USING THE PLANE {111} FOR GAP/SI (6° MISCUT) PSEUDO-SUBSTRATE. ..... 43
FIGURE 2-14 SKETCH OF THE BEAMLINE ID01 DIFFRACTION EXPERIMENTAL SETUP. [48] ..... 47
FIGURE 2-15 SCHEMATIC DIAGRAM OF THE PHOTODIODE DETECTOR SYSTEM. ..... 48
FIGURE 3-1 POLES FIGURE IMAGE AROUND THE NOMINAL GAP (111) REFLECTION FOR THE S1477 140NM GAP/SI (001) 6° -OFF SAMPLE TOWARDS THE [110] DIRECTION. ..... 56
FIGURE 3-2 THE A) POLES FIGURE B) 5×5 MM2 AFM IMAGES OF A GAP/SI SAMPLE GROWN WITH THE OPTIMIZED CONDITION. ..... 56
FIGURE 3-3 EXAMPLE OF WILLIAMSON-HALL-LIKE PLOT. ..... 58
FIGURE 3-4 LABORATORY XRD RSM AROUND (A) 002 AND (B) 004 NEARLY SPECULAR REFLECTIONS FOR S1330, AND THEIR CORRESPONDING TRANSVERSE SCANS (C) AND (D). ..... 59

Figure 3-5 Cross-section STEM-BF images for the optimized GaP/Si growth (from ref [7] ). 60
Figure 3-6 (a)RSM image of (004) diffraction. (b) PF image (c) 5mm×5mm AFM image under tapping mode. (d) Cross-sectional (220) Dark-Field (DF) TEM image. The misfit dislocations are labelled with yellow arrows. 62
Figure 3-7 a) The experimental setup of the K-Map and b) the footprint of the X-ray beam for the (004). 63
Figure 3-8 Sketch of the corrected vertical resolution in a thin layer, broadened by the projection of the cross-section and the sample thickness. 63
Figure 3-9 The movement of the X-ray spot on the sample surface controlled by the nanomotor. 64
Figure 3-10 The resolution of Qz determined by the rotation of the diffraction vector. 67
Figure 3-11 Tilt mapping towards (a) the [-1-10] and (b) the [1-10] using the (004) Bragg reflection. (c) Tilt mapping towards the [1-10] direction for the (002) Bragg reflection which exhibits similar tilts with (b) (the shift along the X direction is due to imperfect alignment or drift between measurements). 69
Figure 3-12 (a)Local strain (%) (b) FWHM of the $Q_y$ profile (°) mapping on (004) Bragg reflection of Sample S1477, which is 200nm GaP on Si substrate with 6° -off towards the [-1-10] direction. 70
Figure 3-13 Three LBPs with neighborhood ranges equal to 1, 2 and 3. 71
Figure 3-14 (a) Local binary image extracted from the residual strain mapping (Figure 3-12 a). (b) Spatial frequency of the lines with high strain along [-1-10] (blue) and [1-10] (orange). 71
Figure 3-15 Sketch of the unparallel dislocations for the steps of the substrate (redrew based on figure 5(c) in ref [32]). 72
Figure 3-16 Spatial frequency of AFM image Figure 1(b) along [-1-10] (blue) and [1-10] (orange). 73
Figure 3-17 (a) The single-peak point CCD image with Ω = 40.40° for (004) Bragg reflection and (c) the corresponding transverse scan with 0.01° width. (b) The double-peak point CCD image with Ω = 40.40° for (004) Bragg reflection and (d) the corresponding transverse scan with 0.01° width. 74
Figure 3-18 Sketch of different modes in the diffraction image. 75
Figure 3-19 (a) The mode mapping for sample S1477. The red, white and green areas respond to "split", "shift" and "normal" modes respectively. (b) Tilt mapping towards [110] using the (004) Bragg reflection (i.e. Figure 3-11.b) and the overlapping contour lines base on (a), where the red lines labelled "split" areas and the white lines labelled "shift" areas. 76
Figure 3-20 (a) FWHM mapping of the main peak along $Q_y$ and (b) In-plane residual strain mapping with overlapped contour lines (red) of the "split" areas based on Figure 3-19(a). 77
Figure 3-21 The direct CCD images of seven sampling points shown in Figure 3-20 (a). 78
Figure 3-22 Hypothetical sketch of the mechanism related to the "split" area. 80
Figure 4-1 Tandem concept with CIGS top cell with selective contacts and Si bottom cell. 86
Figure 4-2 structural matching criteria for the epitaxial growth of wide gap chalcopyrite on GaP/Si. Adapted from S. Chichibu et. al. [2] 86
Figure 4-3 band offset criteria for the optimization of photovoltaic properties of the CIGS/Si tandem devices. Values extracted by IPVF from literature data[2]–[6], [7, p.], [8]. 87
Figure 4-4 The unit cell of CIGS. 88

Figure 4-5 Ω/2Θ XRD scans a) from sample S554 (90nm grown at 450°C) and b) from sample 597 (600nm GaP grown at 580°C). The red tick (resp. the blue one) gives the theoretical fully strained GaP Bragg peak position (resp. the theoretical fully relaxed one). ..... 89
Figure 4-6 Ω/2Θ scans with 2Θ ranged from 20° to 80° for sample 1743/Glass. ..... 91
Figure 4-7 Ω/2Θ scans with 2Θ ranged from 20° to 80° for sample 1743/S554, 1743/S597, 1744/S554 and 1744/S597. ..... 92
Figure 4-8 A selected area electron diffraction by TEM on 1743/S554. ..... 93
Figure 4-9 EDX cartography performed on the 1743/S554 sample, showing the atomic fraction of all the CIGS elements, in particular the In and Ga elements. ..... 94
Figure 4-10 Left: evolution of the CIGS lattice parameters with respect to x, according to ref [16], [17] and [29]. Right: variations of the corresponding XRD (008) and (004) Bragg peak positions with respect to x. The vertical lines correspond to the variation of x deduced from the atomic fractions measured by EDX. ..... 95
Figure 4-11 Ω/2Θ scans with 2Θ ranged a) from 25° to 35° and b) from 65° to 70° for sample 1743/S554, 1743/S597, 1744/S554 and 1744/S597. ..... 96
Figure 4-12 Ω/2Θ scans with 2Θ ranged from 65° to 70° for sample 1743/S554, 1744/S554 and GaP/Si pseudo-substrate before growth. ..... 97
Figure 4-13 Cross-sectional (220) Bright-Field (BF) TEM image of a CIGS sample grown on GaP/Si substrate. ..... 98
Figure 4-14 RSM image of CIGS (1 1 10) and GaP/Si (115) diffraction. ..... 99
Figure 4-15 a) Pole figure at x = 45.5°, which corresponds to the (204) CIGS Bragg reflection and b) Ω/2Θ scan around the (204) Bragg reflection (oblique planes) on sample 1743/S597. ..... 100
Figure 4-16 STEM-HAADF image of the interface between the CIGS and the GaP layers (with FFT of each layer as insets), showing the epitaxy between both layers. ..... 100
Figure 4-17 An example of the integrated intensity calculation of the poles. ..... 101
Figure 4-18 The Pole Figures at CIGS (112) (left) and at GaP(111), for sample a, b) 1743/S554, c, d) 1743/S597, e, f) 1744/S554 and g, h) 1744/S597. ..... 104
Figure 4-19 Ω/2Θ scans from 26° to 30° with Φ = 90° and a) x = 16° or b) x = 55°. ..... 104
Figure 4-20 Sketches of the nominal CIGS planes and planes of the MTs related to a) G-B and b) G-C poles respectively. ..... 105
Figure 4-21 Stimulation result of the pole figure of the nominal CIGS planes and planes of the MTs. ..... 105
Figure 4-22 External quantum efficiency of CIGS solar cell on non-optimized GaP/Si pseudo-substrate compared to CIGS solar cell on glass (Mo) substrate. ..... 107
Figure 4-23 Dark I-V and I-V curves under illumination (AM1.5) on the solar cell. ..... 107
Figure 5-1 a) TEM images of CIGS/GaP/Si b) pole figure of CIGS/GaP/Si, which shows a clear CIGS (112) diffraction, as well as the MTs form in the CIGS layer. A transverse scan around the CIGS (112) position confirmed the diffraction is not an illusion from GaP (111). ..... 114

# List of abbreviations

| | |
|---|---|
| **AFM** | Atomic Force Microscopy |
| **APB** | Antiphase Boundary |
| **APD** | Antiphase Domain |
| **BF** | Bright Field |
| **CMOS** | Complementary Metal Oxide Semi-conductor |
| **CTR** | Crystal Truncation Rod |
| **DF** | Dark Field |
| **DFT** | Density Functional Theory |
| **EQE** | External Quantum Efficiency |
| **EIC** | Electronic Integrated Circuits |
| **FCC** | Face Centered Cubic |
| **HAADF** | High-Angle Annular Dark-Field |
| **HCP** | Hexagonal Close Packed Structure |
| **IB** | Integral Breadth |
| **K-map** | quicK continuous Mapping |
| **LED** | Light-Emitting Diode |
| **MBE** | Molecular Beam Epitaxy |
| **MEE** | Migration Enhanced Epitaxy |
| **MOCVD** | Metal Organic Chemical Vapor Deposition |
| **MOVPE** | Metal Organic Vapor Phase Epitaxy |

| | |
|---|---|
| **MT** | Microtwin |
| **OEIC** | Optoelectronic Integrated Circuits |
| **QF** | Quality Factor |
| **r.m.s.** | Root Mean Square |
| **RC** | Rocking Curve |
| **RHEED** | Reflection High-Energy Electron Diffraction |
| **RSM** | Reciprocal Space Map |
| **SEM** | Scanning Electron Microscopy |
| **SOI** | Silicon-on-Insulator |
| **STEM** | Scanning Transmission Electron Microscopy |
| **STM** | Scanning Tunneling Microscopy |
| **TDS** | Thermal Diffuse Scattering |
| **TEM** | Transmission Electron Microscopy |
| **UHVCVD** | Ultra-High Vacuum Chemical Vapor Deposition |
| **WHL** | Williamson-Hall like |
| **XRD** | X-ray Diffraction |

Remark: all the vectors are represented by a ***bold italic*** letter.

# Chapitre 1. Introduction

This chapter is dedicated to introducing the purpose of the study. A brief review on the heteroepitaxy of GaP on Si is given, which includes the applications of the study. The common crystal defects are firstly introduced, and then some principle defects, for instance dislocations, microtwins and antiphase boundaries, are discussed in the GaP/Si heteroepitaxial system. At last, the organization of the dissertation is given.

## 1.1. Towards a better world

Energy, information and material are three pillars of development of modern society. The semiconductor material is the key bonding between the three pillars. As to the bonding between energy and material, the Photovoltaic (PV) system based on semiconductor materials is one of the two technologies used in solar power plants (The other one is Concentrated Solar Power (CSP) system), when the solar power grows more and more important in the energy field, as the pollution of the traditional fossil power threatens the living environments of human beings. [1] As to the bonding between information and material, nearly all the chips, used in the electron computers, the smart phones, the domotics and other applications, are fabricated by silicon. In further, optoelectronic integrated circuits, which is considered as an alternative of the current electronic integrated circuits and a solution to overcome this bottleneck, are also based on semiconductor materials.

Silicon is the most mature semiconductor material. It is widely in the microelectronic industry and photovoltaic industry, owing to its natural abundance, low cost, high purity and availability of large single crystals. Silicon photonics, which use silicon, SiC, silicon on insulator (SOI) or SiGe, as the optical medium, has been applied in light emitters[2]–[4], waveguides[5]–[7], modulators[8]–[10], photodetectors[11]–[13]. In addition, the market share of silicon (including crystalline or amorphous) PV has never fell below 90% [14] in the last decade.

Nevertheless, silicon has its own limitation. The poor optical properties due to its indirect bandgap precludes both the efficient light emission and the efficient light absorption. Although many strategies have been applied to improve the optical properties of silicon, for instance, porous silicon [15]–[17], erbium doping [18]–[20], nanowires[21], [22], nanocrystals[23], [24], silicon is still less efficient compared to another important class of semiconductor materials, III-V compound semiconductors. Thus, the monolithic integration of III-V semiconductors on silicon is considered as a cornerstone for the integration of photonics into the mature silicon technology (semiconductor LED or laser [25]–[27] and integrated photonics devices [28]), as well as in the framework of the development of high-efficiency solar cells on low-cost silicon substrates (multijunction solar cells or solar cell heterojunctions), [29]–[31] and water splitting devices. [32]– [34]

Three main approaches have been developed and applied to realize the integration of III-V compound semiconductor on top of a silicon wafer: flip-chip, bonding, and heteroepitaxy.

In the flip-chip integration, III-V optoelectronic devices and the silicon platform are processed separately. Then one of the two components is flipped and interconnected to the other one through soldering. [35], [36] The bonding technique is to contact mirror-polished, flat and clean wafers to realize a strong bond between them based on the intermolecular interactions, for instance, van der Waals forces, hydrogen bonds and strong covalent bonds. In the bonding techniques, there are two different methods, i.e. direct bonding and adhesive bonding. In the wafer bonding process, the adhesive bonding has additional intermediate layers as “glues”, i.e. polymers or metals, while the direct bonding does not. The direct bonding of III-V semiconductor materials and silicon demands a high-temperature (>600 °C) anneal, while some devices fabricated on the silicon wafer, i.e. CMOS, become invalid at about 450 °C [37]. Thus, a key challenge to the direct bonding is that, how the anneal temperature can be sufficiently low to inhibit active material degradation [38]. $O_2$ plasma-assisted wafer bonding is proposed to solve the problem, and the process temperature has be decreased to below 400 °C [38], [39]. For the adhesive bonding, several materials, i.e. thermoplastic [40], elastomeric [41] and thermosetting materials [42], are used in the case of III-V semiconductor materials and silicon. Divinylsiloxane-bis-benzocyclobutene (DVS-BCB), as a thermosetting polymer, is selected from the materials by many groups due to its properties, such as, the low optical loss at telecommunication wavelengths, the high planarization and the high glass transition temperature[37], [43], [44].

Although some interesting results have been achieved with the two methods, heteroepitaxy is still considered as a promising and attractive technique. Because heteroepitaxy provides low-cost, highly integrated, and large-scale monolithic integration of III-V semiconductor materials and silicon. A brief literature review on the heteroepitaxy of III-V materials on silicon, especially GaP on Si, is given in the next section.

## 1.2. Heteroepitaxy of GaP and Si

Epitaxy refers to the growth of a crystalline overlayer on the crystalline surface of the substrate. The overlayer is also called epitaxy layer. The in-plane crystalline orientation of the epitaxy layer is usually defined by the substrate crystal structure. According to the compound

of the epitaxy layer and the substrate, epitaxy is classified into two types, i.e. homoepitaxy and heteroepitaxy. In the homoepitaxy, the epitaxy layer is the same material as the substrate, while it is purer or has different doping levels, compared to the substrate. The epitaxy layer in the heteroepitaxy has a different compound from the substrate, and III-V on silicon is a typical heteroepitaxy.

The heteroepitaxy of several common III-V semiconductor materials on silicon has been successfully performed, such as, GaAs[45]–[47], InGaAs[48], [49], InP[50], GaP[51], [52], GaSb[53], GaN[54], [55] and et.al. But the lattice mismatch between most III-V compounds and silicon is large. Figure 1-1 shows the band gap energy (wavelength) versus lattice constants for silicon and most common III-V semiconductors.

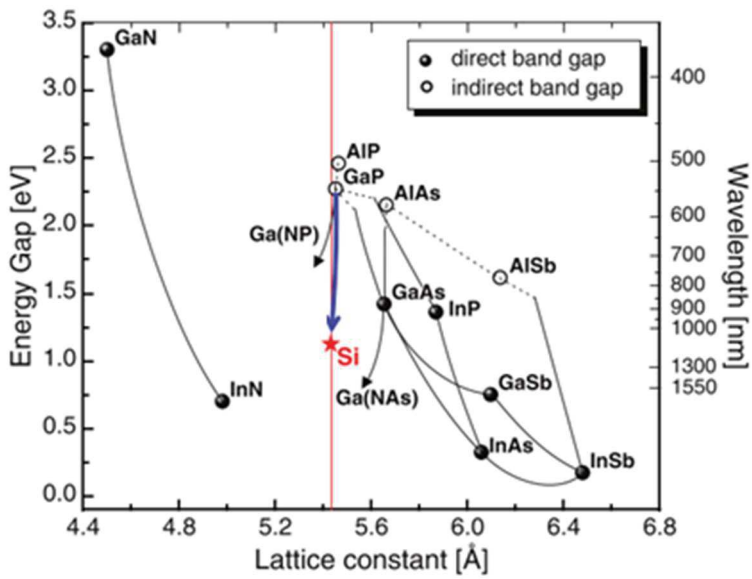


Figure 1-1 Band gap energy (wavelength) versus lattice constants for silicon and most common III-V semiconductors.

For thin III-V layer grown on silicon substrate, the lattice mismatch ***f*** is defined as the equation below:

$$f = \left|\frac{a_e - a_s}{a_s}\right| \qquad (1.1)$$

where $a_e$ is the lattice constant of the epitaxy layer, and $a_s$ is the lattice constant of the substrate. So, GaAs, InP and GaSb have 4.10%, 8.06% and 12.2% lattice mismatch compared to Si substrate, respectively. In addition, some results have shown that a large lattice mismatch

leads to a large dislocation density [56], [57], which can reduce the carrier lifetime [58]–[60] and influence the photoelectric properties of the final devices based on the heteroepitaxy structure.

While, Gallium phosphide (GaP), which is an indirect bandgap semiconductor material, has very small lattice mismatch with silicon. Some basic parameter of GaP and Si at the room temperature is shown as Table 1-1. The lattice mismatch of GaP and Si is only 0.37% at the room temperature. Thus, the epitaxial growth of quasi-lattice matched GaP on silicon has been developed to be used as an efficient platform for the subsequent integration of low-defect or defect-free III-V based heterostructures. For instance, the development of GaP/Si pseudo-substrates opens the route for the coherent growth of a direct band-gap material, using for example diluted-nitrides GaPN-based materials. Having nearly a lattice-match to Si, GaP/Si also provides a simple but important model system for the heteroepitaxial growth of polar semiconductor material on a nonpolar substrate.

| | GaP | Si |
|---|---|---|
| Lattice constant | 0.5451 | 0.5431 |
| $C_{11}$ | 140.5 GPa | 166.0 GPa |
| $C_{12}$ | 62.0 GPa | 64.0 GPa |
| Band gap energy | 2.26 eV | 1.12 eV |
| Thermal expansion coefficient | $4.65\times10^{-6}$/K | $2.6\times10^{-6}$/K |

Table 1-1 Some basic parameter of GaP and Si at the room temperature (300K).

Broadie et.al. from IBM in USA [61], T. Katoda and M.Kishi from University of Tokyo in Japan [62] had studied the heteroepitaxy of GaP on silicon substrated at 1980s. After that, T.J. Grassman et al. from the Ohio State University in USA [63], [64], K.Volz et.al. from Philipps-University in Marburg (Germany) [65], [66], Yonezu et.al. from Toyohashi University of Technology in Japan [67], [68], have also sucssefully achieved the heteroepitaxy of GaP on Si by either MBE or MOCVD. Recently, M. S. Sobolev and co-workers at St. Petersburg Academic University in Russia has achieved single crystalline GaP nucleation and buffer layers on silicon substrates with MBE. [69] They also invested the possibility of silicon or beryllium doping in GaP layers, which can used as

contact layers in the further development of devices. [70] C. Zhang et. al. from Arizona State University in USA worked on the application of GaP/Si in the heterojunction solar cells and have obtained n-GaP/n-Si heterojunction solar cells with an efficiency of 13.1% at AM1.5G. [71], [72] They also cooperated with M. Vaisman et.al from Yale University and National Renewable Energy Laboratory in USA to develop GaAsP solar cells on GaP/Si pseudo-substrate and achieved an efficiency of 15.3% at AM1.5G. [73]

In our laboratory, GaP-based optical devices [74], [75] and solar cells [76] has been reported for years. The heteroepitaxy of GaP on Si using UHVCVD-MBE is also studied in recent years [77]–[79]. The aim of the thesis work is to characterize the structure defects on the base of former study and develop more analytical methods for the improvement of the GaP/Si platform.

## 1.3. Crystallographic defect

In an unlimited perfect crystal, the arrangement of the atoms or molecules usually has long-range periodicity. The minimum group of atoms or molecules, which constitutes the repeating pattern is called the unit cell. If each unit cell is treated as a point, then the crystal cells can repeat themselves after a set of symmetry operations, which is called the crystallographic point group. Thus, the interruptions of the periodic crystal structure are called the crystallographic defects, or defects. According to the geometric dimension of the defects, they can be classified into point defects, line defects, planar defects and bulk defects, which are corresponding to 0D, 1D, 2D, and 3D, respectively. In the section, I will give a brief introduction to the definition and the classification of these defects. For some principle defects in the heteroepitaxy of GaP and Si, for instance dislocations, microtwins and antiphase boundaries, the detailed discussion will be in the next section.

### 1.3.1. Point defects

Point defect occurs only at or around a single lattice point. A point can only be missing or additionally placed in the lattice structure, so the point defects have three typical types, which is shown in Figure 1-2.

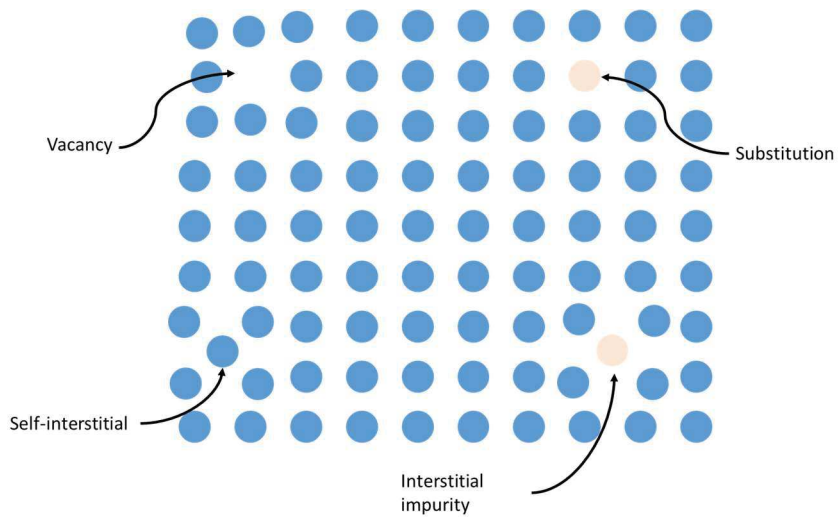


Figure 1-2 A schematic representation of typical point defects in the lattice structure.

a) Vacancy defect is the situation that the lattice site should have an atom but is vacant. Around a vacancy defect, the surrounding lattice points can collapse to the vacant site, while they can also be "dragged" away due to the missing of attraction of vacancy defect in some material.

b) Interstitial defect is that an additional atom is placed at an irregular site in the lattice structure. Considering that different atoms can existed in the lattice structure, if the additional atom is the same atom as the crystal, it is called self-interstitial. Otherwise, it is called interstitial impurity. Sometimes, the vacancy defect and interstitial defect can occur around the same lattice point, which is often called a Frenkel defect or a Frenkel pair. The self-interstitial can occur in several materials including Si due to the high stress or the high energy state.

c) Substitutional defect is that a different point replaced the raw point in the lattice site. If the point is an ion, then the substitutional defect can be classified into isovalent substitution and aliovalent substitution according to if the new ion has the same oxidation state as the original ion.

The vacancy defect, interstitial impurity and substitutional defect are common in the semiconductor production. Because the doping, as an important process in the semiconductor production, is to insert impurities into an intrinsic semiconductor and the doped atoms can be seen as the artificial interstitial impurity or substitutional defect. The purpose of doping is to module the electronical, optical or structural properties of the raw semiconductor.

### 1.3.2. Line defects

A line defect refers to a whole row of anomalously arranged points in the lattice structure. The mis-arrangement of the lattice points is usually called the line of dislocation. Thus, the dislocations and the line defects are considered to be equivalent in many places.

### 1.3.3. Planar defects

In single crystals, the points in the lattice structure form layers, which are stacked with a certain order. The most discussed example of the planar defects in single crystals is found in close-packed crystal structures, because the hexagonal close packed structure (HCP) and face centered cubic structure (FCC) differ with each other only in stacking order. Two models of HCP and FCC are shown in Figure 1-3 (a) and (b), respectively. The stacking sequence of HCP is ABABAB, while that of FCC is ABCABC. Similar to the point defects, the planar defects occur when the layers are missing or additionally placed. If the layer is missed (ABC_BCABC), the defect is called intrinsic stacking fault. If a layer is additionally placed (ABC***B***ABC), the defect is called extrinsic stacking fault.

In the materials of FCC structures, for instance Si or GaP, if the intrinsic stacking fault occurs, the defect phase is actually of HCP structure. In addition, the band gap energy of the same material with FCC and HCP structures are usually different. So, the stacking faults have a large impact on the local optical properties.

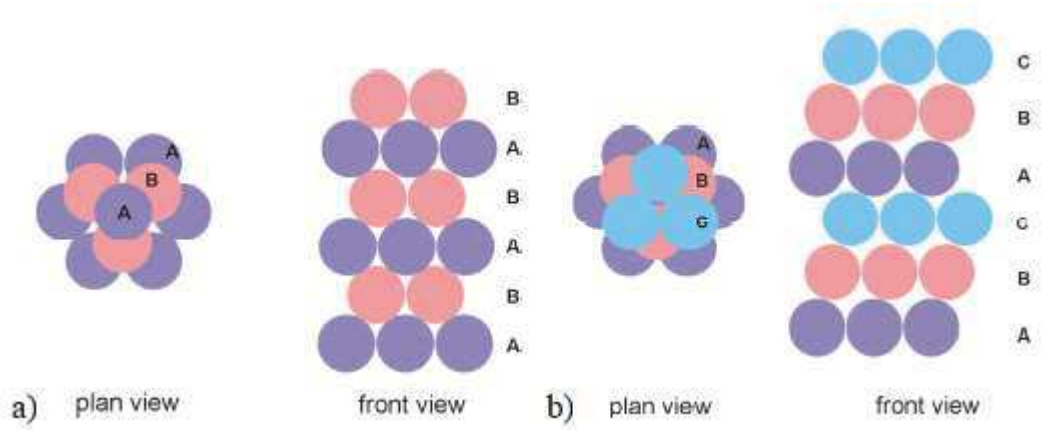


Figure 1-3 Stacking sequence of hexagonal close packed structure (HCP) and face centered cubic structure (FCC).

A special case in the stacking fault is the twins, where the stacking sequences are mirror symmetric besides the defects, i.e. ABCABC|CBCABC.

In polycrystals, another type of planar defect is the grain boundary, which is the interface between two grains or crystallites. The grain is usually defined as the smallest unit with the same orientation in polycrystals, such as copper indium gallium selenide (CIGS), which is shown in Figure 1-4. [80]

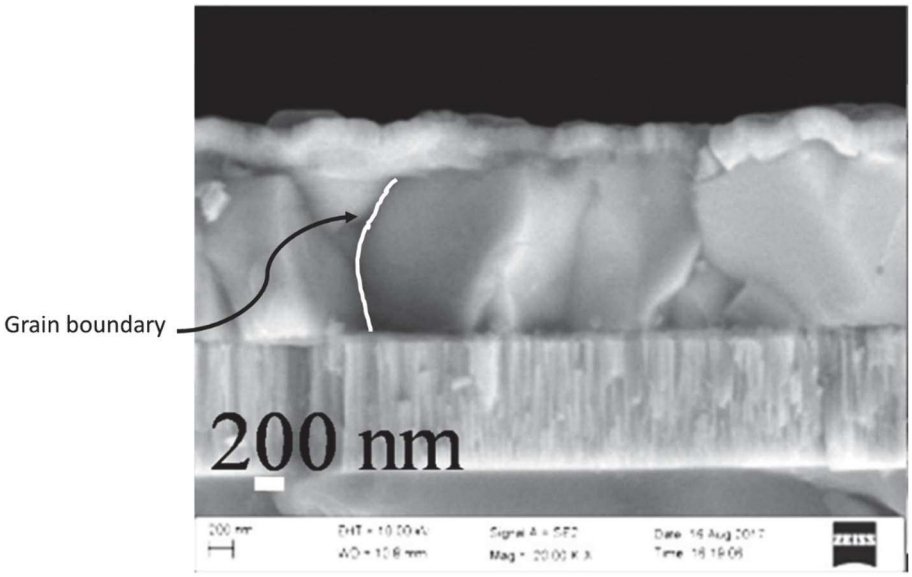


Figure 1-4 A TEM image which show the grain boundaries in CIGS grown on Mo/glass. [80]

### 1.3.4. Volume defects

The volume defects are voids or local region featuring different phase in crystalline materials. The defect phase between two opposite planar defects are volume defects. An antiphase domain is a volume defect between two antiphase boundaries.

## 1.4. Principle crystallographic defects in GaP/Si pseudo-substrate

In the GaP/Si pseudo-substrate, the principle defects include dislocations, microtwins, antiphase boundaries and mosaicity characteristics. Although the lattice constant of GaP is very close to Si at room temperature, the 0.37% misfit between GaP and Si has to be taken into account in the heteroepitaxy. There are two situations during the heteroepitaxy. The first one is to squeeze the epitaxial layer to fit on the substrate. The second one is to relief the strain and stress by introducing some defects.

The first situation often occurs in the growth of thin layers. The strain and stress energy will be stored in the epitaxial layer. The growth mode of this situation is usually called “coherent growth” or “pseudomophic growth”. For the growth of thicker epitaxy layer, the initial layer is also similar to the thin layer.

The lattice strain of the GaP epitaxy layer on nominal Si substrate and vicinal Si substrate is shown in Figure 1-5.

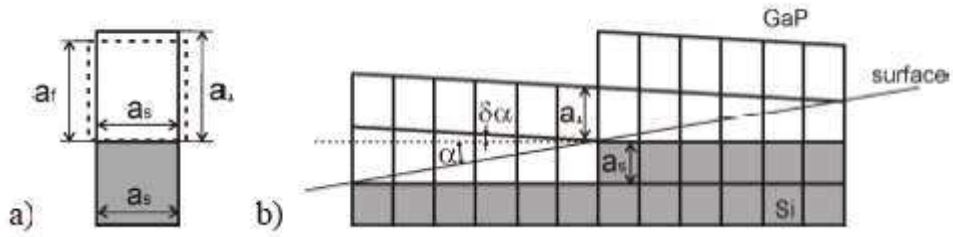


Figure 1-5 The sketch of the lattice strain of GaP thin layer on a) nominal and b)vicinal Si substrate. [81]

The out-of-plane relaxation $\varepsilon_{\perp}$ and in-plain relaxation $\varepsilon_{\parallel}$ can be defined as below:

$$\varepsilon_{\perp} = \frac{a_{\perp} - a_f}{a_f} \tag{1.2}$$

$$\varepsilon_{\parallel} = \frac{a_{\parallel} - a_f}{a_f} \tag{1.3}$$

where $\mathbf{a}_{\perp}$ is the out-of-plane lattice constant of the epitaxy layer, $\mathbf{a}_{\parallel}$ is the out-of-plane lattice constant of the epitaxy layer, and $\mathbf{a_f}$ is the lattice constant of bulk GaP.

According to the Hooke’s law, the out-of-plane relaxation $\boldsymbol{\varepsilon}_{\perp}$ and in-plain relaxation $\boldsymbol{\varepsilon}_{\parallel}$ have a relationship as below:

$$\varepsilon_{\perp} = -\frac{2C_{12}}{C_{11}}\varepsilon_{\parallel} \tag{1.4}$$

For the nominal substrate, $\boldsymbol{a}_{\parallel}$ is equal to the lattice constant of Si $\boldsymbol{a_s}$. For the vicinal substrate, the $\boldsymbol{a}_{\parallel}$ is: [81]

$$a_{\parallel} = a_s + \frac{tan(\Delta\alpha)}{tan(\alpha)} a_s \tag{1.5}$$

where $\boldsymbol{\Delta\alpha}$ is the tilt angle between the [001] orientation of GaP and that of Si, $\boldsymbol{\alpha}$ is the vicinal angle of the substrate. For $\boldsymbol{\alpha} = 6°$, $\boldsymbol{\Delta\alpha}$ is only 0.041°. Thus, the difference between the $\boldsymbol{a}_{\parallel}$ and $\boldsymbol{a_s}$ is so little that it can be neglected.

The elastic energy $\boldsymbol{E}$ generated in this way is nearly proportional to the thickness of the epitaxial layer $\boldsymbol{h}$, which is:

$$\mathrm{E} = \varepsilon_{\parallel}^{2}\mathrm{M_f h} \tag{1.6}$$

where $\boldsymbol{M_f}$ is the biaxial modulus of the film. [82]

As the ability of the epitaxial layer to store the elastic energy is limited, the maximum thickness to keep the energy is called the critical thickness. If the sample thickness is beyond the critical thickness, the sample is considered to be relaxed. The critical thickness can be calculated with the Matthews-Blakeslee critical thickness model [83]–[85], and modified by considering other defects, such as vicinal substrate. The critical thickness for GaP/Si pair in heteroepitaxy has been determined to be around 50 nm by Yamane et.al.[86], 45 nm by Skibitzki [87] and below 90 nm by Soga et.al.[88].

While, many of our sample has a thickness of the epitaxial layer which is beyond the critical thickness. In the condition, the strain and stress energy will be released by relieved both by formation and/or propagation the defects, which is mainly the dislocation. [89] In addition, due to the physical and chemical presence of an interface between GaP and Si, some specific defects, i.e. microtwins, antiphase boundaries and mosaicity characteristics, occur in the heteroepitaxy.

### 1.4.1. Dislocation

Dislocation was proposed to be a defect in atomic scale by G. I. Taylor in 1934. [90] So, it is also called Taylor's dislocation. In geometry, dislocations can be described by a vector $\boldsymbol{b}$, which is called Burgers vector. The Burgers vector is determined by the closure failure of a closed loop, which trace around the end of the dislocation plane. According to the direction of the Burgers vector, dislocations can be classified into two primary type: edge dislocations and screw dislocations, which is shown in Figure *1-6* a) and b), respectively [91]. The line vector $\boldsymbol{t}$ describes the local direction of the dislocation line. If the Burgers vector $\boldsymbol{b}$ is orthogonal to the line vector $\boldsymbol{t}$, then the dislocation is edge dislocation. While, if the Burgers vector $\boldsymbol{b}$ is parallel

to the line vector ***t***, then the dislocation is screw dislocation. The real dislocations are always mixture of the two. The energy $\boldsymbol{E}_{\mathbf{dis}}$ of a dislocation is about $5\mathrm{eV}/|b|$.

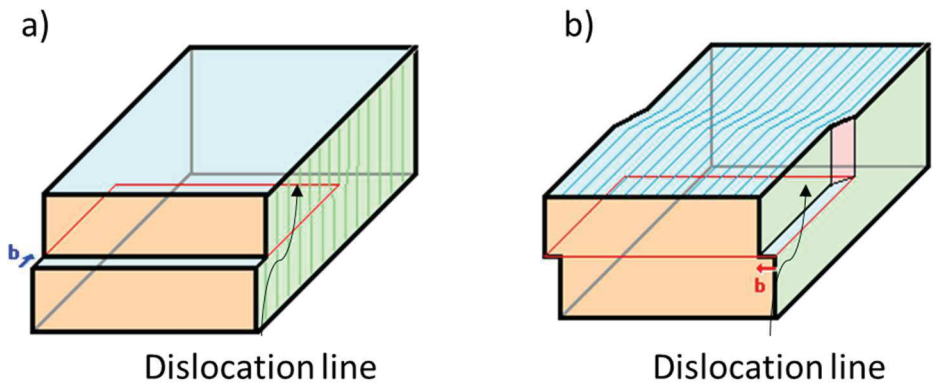


Figure 1-6 The sketch of the a) edge dislocation and b) screw dislocation. [91]

In our GaP/Si pseudo-substrate, the most important dislocation is a specific dislocation called 60° dislocations or misfit dislocations, which are the principle relaxation process in the GaP/Si structure. [88] 60° dislocations have **a**/2<101> Burgers vectors and {111} glide planes, which is shown in Figure 1-7 [92]. The main factor used to characterize the dislocations is the dislocation density. The density describes how many dislocations are in the unit distance, which is orthogonal to the line vector ***t*** of dislocations.

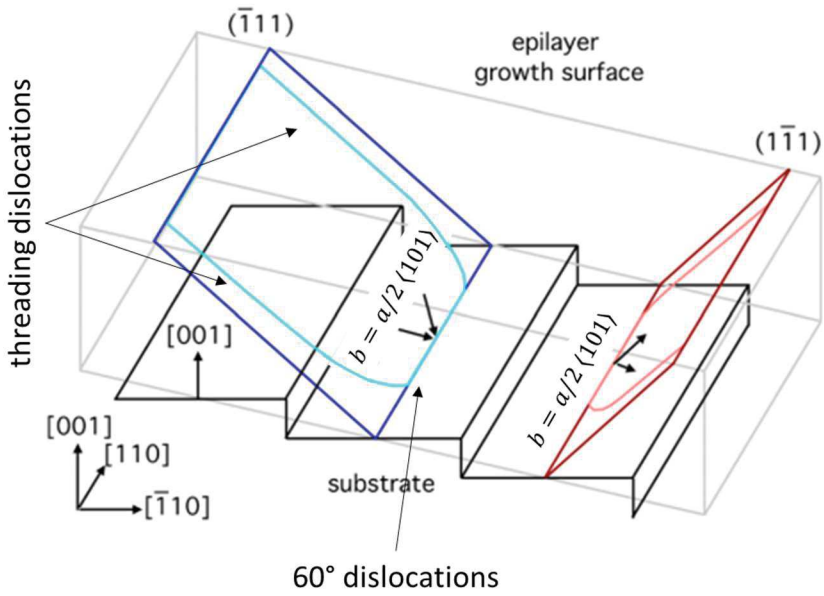


Figure 1-7 A sketch of 60° dislocations in heteroepitaxy layer on vicinal substrate. [92]

For other III-V materials grown on silicon substrates with a larger lattice mismatch, a 60° dislocation can be split by a stacking fault into a 30° dislocation and a 90° dislocation, which has lower energy than a single 60° dislocation. Higher stress can also directly lead to more 90° dislocations instead of 60° dislocations.

### 1.4.2. Microtwins

The microtwins is a phase domain consist of a sequence of twins. In the zinc blende system like GaP/Si, the twinning domain is the same as the {111} planes of the nominal phase with a rotation around corresponding [111] axis. The nominal {111} planes are 54.7° away from the (001) plane of the nominal phase, while the MTs planes are 15.9° away. Due to the fourfold symmetry of the zinc blende system, there are four different MTs. See from the above of the sample, the four MTs are labelled with A, B, C and D in counterclockwise order, which is shown in upper part of Figure 1-8. The sketch is based on the clear drawing of O. Skibitzki [87]. The two MTs parallel to the atomic steps are MT-A and MT-C, and the other two are MT-B and MT-D. In the reciprocal space (the bottom part of Figure 1-8), the green ellipsoids are the mirror symmetry of the nominal lattice point( (-1 -1 -1) and (-2 -2 0) ) around the [11-1] axis, indicating the additional reflections due to the MT-A. The elongation of the spot along the [11-1] direction is the result of that, the MT domain is a thin “platelet”. In addition, the MT-A is nearly parallel to nominal {115} planes.

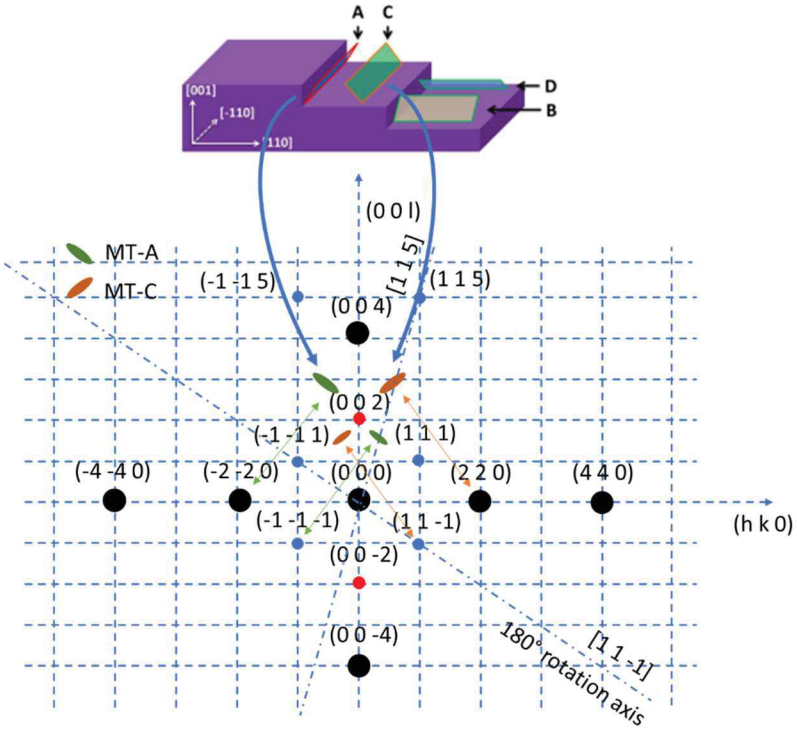


Figure 1-8 A sketch of four microtwins in GaP thin layer on vicinal Si substrate [87], and GaP in the reciprocal space. Strong, medium and weak reflections are labelled with black, blue and red points. MT-A and MT-C are labelled with green and orange ellipsoids.

### 1.4.3. Antiphase Domain

The antiphase boundary (APB) is a specific planar defect, which separates two domains of the same ordered phase. The antiphase domains (APDs) are volume defects formed between APBs. For the APDs in GaP epitaxy layers, the Ga atoms locate at the lattice sites what occupied by P atoms in the normal structure, and vice versa. A schematic representation of the APD in GaP epitaxy layers on silicon substrates with mono-atomic steps is shown in Figure 1-9.

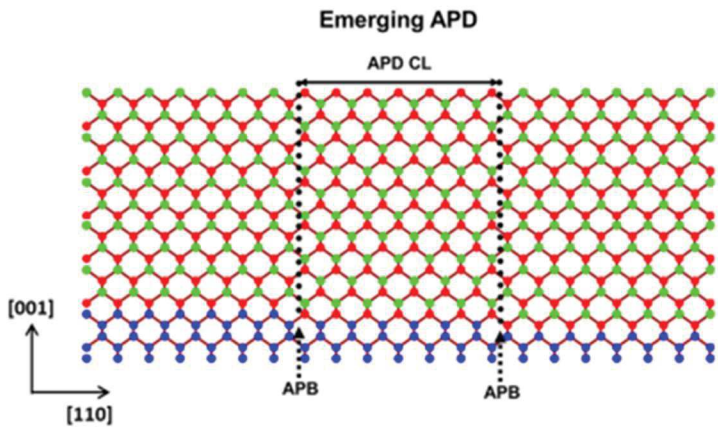


Figure 1-9 The APD in GaP epitaxy layers on silicon substrates with mono-atomic steps.

There have been several reports on the APDs in GaP epitaxy layers on silicon substrates. H. Döscher et.al. from Helmholtz Center in Germany have applied Reflectance Anisotropy Spectroscopy (RAS) as an *in-situ* probe to measure and quantify the Anti-Phase Domain (APD) content in the GaP heteroepitaxial layer grown on the Si substrate. [93], [94] The originating mechanism of the APDs, one of the main defects originating at the nucleation process of the GaP on the Si (001) substrate, was discussed by K. Volz et.al. from Phillips University. [95], [96] E. L. Warren et.al. from National Renewable Energy Laboratory in USA achieved APD free growth of GaP on Si with *in-situ* AsH3-etching during the epitaxy by MOCVD, which is demonstrated by both Low-energy electron diffraction (LEED) and Transmission electron microscope (TEM). [52] Our laboratory has also used X-ray diffraction and transmission electron microscopy (TEM) to quantitively measure the lateral size of the APDs in GaP on vicinal Si substrates grown by MBE. [79], [97] It had been suggested that the APDs could be better self-annihilated on vicinal Si substrates with bi-atomic steps. [98]–[100] A most recent study in our laboratory by I. Lucci et.al. pointed that the phases of the initial GaP islands on the Si substrates have large impact on the formation and self-annihilation of APDs. [101]

### 1.4.4. Mosaic

The GaP heteroepitaxy layer on Si consist of small crystalline block with a typical size equal to a few micrometers, which is shown in Figure 1-10. As the size of these small crystalline blocks is so small, they are usually called mosaics instead of grains. The sizes of mosaics, which is called coherence lengths, are mainly determined by the planar defects. The mosaics can have tilt around the nominal surface, which is usually several secs. As the size and the tilt of the

mosaics are both very small in GaP thin layers, the GaP thin layers are considered to be monocrystalline in many situations. But if the spatial resolution of the characterization methods (i.e. sub-microbeam X-ray scanning diffraction or TEM) are high enough, the mosaicity characteristics should be taken into account.

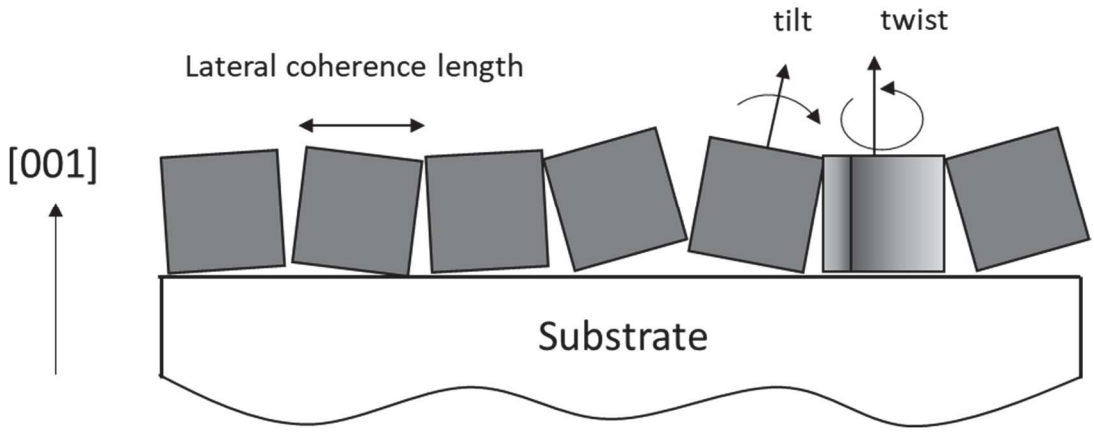


Figure 1-10 A sketch of Mosaics with limited lateral coherence length, tilt or twist in GaP heteroepitaxy layer on Si substrate.

## 1.5. The organization of the thesis

Chapter 1 describes the purpose of the thesis work. The GaP/Si pseudo substrate provides an important platform in the monolithic integration of III-V semiconductor materials and Si, which have a large application field in both photonics and photovoltaics. A general introduction on the crystal defects are presented, and some important defects in heteroepitaxial thin layers, for instance dislocations, MTs and APDs, are detailed.

Chapter 2 introduces the techniques in the growth and characterization process, which are applied in the thesis work. The Si substrate preparation and the heteroepitaxy of GaP/Si thin layers by using MBE are firstly introduced. Then the most important characterization method, X-ray diffractions, is detailed, including basic principles, experimental setup and data process methods. Finally, other characterization methods, for instance atomic force microscope and transmission electron microscope, are introduced.

Chapter 3 is dedicated to the characterization of the dislocations' distribution, by using an advanced X-ray technique, sub-micrometer scanning X-ray diffraction. Firstly, a brief review on the former characterization results on similar samples are given. Then, the sample

preparation and the structural result performed with lab-setup measurements are present. Finally, with the analysis of the sub-micrometer scanning X-ray diffraction results, the distribution of dislocations is found to be inhomogeneous. The distribution of dislocations has strong impact the sample surface roughness.

Chapter 4 presents the primary evaluation of CIGS/GaP/Si tandem solar cells, which can be both low-cost and high-efficiency. The CIGS is observed to epitaxially grown on GaP/Si pseudo substrates, by analyzing the results from ω/2θ scan, reciprocal space map and pole figures. The influence of the growth condition on the structural quality is also discussed.

Finally, Chapter 5 summarizes all the results obtained during the thesis, including the structural analyses of the GaP/Si layer and CIGS/GaP/Si solar cells.

## References


[1] C. A. Horowitz, "Paris Agreement," *Int Leg Mater*, vol. 55, no. 4, pp. 740–755, 2016.

[2] K. Eberl, O. G. Schmidt, R. Duschl, O. Kienzle, E. Ernst, and Y. Rau, "Self-assembling SiGe and SiGeC nanostructures for light emitters and tunneling diodes," *Thin Solid Films*, vol. 369, no. 1–2, pp. 33–38, 2000.

[3] D. P. Yu *et al.*, "Amorphous silica nanowires: Intensive blue light emitters," *Appl. Phys. Lett.*, vol. 73, no. 21, pp. 3076–3078, 1998.

[4] D. J. Lockwood, Z. H. Lu, and J.-M. Baribeau, "Quantum confined luminescence in Si/SiO 2 superlattices," *Phys. Rev. Lett.*, vol. 76, no. 3, p. 539, 1996.

[5] U. Fischer, T. Zinke, J.-R. Kropp, F. Arndt, and K. Petermann, "0.1 dB/cm waveguide losses in single-mode SOI rib waveguides," *IEEE Photonics Technol. Lett.*, vol. 8, no. 5, pp. 647–648, 1996.

[6] G. Li *et al.*, "Ultralow-loss, high-density SOI optical waveguide routing for macrochip interconnects," *Opt. Express*, vol. 20, no. 11, pp. 12035–12039, 2012.

[7] X. Wang, W. Shi, H. Yun, S. Grist, N. A. Jaeger, and L. Chrostowski, "Narrow-band waveguide Bragg gratings on SOI wafers with CMOS-compatible fabrication process," *Opt. Express*, vol. 20, no. 14, pp. 15547–15558, 2012.

[8] C. E. Png, S. P. Chan, S. T. Lim, and G. T. Reed, "Optical phase modulators for MHz and GHz modulation in silicon-on-insulator (SOI)," *J. Light. Technol.*, vol. 22, no. 6, p. 1573, 2004.

[9] J. Liu, D. Pan, S. Jongthammanurak, K. Wada, L. C. Kimerling, and J. Michel, “Design of monolithically integrated GeSi electro-absorption modulators and photodetectors on an SOI platform,” *Opt. Express*, vol. 15, no. 2, pp. 623–628, 2007.

[10] T.-Y. Liow *et al.*, “Silicon modulators and germanium photodetectors on SOI: monolithic integration, compatibility, and performance optimization,” *IEEE J. Sel. Top. Quantum Electron.*, vol. 16, no. 1, pp. 307–315, 2009.

[11] H. Yamamoto, K. Taniguchi, and C. Hamaguchi, “High-sensitivity SOI MOS photodetector with self-amplification,” *Jpn. J. Appl. Phys.*, vol. 35, no. 2S, p. 1382, 1996.

[12] G. Dehlinger, S. J. Koester, J. D. Schaub, J. O. Chu, Q. C. Ouyang, and A. Grill, “High-speed germanium-on-SOI lateral PIN photodiodes,” *IEEE Photonics Technol. Lett.*, vol. 16, no. 11, pp. 2547–2549, 2004.

[13] X. Wang, Z. Cheng, K. Xu, H. K. Tsang, and J.-B. Xu, “High-responsivity graphene/silicon-heterostructure waveguide photodetectors,” *Nat. Photonics*, vol. 7, no. 11, p. 888, 2013.

[14] S. Ali, Ed., *Comprehensive Renewable Energy*, vol. Photovoltaic Solar Energy, 1 vols. Boston: Elevier Science, 2012.

[15] V. Lehmann and U. Gösele, “Porous silicon formation: A quantum wire effect,” *Appl. Phys. Lett.*, vol. 58, no. 8, pp. 856–858, 1991.

[16] V. S.-Y. Lin, K. Motesharei, K.-P. S. Dancil, M. J. Sailor, and M. R. Ghadiri, “A porous silicon-based optical interferometric biosensor,” *Science*, vol. 278, no. 5339, pp. 840–843, 1997.

[17] G. Korotcenkov, “Porous Silicon Characterization and Application: General View,” in *Porous Silicon: From Formation to Application: Formation and Properties, Volume One*, CRC Press, 2016, pp. 20–43.

[18] H. Ennen, G. Pomrenke, A. Axmann, K. Eisele, W. Haydl, and J. Schneider, “1.54-µm electroluminescence of erbium-doped silicon grown by molecular beam epitaxy,” *Appl. Phys. Lett.*, vol. 46, no. 4, pp. 381–383, 1985.

[19] J. Palm, F. Gan, B. Zheng, J. Michel, and L. C. Kimerling, “Electroluminescence of erbium-doped silicon,” *Phys. Rev. B*, vol. 54, no. 24, p. 17603, 1996.

[20] G. Mula *et al.*, “Doping porous silicon with erbium: pores filling as a method to limit the Er-clustering effects and increasing its light emission,” *Sci. Rep.*, vol. 7, no. 1, p. 5957, 2017.

[21] P. R. Wiecha, A. Arbouet, H. Kallel, P. Periwal, T. Baron, and V. Paillard, “Enhanced nonlinear optical response from individual silicon nanowires,” *Phys. Rev. B*, vol. 91, no. 12, p. 121416, 2015.

[22] M. Keplinger *et al.*, “Strain distribution in single, suspended germanium nanowires studied using nanofocused x-rays,” *Nanotechnology*, vol. 27, no. 5, p. 055705, Feb. 2016.

[23] M. Dasog, J. Kehrle, B. Rieger, and J. G. Veinot, “Silicon nanocrystals and silicon-polymer hybrids: synthesis, surface engineering, and applications,” *Angew. Chem. Int. Ed.*, vol. 55, no. 7, p. 2322–2339, 2016.

[24] N. J. Kramer, K. S. Schramke, and U. R. Kortshagen, “Plasmonic properties of silicon nanocrystals doped with boron and phosphorus,” *Nano Lett.*, vol. 15, no. 8, p. 5597–5603, 2015.

[25] S. Liebich *et al.*, “Laser operation of Ga(NAsP) lattice-matched to (001) silicon substrate,” *Appl Phys Lett*, vol. 99, no. 7, p. 071109, 2011.

[26] K. Yamane *et al.*, “Growth of a lattice-matched GaAsPN p–i–n junction on a Si substrate for monolithic III–V/Si tandem solar cells,” *Appl Phys Express*, vol. 10, no. 7, p. 075504, 2017.

[27] A. Y. Liu *et al.*, “Electrically pumped continuous-wave 13 µm quantum-dot lasers epitaxially grown on on-axis (001) GaP/Si,” *Opt Lett*, vol. 42, no. 2, p. 338, 2017.

[28] P. Guillemé *et al.*, “Second harmonic generation in gallium phosphide microdisks on silicon: from strict to random quasi-phase matching,” *Semicond Sci Tech*, vol. 32, no. 6, p. 065004, 2017.

[29] M. Feifel *et al.*, “MOVPE Grown Gallium Phosphide-Silicon Heterojunction Solar Cells,” *Ieee J Photovolt*, vol. 7, no. 2, pp. 502–507, 2017.

[30] C. Cornet, M. Silva, C. Levallois, and O. Durand, *GaP/Si-Based Photovoltaic Devices Grown by Molecular Beam Epitaxy*, *Second Edition.*, Elsevier, 2018, pp. 637–648.

[31] R. Varache, M. Darnon, M. Descazeaux, M. Martin, T. Baron, and D. Muñoz, “Evolution of Bulk c-Si Properties during the Processing of GaP/c-Si Heterojunction Cell,” *Enrgy Proced*, vol. 77, pp. 493–499, 2015.

[32] O. Supplie, M. M. May, H. Stange, C. Höhn, H.-J. Lewerenz, and T. Hannappel, “Materials for light-induced water splitting: In situ controlled surface preparation of GaPN epilayers grown lattice-matched on Si(100),” *J Appl Phys*, vol. 115, no. 11, p. 113509, 2014.

[33] J. L. Young, M. A. Steiner, H. Döscher, R. M. France, J. A. Turner, and T. G. Deutsch, “Direct solar-to-hydrogen conversion via inverted metamorphic multi-junction semiconductor architectures,” *Nat Energy*, vol. 2, no. 4, p. 17028, 2017.

[34] I. Lucci *et al.*, “A Stress-Free and Textured GaP Template on Silicon for Solar Water Splitting,” *Adv Funct Mater*, vol. 28, no. 30, p. 1801585, 2018.

[35] J. H. Lau, *Flip chip technologies*, vol. 1. New York: McGraw-Hill, 1996.

[36] M. D. Rostoker, *Multi-chip semiconductor arrangements using flip chip dies*. U.S. Patents, 1995.

[37] G. Roelkens *et al.*, “III-V/silicon photonics for on-chip and intra-chip optical interconnects,” *Laser Photonics Rev.*, vol. 4, no. 6, pp. 751–779, Nov. 2010.

[38] K. Tanabe, K. Watanabe, and Y. Arakawa, “III-V/Si hybrid photonic devices by direct fusion bonding,” *Sci. Rep.*, vol. 2, p. 349, 2012.

[39] D. Pasquariello and K. Hjort, “Plasma-assisted InP-to-Si low temperature wafer bonding,” *IEEE J. Sel. Top. Quantum Electron.*, vol. 8, no. 1, pp. 118–131, Feb. 2002.

[40] F. J. Blanco *et al.*, “Novel three-dimensional embedded SU-8 microchannels fabricated using a low temperature full wafer adhesive bonding,” *J. Micromechanics Microengineering*, vol. 14, no. 7, p. 1047, 2004.

[41] Y. Sun, D.-Y. Khang, F. Hua, K. Hurley, R. G. Nuzzo, and J. A. Rogers, “Photolithographic route to the fabrication of micro/nanowires of III–V semiconductors,” *Adv. Funct. Mater.*, vol. 15, no. 1, pp. 30–40, 2005.

[42] S. Keyvaninia, M. Muneeb, S. Stanković, P. J. Van Veldhoven, D. Van Thourhout, and G. Roelkens, “Ultra-thin DVS-BCB adhesive bonding of III-V wafers, dies and multiple dies to a patterned silicon-on-insulator substrate,” *Opt. Mater. Express*, vol. 3, no. 1, pp. 35–46, 2013.

[43] S. Stankovic, R. Jones, M. N. Sysak, J. M. Heck, G. Roelkens, and D. Van Thourhout, “Hybrid III–V/Si distributed-feedback laser based on adhesive bonding,” *IEEE Photonics Technol. Lett.*, vol. 24, no. 23, pp. 2155–2158, 2012.

[44] S. Keyvaninia *et al.*, “Heterogeneously integrated III-V/silicon distributed feedback lasers,” *Opt. Lett.*, vol. 38, no. 24, pp. 5434–5437, 2013.

[45] D. K. Biegelsen, F. A. Ponce, A. J. Smith, and J. C. Tramontana, “Initial stages of epitaxial growth of GaAs on (100) silicon,” *J. Appl. Phys.*, vol. 61, no. 5, pp. 1856–1859, 1987.

[46] L. Wang *et al.*, “Toward All MOCVD Grown InAs/GaAs Quantum Dot Laser on CMOS-compatible (001) Silicon,” in *CLEO: Science and Innovations*, 2019, p. JTu2A. 82.

[47] J. Wang *et al.*, “1.3 µm InAs/GaAs quantum dot lasers on silicon with GaInP upper cladding layers,” *Photonics Res.*, vol. 6, no. 4, pp. 321–325, 2018.

[48] S. Chowdhury, A. Das, and P. Banerji, “Growth of indium gallium arsenide thin film on silicon substrate by MOCVD technique,” in *AIP Conference Proceedings*, 2018, vol. 1953, p. 030233.

[49] W. K. Loke, K. H. Lee, Y. Wang, C. S. Tan, E. A. Fitzgerald, and S. F. Yoon, “MOCVD growth of InGaP/GaAs heterojunction bipolar transistors on 200 mm Si wafers for heterogeneous integration with Si CMOS,” *Semicond. Sci. Technol.*, vol. 33, no. 11, p. 115011, 2018.

[50] S. Lourdudoss, “Heteroepitaxy of InP on Si for photonic and photovoltaic applications,” in *2016 Compound Semiconductor Week (CSW)[Includes 28th International Conference on Indium Phosphide & Related Materials (IPRM) & 43rd International Symposium on Compound Semiconductors (ISCS)]*, 2016, pp. 1–1.

[51] C. Zhang, Y. Kim, N. N. Faleev, and C. B. Honsberg, “Improvement of GaP crystal quality and silicon bulk lifetime in GaP/Si heteroepitaxy,” *J. Cryst. Growth*, vol. 475, pp. 83–87, 2017.

[52] E. L. Warren, A. E. Kibbler, R. M. France, A. G. Norman, J. M. Olson, and W. E. McMahon, “Investigation of GaP/Si heteroepitaxy on MOCVD prepared Si (100) surfaces,” in *2015 IEEE 42nd Photovoltaic Specialist Conference (PVSC)*, 2015, pp. 1–4.

[53] B. Lai, “Heteroepitaxy and characterization of GaSb and InAs narrow bandgap semiconductors on Si,” Master., Hong Kong University of Science and Technology, Hong Kong, 2018.

[54] A. Tanaka, W. Choi, R. Chen, and S. A. Dayeh, “Si complies with GaN to overcome thermal mismatches for the heteroepitaxy of thick GaN on Si,” *Adv. Mater.*, vol. 29, no. 38, p. 1702557, 2017.

[55] A. Bansal, N. C. Martin, K. Wang, and J. M. Redwing, “GaN Heteroepitaxy on Strain-Engineered (111) Si/Si 1− x Ge x,” *J. Electron. Mater.*, vol. 48, no. 5, pp. 3355–3362, 2019.

[56] R. People and J. C. Bean, “Calculation of critical layer thickness versus lattice mismatch for Ge x Si1− x/Si strained-layer heterostructures,” *Appl. Phys. Lett.*, vol. 47, no. 3, pp. 322–324, 1985.

[57] G. B. Stringfellow, “The importance of lattice mismatch in the growth of Ga x In1− x P epitaxial crystals,” *J. Appl. Phys.*, vol. 43, no. 8, pp. 3455–3460, 1972.

[58] C. L. Andre *et al.*, “Impact of dislocations on minority carrier electron and hole lifetimes in GaAs grown on metamorphic SiGe substrates,” *Appl. Phys. Lett.*, vol. 84, no. 18, pp. 3447–3449, May 2004.

[59] D. Jung *et al.*, “Impact of threading dislocation density on the lifetime of InAs quantum dot lasers on Si,” *Appl. Phys. Lett.*, vol. 112, no. 15, p. 153507, Apr. 2018.

[60] C. Heidelberger and E. A. Fitzgerald, “GaAsP/InGaP HBTs grown epitaxially on Si substrates: Effect of dislocation density on DC current gain,” *J. Appl. Phys.*, vol. 123, no. 16, p. 161532, Apr. 2018.

[61] H. B. Pogge, B. M. Kemlage, and R. W. Broadie, “The heteroepitaxial growth of GaP films on Si substrates,” *J. Cryst. Growth*, vol. 37, no. 1, pp. 13–22, Jan. 1977.

[62] T. Katoda and M. Kishi, “Heteroepitaxial growth of gallium phosphide on silicon,” *J. Electron. Mater.*, vol. 9, no. 4, pp. 783–796, Jul. 1980.

[63] T. J. Grassman *et al.*, “Control and elimination of nucleation-related defects in GaP/Si (001) heteroepitaxy,” *Appl. Phys. Lett.*, vol. 94, no. 23, p. 232106, 2009.

[64] T. J. Grassman *et al.*, “Nucleation-related defect-free GaP/Si (100) heteroepitaxy via metal-organic chemical vapor deposition,” *Appl. Phys. Lett.*, vol. 102, no. 14, p. 142102, 2013.

[65] I. Németh, B. Kunert, W. Stolz, and K. Volz, “Heteroepitaxy of GaP on Si: Correlation of morphology, anti-phase-domain structure and MOVPE growth conditions,” *J. Cryst. Growth*, vol. 310, no. 7–9, pp. 1595–1601, Apr. 2008.

[66] A. Beyer *et al.*, “GaP heteroepitaxy on Si(001): Correlation of Si-surface structure, GaP growth conditions, and Si-III/V interface structure,” *J Appl Phys*, vol. 111, no. 8, p. 083534, 2012.

[67] Y. Takagi, H. Yonezu, K. Samonji, T. Tsuji, and N. Ohshima, “Generation and suppression process of crystalline defects in GaP layers grown on misoriented Si (1 0 0) substrates,” *J Cryst Growth*, vol. 187, no. 1, pp. 42–50, 1998.

[68] J. A. Piedra-Lorenzana *et al.*, “Estimation of Ga adatom diffusion length for GaP growth by molecular beam epitaxy,” *J. Cryst. Growth*, vol. 512, pp. 37–40, 2019.

[69] M. S. Sobolev *et al.*, “Heteroepitaxy of GaP Nucleation Layers on Si by Molecular Beam Epitaxy,” *Semiconductors*, vol. 52, no. 16, pp. 2128–2131, 2018.

[70] A. A. Lazarenko, M. S. Sobolev, E. V. Pirogov, and E. V. Nikitina, “Doping of GaP layers grown by molecular-beam epitaxy on silicon substrates,” in *Journal of Physics: Conference Series*, 2018, vol. 1124, p. 022022.

[71] R. Saive, H. Emmer, C. T. Chen, C. Zhang, C. Honsberg, and H. Atwater, “Study of the Interface in a GaP/Si Heterojunction Solar Cell,” *IEEE J. Photovolt.*, vol. 8, no. 6, pp. 1568–1576, Nov. 2018.

[72] C. Zhang, E. Vadiee, R. R. King, and C. B. Honsberg, “Carrier-selective contact GaP/Si solar cells grown by molecular beam epitaxy,” *J. Mater. Res.*, vol. 33, no. 4, pp. 414–423, 2018.

[73] M. Vaisman *et al.*, “15.3%-Efficient GaAsP Solar Cells on GaP/Si Templates,” *ACS Energy Lett.*, vol. 2, no. 8, pp. 1911–1918, Aug. 2017.

[74] J.-P. Gauthier *et al.*, “Electrical injection in GaP-based laser waveguides and active areas,” in *26th International Conference on Indium Phosphide and Related Materials (IPRM)*, 2014, pp. 1–2.

[75] C. Robert *et al.*, “Electronic, optical, and structural properties of (In, Ga) As/GaP quantum dots,” *Phys. Rev. B*, vol. 86, no. 20, p. 205316, 2012.

[76] M. Da Silva *et al.*, “GaAsPN-based PIN solar cells MBE-grown on GaP substrates: toward the III-V/Si tandem solar cell,” in *Physics, Simulation, and Photonic Engineering of Photovoltaic Devices IV*, 2015, vol. 9358, p. 93580H.

[77] T. Quinci *et al.*, “Defects limitation in epitaxial GaP on bistepped Si surface using UHVCVD–MBE growth cluster,” *J Cryst Growth*, vol. 380, pp. 157–162, 2013.

[78] P. Y. Wang *et al.*, “Abrupt GaP/Si hetero-interface using bistepped Si buffer,” *Appl Phys Lett*, vol. 107, no. 19, p. 191603, 2015.

[79] P. Y. Wang *et al.*, “Quantitative evaluation of microtwins and antiphase defects in GaP/Si nanolayers for a III–V photonics platform on silicon using a laboratory X-ray diffraction setup,” *J. Appl. Crystallogr.*, vol. 48, no. 3, pp. 702–710, 2015.

[80] H. Li *et al.*, “Engineering CIGS grains qualities to achieve high efficiency in ultrathin Cu(In Ga1−)Se2 solar cells with a single-gradient band gap profile,” *Results Phys.*, vol. 12, pp. 704–711, Mar. 2019.

[81] Y. Takagi, Y. Furukawa, A. Wakahara, and H. Kan, “Lattice relaxation process and crystallographic tilt in GaP layers grown on misoriented Si(001) substrates by metalorganic vapor phase epitaxy,” *J. Appl. Phys.*, vol. 107, no. 6, p. 063506, 2010.

[82] S. Adachi, *Properties of semiconductor alloys: group-IV, III-V and II-VI semiconductors*, vol. 28. John Wiley & Sons, 2009.

[83] F. C. Frank and J. H. van der Merwe, “One-dimensional dislocations. I. Static theory,” *Proc. R. Soc. Lond. Ser. Math. Phys. Sci.*, vol. 198, no. 1053, pp. 205–216, 1949.

[84] J. H. Van der Merwe, “Crystal interfaces. Part I. Semi-infinite crystals,” *J. Appl. Phys.*, vol. 34, no. 1, pp. 117–122, 1963.

[85] J. H. Van der Merwe, “Equilibrium structure of a thin epitaxial film,” *J. Appl. Phys.*, vol. 41, no. 11, pp. 4725–4731, 1970.

[86] K. Yamane, T. Kawai, Y. Furukawa, H. Okada, and A. Wakahara, “Growth of low defect density GaP layers on Si substrates within the critical thickness by optimized shutter sequence and post-growth annealing,” vol. 312, no. 15, pp. 2179–2184, 2010.

[87] O. Skibitzki *et al.*, “GaP collector development for SiGe heterojunction bipolar transistor performance increase: A heterostructure growth study,” *J Appl Phys*, vol. 111, no. 7, p. 073515, 2012.

[88] T. Soga, T. Jimbo, and M. Umeno, “Dislocation generation mechanisms for GaP on Si grown by metalorganic chemical vapor deposition,” *Appl. Phys. Lett.*, vol. 63, no. 18, pp. 2543–2545, Nov. 1993.

[89] A. Konkar, “Origin of the 60 degree and 90 degree dislocations and their role in strain relief in lattice-mismatched heteroepitaxy of fcc materials,” *ArXivcond-Mat0606744*, Jun. 2006.

[90] G. I. Taylor, “The mechanism of plastic deformation of crystals. Part I.—Theoretical,” *Proc. R. Soc. Lond. Ser. Contain. Pap. Math. Phys. Character*, vol. 145, no. 855, pp. 362–387, 1934.

[91] H. Föll, “Defects in Crystals,” *Essentials to Chapter 5.1: Dislocations - Basics*. .

[92] R. M. France, W. E. McMahon, A. G. Norman, J. F. Geisz, and M. J. Romero, “Control of misfit dislocation glide plane distribution during strain relaxation of CuPt-ordered GaInAs and GaInP,” *J. Appl. Phys.*, vol. 112, no. 2, p. 023520, Jul. 2012.

[93] H. Döscher, T. Hannappel, B. Kunert, A. Beyer, K. Volz, and W. Stolz, “In situ verification of single-domain III-V on Si(100) growth via metal-organic vapor phase epitaxy,” *Appl Phys Lett*, vol. 93, no. 17, p. 172110, 2008.

[94] H. Döscher and T. Hannappel, “In situ reflection anisotropy spectroscopy analysis of heteroepitaxial GaP films grown on Si (100),” *J. Appl. Phys.*, vol. 107, no. 12, p. 123523, 2010.

[95] A. Beyer *et al.*, “Atomic structure of (110) anti-phase boundaries in GaP on Si(001),” *Appl Phys Lett*, vol. 103, no. 3, p. 032107, 2013.

[96] P. Farin *et al.*, “Three-dimensional structure of antiphase domains in GaP on Si(0 0 1),” *J Phys Condens Matter*, vol. 31, no. 14, p. 144001, 2019.

[97] A. Létoublon *et al.*, “X-ray study of antiphase domains and their stability in MBE grown GaP on Si,” *J. Cryst. Growth*, vol. 323, no. 1, pp. 409–412, May 2011.

[98] O. Durand *et al.*, “Monolithic integration of diluted-nitride III–VN compounds on silicon substrates: toward the III–V/Si concentrated photovoltaics,” *Energy Harvest. Syst.*, vol. 1, no. 3–4, pp. 147–156, 2014.

[99] T. J. Grassman *et al.*, “Toward metamorphic multijunction GaAsP/Si photovoltaics grown on optimized GaP/Si virtual substrates using anion-graded GaAs y P 1-y buffers,” in *34th IEEE Photovoltaic Specialists Conference (PVSC)*, 2009, pp. 002016–002021.

[100] E. Tea *et al.*, “Theoretical study of optical properties of anti-phase domains in GaP,” *J. Appl. Phys.*, vol. 115, no. 6, p. 063502, 2014.

[101] I. Lucci *et al.*, “Universal description of III-V/Si epitaxial growth processes,” vol. 2, no. 6, p. 060401, 2018.

# Chapitre 2. GaP/Si epitaxy and characterization techniques

This chapter is dedicated to introducing the GaP/Si pseudo-substrate epitaxy and characterization techniques, which are applied in this thesis. Firstly, the epitaxy of the GaP/Si pseudo-substrate by MBE is introduced, which is performed by Tony Rohel et Charles Cornet at Institute FOTON. Then, the setups, the parameters and the data processing methods of several experiments for the characterization of our material are introduced.

## 2.1. Epitaxy of the GaP/Si pseudo-substrate

### 2.1.1. Growth cluster UHV/CVD – MBE

The epitaxy of GaP on Si substrate is performed in the Ultra-High-Vacuum Chemical Vapor Deposition (UHV/CVD) – Molecular Beam Epitaxy (MBE) cluster installed in laboratory FOTON-OHM.

The cluster consists of a Riber UHV/CVD chamber for Si epitaxy and a Riber compact 21 solid source MBE chamber for III-V material epitaxy, which are connected from one to another by an ultra-high vacuum (UHV) tunnel with vacuum on the order of $10^{-9}$ Torr.

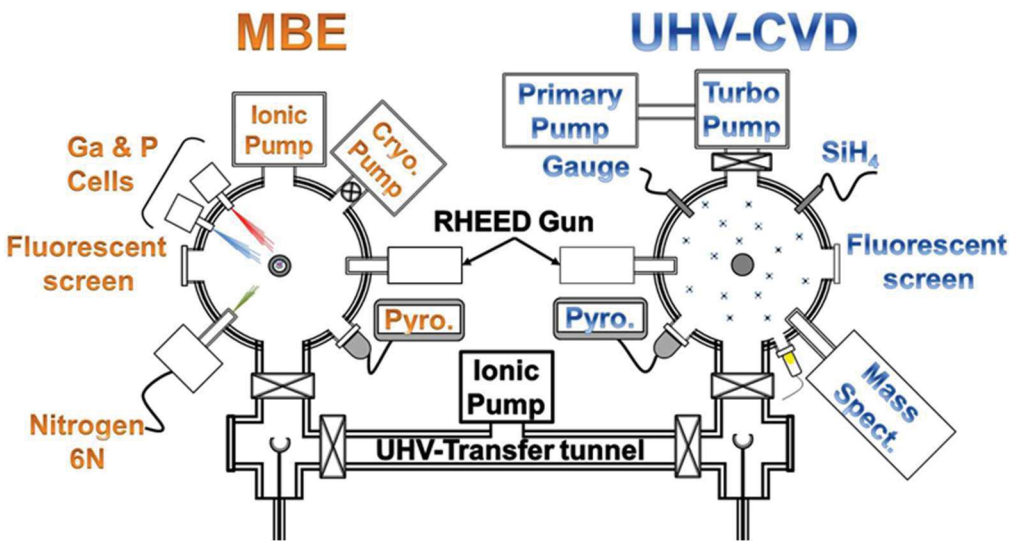


Figure 2-1 UHV/CVD-MBE cluster in FOTON for GaP/Si pseudo-substrate epitaxy.

The growth of III-V materials on Si must be done in separate chambers to avoid any cross-contamination. Indeed, Si is a dopant for III-V materials and vice versa.

The idea of the double-chambers growth cluster for III-V/Si heteroepitaxy was proposed by Yamane et.al. from Toyohashi University of Technology in Japan[1]–[3]. They used an UHV transfer chamber to connect two MBE chambers, and demonstrated a drastic reduction in the contamination between III-V and Si as compared to single-chamber. Subsequently, the group of Volz K. at Philipps Marburg University in Germany and the group of James S. Harris at Stanford University in USA [4]–[6] also developed double-chambers growth clusters, which

consist of MOVPE/MBE and MBE/MBE respectively. The group of Volz K. et.al. at Philipps Marburg University also use the Metal-organic Vapor Phase Expitaxy (MOVPE) after 2008 [7].

### 2.1.2. The preparation of Si wafers

In this work, all the GaP/Si pseudo-substrates are based on 2 inches n-type Si (001) wafers with two flats to indicate the in-plane crystallographic orientation of the substrate. All the Si wafers have vicinal surfaces, and the miscut of the surface are either 4° or 6° towards the [110] direction. Both single-layer step and double-layers step can be formed on these vicinal surfaces. The average length D of the terraces for single layer and double layer steps can be respectively calculated as below:

$$\mathrm{D_{single}} = \frac{\mathrm{a}}{4tan(\alpha)} \tag{2.1}$$

$$\mathrm{D_{double}} = \frac{\mathrm{a}}{2tan(\alpha)} \tag{2.2}$$

where a is the lattice constant of Si and $\alpha$ is the miscut angle. For 4° miscut, the length of the terraces for the single layer and double layer is 1.95 nm and 3.90 nm, respectively. For 6° miscut, the length is 1.27 nm and 2.59 nm, respectively. The steps have been considered to prevent or lower the formation of the APDs [8]–[11].

Before the epitaxy of GaP, the silicon wafer is cleaned with the “optimized HF process”, which is introduced in ref [12]. The cleaning process is used to remove the carbon, oxide, metallic and organic impurities at the Si surface prior to the GaP epitaxy. After the preparation, the Si wafer will be immediately transferred into the MBE chamber and heated to 800 °C to dehydrogenation. Then, the wafer will be cooled down for the epitaxy of GaP. The descriptions of the growth of the different GaP/Si studied during my PhD work will be given in the following, directly in the corresponding chapters.

## 2.2. X-ray diffraction characterization

X-ray diffraction (XRD), which is also called X-ray crystallography (XRC) when it is applied in the crystallography, may be the most widely used technique to measure the atomic and molecular structural information of a crystal. In XRD, a beam of X-ray is sent into the crystal. Then, the parameters of the diffraction beams are measured, for instance, the intensity, the

scattering width, the angle, the phase and so on. An analysis on these parameters can provide the structural information, such as the crystal structure type, the defect distribution in the sample and so on.

### 2.2.1. X-ray diffraction setup

The laboratory X-ray diffraction experiments are performed by using a 4-circle Bruker D8 X-ray Diffractometer (horizontal scattering plane geometry), localized in the Institut des Sciences Chimiques de Rennes (ISCR) at The Rennes 1 University. This diffractometer is equipped with a 1D Gobel Multi-layer Mirror placed on the linear focus window of a standard sealed tube as primary optics. The power of the X-ray source is usually set at 40kV and 40mA. There are two setup modes applied in this thesis, i.e. the low-resolution mode (show in Figure 2-2) and the high-resolution mode(show in Figure 2-3). In general, the low-resolution mode is applied in the quick θ/2θ scan and the Pole Figure (PL), and the high-resolution mode is applied in the θ/2θ scan and the Reciprocal Space Mapping (RSM).

In the low-resolution mode, the linear beam focus is 12mm wide in height at source. The X-ray beam passes through an 1mm wide source slit and a 5mm vertically wide anti-scattering slit, which is often installed to limit the vertical width to be smaller than the sample dimensions, before reaching the sample surface. On the other side, an anti-scattering slit of 8 mm horizontal height and 15 mm vertical width and a Soller slits of 2.5° are used to decrease the intensity of the background signal. An optional Ni filter is inserted between the anti-scattering slit and the Soller slits to lower the Cu-$K_\beta$ intensity and, therefore, to select the Cu-$K_\alpha$ with a wavelength of 1.5418 nm. A 180 channels 1D position sensitive detector Lynxeye™ positioned at 300mm from the goniometer center works like a point detector in this mode. The flux intensity from the selected pixels is summed as the final intensity.

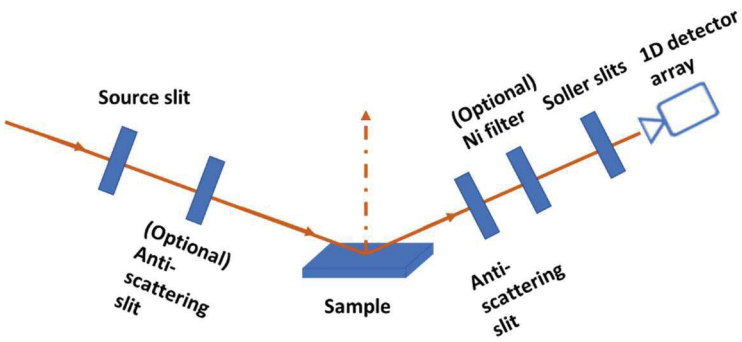


Figure 2-2 Schematic diagram of the lab setup X-ray diffractometer in the low-resolution mode.

While in the high-resolution mode, the cross slit and the Ni filter are replaced by a 4-bounce Ge (022) asymmetric monochromator (Bartels), which can reduce the divergence of the X-ray beam down to 29 arc-seconds (0.008°) and also to select the Cu-$K_{\alpha 1}$ with a wavelength of 1.540562 nm. The angular width on the 1D array is 2.6° in 2θ.

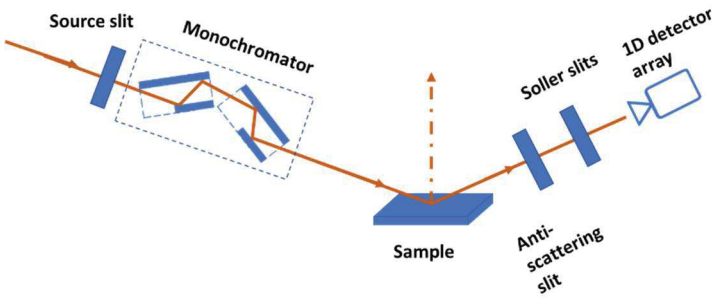


Figure 2-3 Schematic diagram of the lab setup X-ray diffractometer in the high-resolution mode.

The 4-circle diffractometer permits four rotational degrees of freedom, for instance, they are ω, 2θ, ϕ and χ. The goniometer also permits basic translations in the direct space x, y and z. A schematic diagram of the goniometer geometry is shown as Figure 2-4.

- ω – the incident angle between the X-ray beam and the direction x, i.e. the rotation angle of the sample around the axis y.
- 2θ – the angle between the CCD array and the incident beam.
- ϕ – the rotation angle around the vertical axis z.
- χ – the ration angle around the axis x.

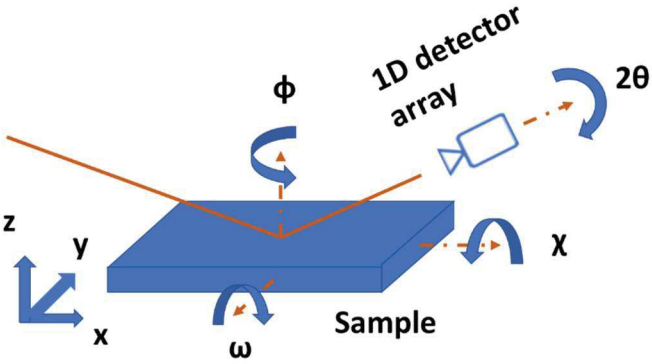


Figure 2-4 Goniometer geometry of the XRD lab setup with four rotational degrees of freedom.

### 2.2.2. Longitudinal scan

The longitudinal scan is a widely used method in XRD for the characterization of epitaxially grown semiconductors. All the four rotational degrees of freedom, i.e. ω, 2θ, ϕ and χ, can be used in the longitudinal scan, while the most common methods applied in this thesis are rocking curve scan (scan in omega with an open detector), transverse scan (also called ω scan, used with either a rear optic) and ω/2θ scan.

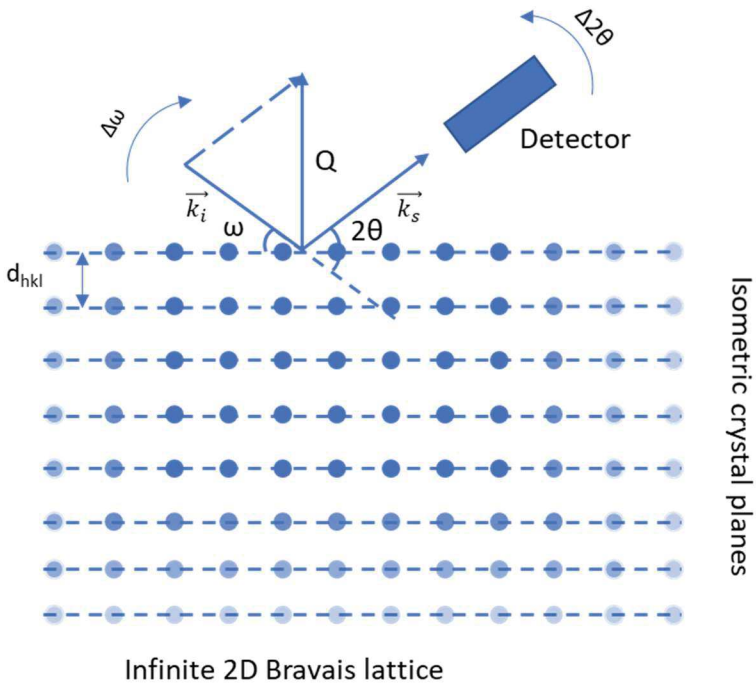


Figure 2-5 Schematic diagram of ω/2θ longitudinal scan.

In general, the thin epitaxially grown semiconductor studied by using ω/2θ longitudinal scan is always simplified as an infinite array of atoms located at a series of isometric crystal planes, i.e. the crystal plane family. A schematic diagram of the ω/2θ scan experiment is shown in Figure 2-5. The distance $d_{hkl}$ between the isometric crystal planes are determined by the crystal system and corresponding diffraction direction given by the diffraction vector direction $\vec{Q}$.

For cubic structure, such as Si or GaP:

$$d_{hkl} = \frac{a}{\sqrt{h^2 + k^2 + l^2}} \tag{2.3}$$

where a is the lattice constant, and (h, k, l) are the Miller indices.

For tetragonal structure, such as Copper Indium Selenide (CIS) or Copper indium gallium (di)selenide (CIGS), studied in the chapter 4:

$$d_{hkl} = \frac{1}{\sqrt{\frac{h^2 + k^2}{a^2} + \frac{l^2}{c^2}}} \tag{2.4}$$

where ***a*** and ***c*** are the lattice constants and ***(h, k, l)*** are the Miller indices.

The X-ray diffraction pattern is obtained by the interference of the scattering waves from the atoms located at the crystal lattice nodes. The vector of the incident source beam and the scattering beam directions are defined as $\overrightarrow{\boldsymbol{k_i}} = \frac{\boldsymbol{2\pi}}{\boldsymbol{\lambda}}$ and $\overrightarrow{\boldsymbol{k_s}} = \frac{2\pi}{\lambda}$ respectively, where $\lambda$ is wavelength of the X-ray source beam. Then the norm of the scattering vector $\vec{\boldsymbol{Q}}$ is:

$$\|\vec{Q}\| = \|\overrightarrow{k_i} - \overrightarrow{k_s}\| = \frac{4\pi sin\theta}{\lambda} \tag{2.5}$$

In addition, the Bragg's law is written as:

$$2d_{hkl}\sin\theta = n\lambda \tag{2.6}$$

, ***n*** being a positive integer, termed the diffraction order

Combining Equation (*2.5*) and Equation (*2.6*), we can express the diffraction vector modulus $\|\vec{\boldsymbol{Q}}\|$ for the first order of the diffraction as $\frac{2\pi}{d_{hkl}}$.

#### 2.2.2.a. Rocking Curve Scan

In a typical rocking curve scan, the ω and 2θ should be firstly fixed at (004), (111) or other specific diffraction directions. Then the sample is rotated by a small angle Δω around the initial ω, while the 2θ is fixed. The rocking curve scan is primarily used to study defects, such as dislocation density [13], mosaic spread [14], curvature [15], misorientation [16], and inhomogeneity [17]. When the slits are widely open, the tilt of the mosaics and the lattice strain cannot be separated in the rocking curve.

#### 2.2.2.b. Transverse scan

The transverse scan is also called the Δω scan. The setup of the transverse scan is nearly the same as the rocking curve scan. The only difference is that the slits are nearly closed, so that only the center part of the beam can be collected by the detector. As the Δω is small, the $\Delta\vec{Q}$ should be nearly parallel to the lattice plane and $\Delta\|\vec{Q}\|$ is approximate to $\frac{4\pi\Delta\omega\sin\theta}{\lambda}$. The transverse scan is sensitive to the mosaicity, and the lateral correlation length of the defect.

#### 2.2.2.c. ω/2θ Scan

The ω/2θ scan in XRD is usually used to determine the basic crystal structure of semiconductor materials. In a typical ω/2θ longitudinal scan, the ω and 2θ should be firstly fixed to ensure the scattering vector $\vec{Q}$ vertical to the lattice plane. Then, the sample will be rotated by an angle Δω, accompanied by a rotation Δ2θ = 2Δω of the detector. Thus, the scattering vector shift $\Delta\vec{Q}$ will be vertical to the lattice constant planes during the ω/2θ scan and $\Delta\|\vec{Q}\|$ is equal to $\frac{4\pi\sin(\Delta\theta)}{\lambda}$.

As the diffraction maximum is achieved when and only when the order of the diffraction n is equal to a positive integer, the ω/2θ scan will show separated characteristic peaks, which are corresponding to different diffraction plane family, which belong to the same direction, with specific Miller indices (h, k, l). A ω/2θ Scan performed on a CIGS thin layer grown on a GaP/Si pseudo substrate is shown in Figure 2-6. Through these characteristic peaks, one can extracted many structural information, for instance the crystal system and the lattice constant.

The relaxation rate of the epitaxial layer can also be measured by the ω/2θ Scan. For simple, here the material with cubic structure is discussed as an example. Based on Equation (1.1) and (2.6), the experimental out-of-plane lattice constant $a_{STR}$ of the epitaxial layer should be:

$$a_{STR} = \frac{n\lambda}{2\sin\theta}\sqrt{h^2 + k^2 + l^2} \tag{2.7}$$

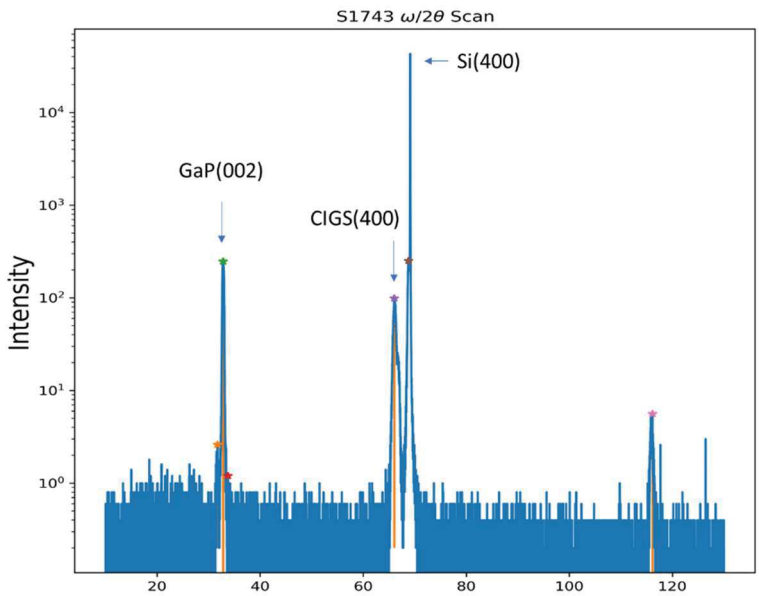


Figure 2-6 ω/2θ Scan on CIGS grown on GaP/Si pseudo substrate.

where n is equal to 1 for the first order diffraction maximum, $\lambda$ is the wavelength of the X-ray source, $\theta$ can be measured in the ω/2θ scan, and the (h, k, l) are the Miller indices.

When the epitaxial layer has a larger (or smaller) lattice constant than the substrate, it undergoes compressive stresses (respectively tensile stresses). In the fully strained case, the in-plane lattice constant of the epitaxial layer $a_{\parallel}$ is equal to the lattice constant of the substrate $\boldsymbol{a_{sub}}$, while the fully relaxed lattice constant is given by $\boldsymbol{a_{relax}}$. The relaxation rate x can be expressed as [18]:

$$x = \frac{a_{\parallel} - a_{sub}}{a_{relax} - a_{sub}} \tag{2.8}$$

According to the generalized Hooke's law, the in-plane lattice constant $a_{\parallel}$ and out-of-plane lattice constant $a_{\perp}$ for isotropic materials with the cubic crystal structure within the range of elastic deformation has a relationship as below:

$$a_{\parallel} - a_{relax} = -\frac{C_{11}}{2C_{12}}(a_{\perp} - a_{relax}) \tag{2.9}$$

where $\boldsymbol{C_{11}}$ and $\boldsymbol{C_{12}}$ are the elastic stiffness constants.

Thus, the relaxation rate x is:

$$x = 1 - \frac{C_{11}}{2C_{12}} \frac{a_{\perp} - a_{relax}}{a_{relax} - a_{sub}} \tag{2.10}$$

### 2.2.3. Reciprocal Space Mapping

#### 2.2.3.a. Reciprocal Space and Ewald's Sphere

A crystal can be described as a periodic arrangement made with a pattern which consists of one or more atoms and a lattice point called Bravais lattice which describes the periodic arrangement of the pattern. A 3D expression of the Bravais lattice $R$ is as below:

$$\overrightarrow{\boldsymbol{R_n}} = n_1\overrightarrow{a_1} + n_2\overrightarrow{a_2} + n_3\overrightarrow{a_3} \tag{2.11}$$

where $n_i$ can be any integers and $\overrightarrow{a_i}$ is the primitive vector in x, y, z directions.

The reciprocal space represents the Fourier transform of the real Bravais lattice. Then the reciprocal vector $\vec{\boldsymbol{G}}$ is:

$$\vec{\mathbf{G}} = h\overrightarrow{b_1} + k\overrightarrow{b_2} + l\overrightarrow{b_3} \tag{2.12}$$

where $\overrightarrow{b_i}$ satisfy the formulas as below:

$$\overrightarrow{b_1} = 2\pi\frac{a_2 \times a_3}{a_1 \cdot (a_2 \times a_3)} \tag{2.13}$$

$$\overrightarrow{b_2} = 2\pi \frac{a_3 \times a_1}{a_2 \cdot (a_3 \times a_1)} \tag{2.14}$$

$$\overrightarrow{b_3} = 2\pi \frac{a_1 \times a_2}{a_3 \cdot (a_1 \times a_2)} \tag{2.15}$$

and the indices ***(h, k, l)*** are the Miller indices. Thus, we have $\|\boldsymbol{G_m}\| = \frac{1}{d_{hkl}} = \frac{\|\vec{Q}\|}{2\pi}$.

As the Bravais lattice has symmetry, the reciprocal lattice is also composed of discrete points with symmetry defined by Equation (2.13)(2.14) and (2.15). For example, the reciprocal lattice of the simple cubic crystal is also a simple cubic structure. The Ewald sphere is proposed by Paul Peter Ewald to characterize the X-ray diffractions, which is shown in Figure 2-7.

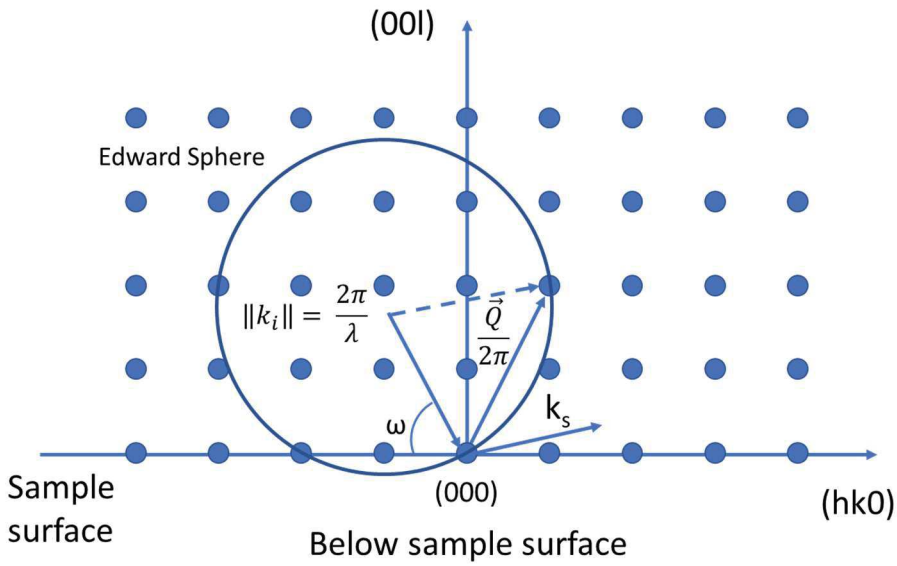


Figure 2-7 2D Reciprocal Space and Edward sphere diagram of a simple cubic structure crystal.

The radius of Edward sphere is $\frac{2\pi}{\lambda}$, so that the endpoints of the incident vector and the diffraction vector fall at the sphere. The incident vector $k_i$ always point from the center of Edward sphere to (000). So, when the incident angle is changed, the Edward sphere is also rotated around the (000). $\boldsymbol{k_s}$ is a direction of diffraction if the endpoint of Q/2π lies on a reciprocal lattice point. Therefore, the diffraction conditions are fulfilled when a reciprocal

lattice point intercepts the Ewald sphere. Thus, a diffraction experiment usually consists of rotating the Ewald sphere, or the crystal, in order to fulfill the diffraction conditions.

While, in the real world, there is no unlimited crystal. As the reciprocal space is the Fourier transformation of the real space, a perfect cubic crystal with limited physical size $(\mathrm{a}, \mathrm{b}, \mathrm{c})$ will be a 3D object in the reciprocal space, which have a size approximate to $(\frac{1}{a}, \frac{1}{b}, \frac{1}{c})$. This is the contribution of the limited crystal size to the width of peak diffraction spot.

2.2.3.b. Reciprocal space mapping

Reciprocal space mapping (RSM) consists of mapping the intensity around a reciprocal space zone by performing a series of scans along 2θ for a set of ω values. For heteroepitaxial layer, the traditional RSMs are usually performed on (00L), (113) and (224) Bragg reflections. The scans along the (00L) diffraction peaks give information along the growth direction while the (113) and (224) displays also in-plane information.

We define the 2D Q coordinate system as below:

$$\begin{cases} \mathrm{Q}_x = \frac{2\pi}{\lambda}(cos\,\omega - cos(2\theta - \omega)) = \frac{4\pi}{\lambda} sin\theta\, sin(\theta - \omega) \\ \mathrm{Q}_z = \frac{2\pi}{\lambda}(sin\,\omega + sin(2\theta - \omega)) = \frac{4\pi}{\lambda} sin\theta\, cos(\theta - \omega) \end{cases} \qquad (2.16)$$

where $(Q_{\mathrm{x}}, Q_z)$ is the coordinate of the diffraction point, $\lambda$ is the wavelength of the X-ray beam.

For simple, the (00L) diffraction is discussed as an example. Here, we define the nominal crystal plane family to be parallel to the crystal surface, which means $\theta = \omega$, which is corresponding to the sample grown on nominal substrates instead of vicinal substrates. The imperfection of the crystal structure changes the center position of the diffraction spot through changing the Bragg angle (i.e. $\mathrm{d}_{\mathrm{hkl}}$) and introduce a tilt, which impacts the average sample surface.

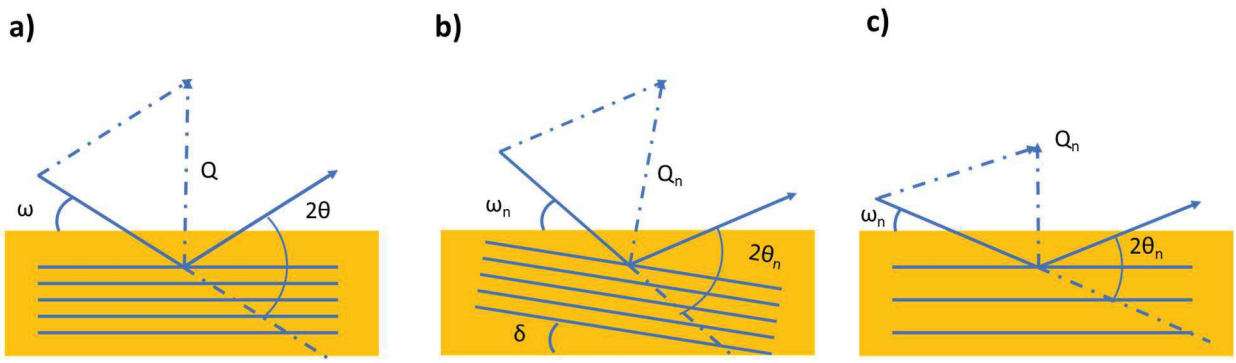


Figure 2-8 Schematic diagram of a) a normal crystal plane family b) a crystal plane family a tilt or c) with a different lattice constant, i.e. a strain state.

The schematic diagram of two simple models with a tilt and a strain state compared the normal crystal plane family are shown in Figure 2-8 (b) and (c). While, there are usually much more than one pf these specific cases in the scanning area of the XRD. So, the superposition of the diffraction patterns leads to a broadening of the diffraction spot's size, and/or a shift of the center position of the diffraction spot.

For the two simple models shown in Figure 2-8 (b) and (c), the position of the scattering spot in the reciprocal space can be calculated as follows.

As $\omega_n = \omega + \delta$ and $\theta_n = \omega_n$, the center of the Q scattering spot can be calculated as below, where $\boldsymbol{\delta}$ is the tilt angle:

$$\begin{cases} Q_{xn} = \frac{4\pi}{\lambda} sin\theta_n \, sin(\theta_n - \omega_n) = Q\sin(-\delta) \\ Q_{zn} = \frac{4\pi}{\lambda} sin\,\theta_n \, cos(\theta_n - \omega_n) = \; Q\cos(-\delta) \end{cases} \qquad (2.17)$$

with

$$Q = \frac{4\pi}{\lambda}\sin\frac{2\theta}{2}$$

where $\frac{2\theta}{2}$ is the Bragg angle and $\delta$ is the tilt angle.

For a strained crystal, comparing to the bulk material, the Bragg angle $\frac{2\theta}{2}$ will change to $\frac{2\theta_n}{2}$ according to the Bragg law, due to the change of $d_{hkl}$, i.e. the lattice constant. Thus, the center of the Q scattering spot is:

$$\begin{cases} Q_{xn} = 0 \\ Q_{zn} = \frac{4\pi}{\lambda} sin \frac{2\theta_n}{2} \end{cases} \tag{2.18}$$

In conclusion, the center position of the scattering spot is determined only by the interrelated distance $d_{hkl}$ and the tilt angle. The distance change will influence the norm of the diffraction vector and the tilt will rotate the diffraction vector, which is shown in Figure 2-9.

While, in the RSM, the beam size is usually much larger than correlation length between defects, so that the scattering spot is the sum of the diffraction from many coherent domains called crystallites (or mosaics in some cases). The influence of the defects is shown as broadening and shift in different directions instead of simple position shift. So, the broadening of the scattering spot is the result of both the limited crystallite size, which is discussed above, and the defects.

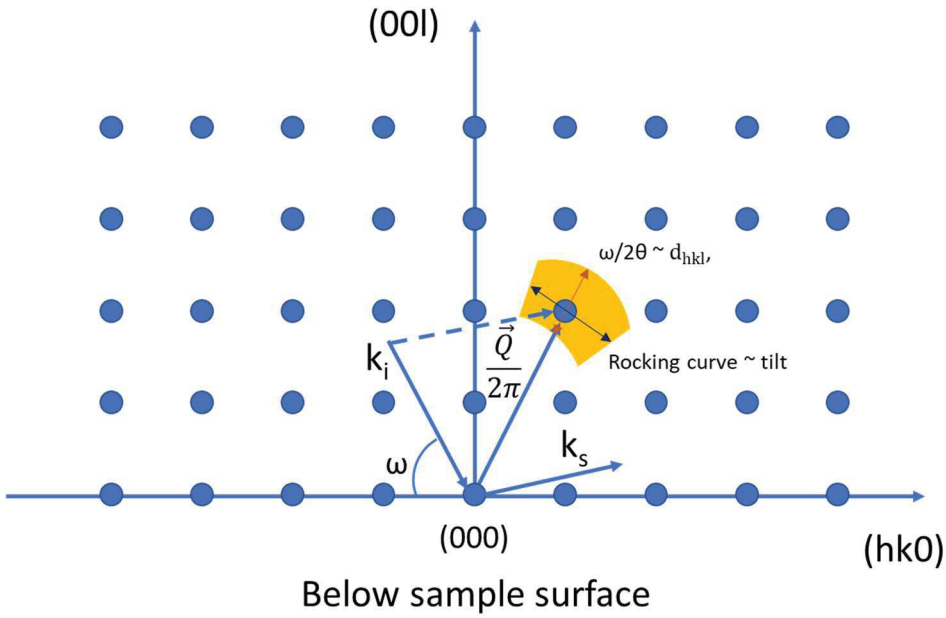


Figure 2-9 Schematic diagram of relationship between RSM and crystal plane parameters $d_{hkl}$ and tilt $\delta$.

For the (113) or (224) Bragg diffraction, the nominal plane family are not parallel to the crystal upper surface. Then, these diffractions can be considered as (00L) diffraction with a general tilt angle equal to $\delta = \arctan(\frac{l}{h})$, and be discussed with the same method. To investigate these diffractions, the incident angle should be set around $\frac{2\theta}{2} + \delta$ to cover the region of interest in the reciprocal space.

### 2.2.4. Pole Figure

Similar to RSM, pole figure consists of mapping the intensity around a series of ϕ and χ values, when 2θ is fixed to select a crystal plane family. Pole figure describes the symmetry of the crystal. A crystal can be described by the angles between the crystallographic directions so that a good representation of the crystal must be based on a "picture" of these angles.

In theory, a ϕ and χ mapping with a fixed incident angle ω can be equivalent to a ω and 2θ mapping with a fixed ϕ value. But in practice, the pole figure usually has larger detection range while lower resolution compared to 2D RSM.

The origin of the stereographic projection comes from a three-dimensional sphere with the crystal located at its center. An example of the {100} 3D pole sphere for a cubic crystal is shown as

Figure 2-10. The sample is located at the center of sphere, and each (ϕ, χ) pair is corresponding to a normal plane through the center. The poles are the intersection between the normal plane and the sphere.

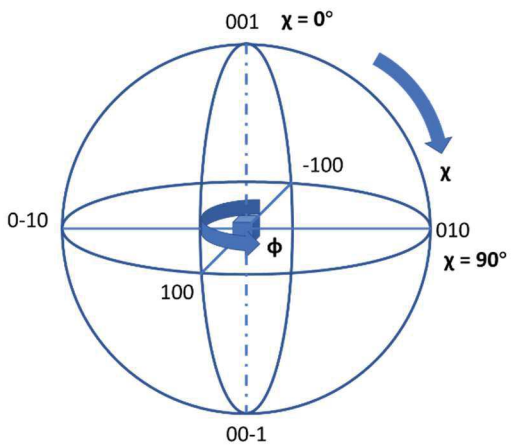


Figure 2-10 Spherical projection of the {100} poles of a cubic crystal.

For convenience, the 3D pole sphere is usually projected into a plane (stereographic projection) along one direction, which is shown in Figure 2-11, while preserving the angular relations. The stereographic projection is then on the equatorial plane of the sphere. The integrated 2D plotting is called pole figure, which is shown like Figure 2-12. [19]

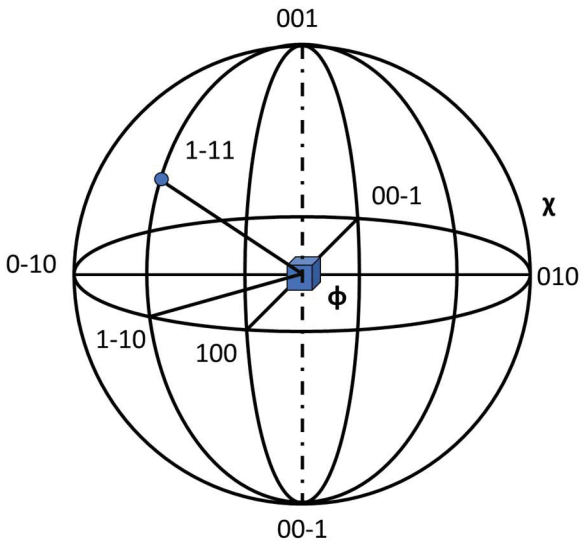


Figure 2-11 Example of stereographic projection of a cubic crystal.

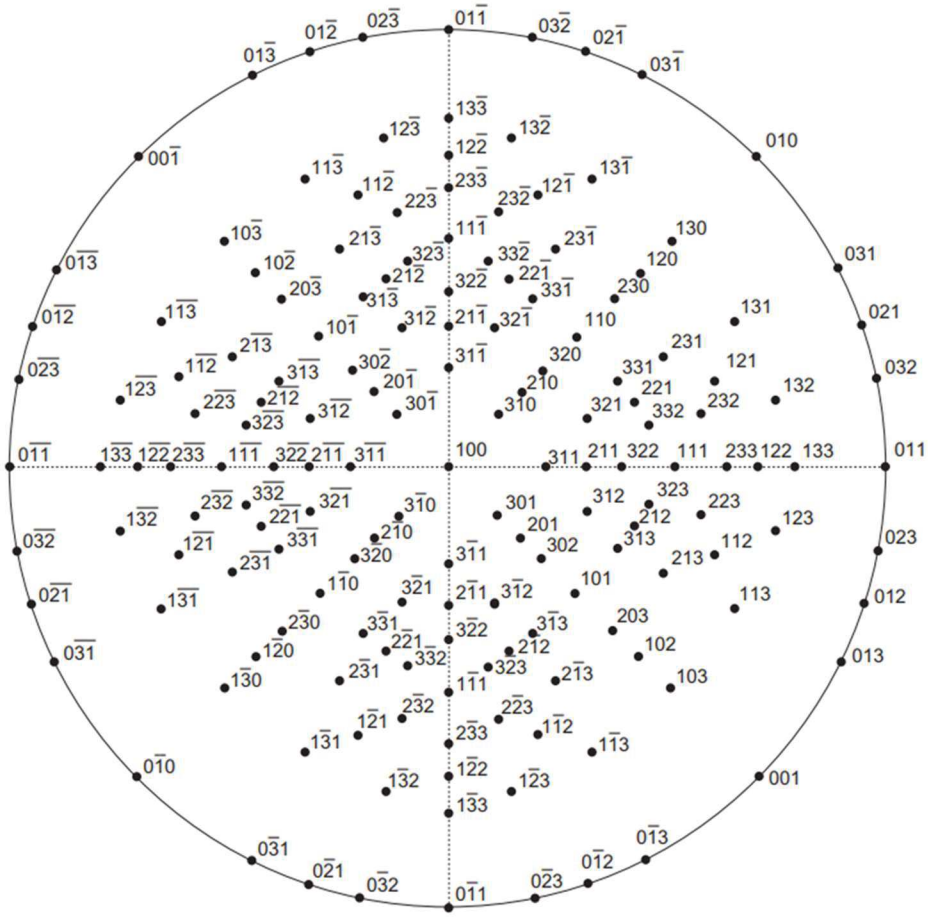

Figure 2-12 Example of a pole figure. [19]

The most traditional application of pole figure is to determine the crystallographic texture. The texture refers to the distribution of the crystallographic orientations of the mosaics in material science. The more consistent the crystallographic orientations are, the stronger the texture is. While in the case of GaP/Si pseudo-substrate, pole figure has two applications[12], [20]:

1. Characterization of the quality of GaP heteroepitaxial layer.
2. Characterization of the MTs.

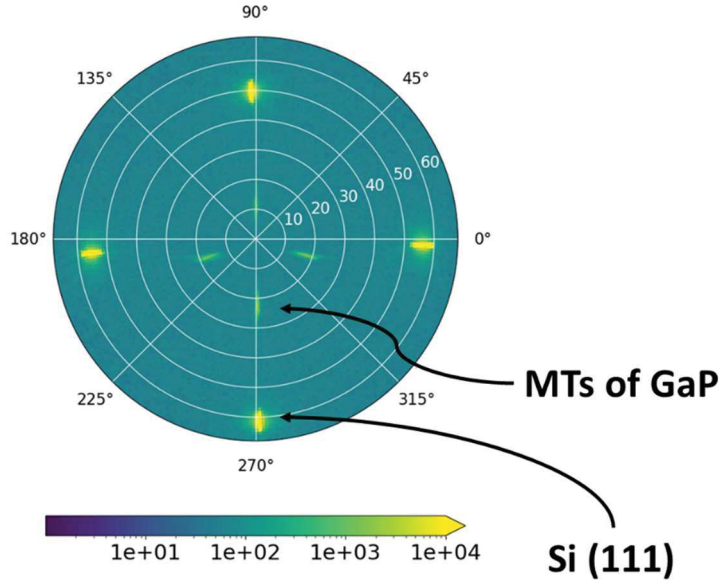


Figure 2-13 Example of pole figure using the plane {111} for GaP/Si (6° miscut) pseudo-substrate.

An example of pole figure using the plane {111} for GaP/Si (6° miscut) pseudo-substrate is shown as Figure 2-13. Because of the small difference between the lattice constant between GaP and Si in room temperature, the Si and GaP (111) diffraction overlap each other. The Si substrate diffraction peaks are always thinner and much more intense than the diffraction peaks from the GaP heteroepitaxial layer. Otherwise, the GaP (111) will become a large but weak background scatter spot. The micro-twins in GaP/Si pseudo-substrate have privileged orientations as stated in 1.4.2. Thus, the pattern of MTs can be observed and measured in pole figures. A detailed report about the quantification of MTs though pole figures can be found in Ref [20], [21].

### 2.2.5. Sub-Micrometer-Beam Scanning Synchrotron X-Ray Diffraction

#### 2.2.5.a. Synchrotron X-Ray

Synchrotron X-ray is an extremely powerful synchrotron radiation with many properties, for instance, high-brilliance and flux, wide energy spectrum, short pulses, high collimation and high polarization. It is produced by the relativistic electrons during circling around the synchrotron. When the direction of the accelerated electrons is changed in the circling synchrotron, thin beam X-ray will be emitted towards the tangent direction [22]. According to the lightsources.org, there has been 50 synchrotron sources in the world [23].

Up to now, there has been four generations of synchrotron radiation sources (SRS). The first-generation SRSs parasitically used the cycling electron synchrotrons developed for particle physics, which were developed between the early 1950s to the early 1970s. After several years running, the storage ring was added to the system as a great advance, which marks the maturity of the first-generation SRSs. While, the X-ray emitted from the synchrotron is an undesired energy loss in particle physics, so the demand of particle physics for the synchrotron is partially opposite to the demand of synchrotron X-ray source. The dedicated SRSs were designed to mainly produce synchrotron radiation. The first second-generation SRS was built at the Daresbury Laboratory in the UK in around 1970. The main improvement for the second-generation SRSs is the insertion devices, for instance, wigglers and undulators. Although the flux density is only determined by the design of the synchrotrons and cannot be improved by any optical technique, the insertion devices help concentrate the energy into one or a few spectrally narrow peaks in the spectrum by introducing constructive interference effect. The third-generation SRSs were born by effectively combination with the insertion device. The third-generation SRSs often adopt NSLS two-ring model and can produce either soft or hard X-ray radiation. The European Synchrotron Radiation Facility (ESRF) in Grenoble, France is the first third-generation SRS. [24]–[28]

Today, there are tens of third-generation SRSs operating all over the world, such as ESRF in Grenoble/France, APS in Argonne/Illinois/USA, SPring-8 in Sayo/Japan, ELETTRA in Trieste/Italy, and et.al.

The next-generation SRSs have been developed for 10s of years and primarily installed in several sites, such as SwissFEL, LCLS and European XFEL. Different from the third-generation SRSs, the fourth-generation SRSs produce X-Ray Free-Electron Laser (XFEL). Through Self Amplified Spontaneous Emission (SASE), the X-ray beam generated in the fourth-generation SRSs can be 10000 times brighter than the X-ray beam in the third-generation SRSs and can keep coherence.

#### 2.2.5.b. The nano- /sub-micrometer-beam synchrotron X-ray

In the traditional X-ray diffraction, the scattering spots of several micrometers are always much larger than the normal size of the structural defects in the samples. So, the analysis is

performed based on the statistical average of large density of defects, comparing to the theoretical model.

In the last decade, the directly observation of the local structure comes true with an application of hard X-ray nanobeams of the order of several hundreds of nanometers, or even tens of nm recently [29]. The most important two challenges in the development of the X-ray nanobeams are the X-ray optics and X-ray source.

To get nano- /sub-micrometer- hard X-ray beam, the first question is how to focus the X-ray beam. There are three main types of X-ray focusing system, i.e. the reflective system, the refractive system and the diffractive system [30].

For the reflective system and the refractive system, the principle challenge is that the interactions between the X-ray and most of the material are weak. Thus, the reflective mirrors in the X-ray focusing system need be coated with multilayers [31]. The reflective mirrors themselves are usually made by dynamical bended Si substrates. Several designs have been proposed to realize the nano-/sub-micrometer- hard X-ray beam with the reflective mirrors [32], [33]. The horizontal and vertical beam are usually focused with two separated mirrors to satisfy the demand of the optical aberration. The complex optical path design and the difficulty in the mirror manufacture lead the reflective system impractical for the nano- /sub-micrometer- hard X-ray beam.

In opposition to the visible light, the refractive indexes of many materials are only slightly below 1 for hard X-ray beam. The low refractive indexes demand the X-ray to have only low angles of incidence, otherwise the X-ray will pass through the lens without any change in the direction. The idea of concave refractive lenses is proposed by Kirkpatrick and furtherly developed Suehiro et.al., Yang et.al. and Snigirev et.al. [34]–[37]. The refractive lenses in use now are mainly Compound Refractive Lenses (CRLs), which are made by beryllium or aluminum. Compared to reflective mirrors, the refractive lenses are more stable and easier to install and align. Due to the background noise, the CRLs made of beryllium or aluminum is less practical for nano- /sub-micrometer- beam. The alternatives are mono-crystalline silicon [38] and polymers [39], which reduce the background noise but also reduce the physical apertures as a trade-off.

The diffractive system is the youngest system among these three and was proposed in the 1960s [40]. This system is extremely suitable for the nano-beam/sub-micrometer- beam, because the high aspect ratios of the zone plates. Because the higher the aspect ratio is, the shorter the focusing distance is. Thus, the losses of the intensity can be reduced. While, the single zone plate with high aspect ratio is only used in the soft X-ray beam, because of the tendency of zone collapse and the lifetime issues. For hard X-ray beam, the diffractive "lens" consists of multi-layers sputtering deposited. This technique decreases the fabrication difficulty, increases the lifetime, but demands a much longer fabrication time [41].

As the useful flux intensity is approximately inversely proportional to resolution, the nano-beam/sub-micrometer-beam X-ray demands stable X-ray beam with high flux, high collimation and low beam divergence. The SRSs are the most suitable source which satisfy all these requirements. As a result, the nano-/sub-micrometer- beam diffraction have been performed in nearly all the main third-generation SRSs, such as APS [42], [43], ESRF [44], SPring-8 [45], MaxIV [46], NSLSII [47].

#### 2.2.5.c. The quicK continuous Mapping

The quicK continuous Mapping (K-Map) is a non-destructive sub-micrometer-beam scanning X-ray diffraction method, developed by Chahine et.al. at ID01-ESRF beamline [48]. This technique provides large-scale local structure information by the X-ray diffraction mapping with high resolution in a short time. Up to now, K-Map has been used to characterize organic electronic devices[49] and to study the defects in the heteroepitaxy structure [50]–[52]. The setup is improved by the staff of ID01 after 2014. Beam typical dimensions will be smaller in the next version. The detail of the experiment setup of K-Map will be discussed in the Chapter 3 for our sample.

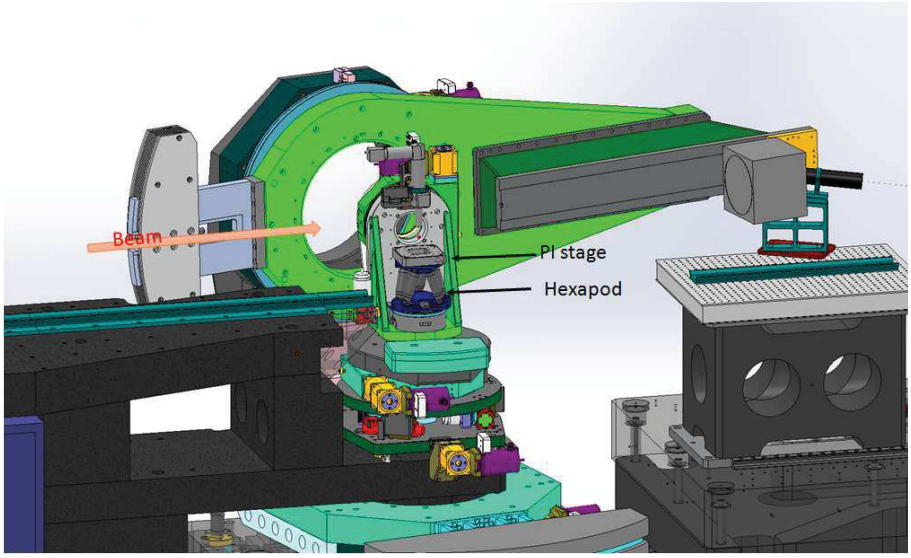


Figure 2-14 Sketch of the beamline ID01 diffraction experimental setup. [48]

The highly focused beams at ID01 can support many X-ray techniques, such as nano-diffraction mapping(K-Map), coherent diffraction imaging (CDI), full-field diffraction microscopy, grazing-incidence diffraction and small-angle scattering. [53]

## 2.3. Other Characterization Methods

Besides X-ray, other optical characterization methods are also applied in the thesis, including micrometer Photoluminescence scanning (Micro-PL), Atomic Force Microscope (AFM) and Transmission Electron Microscope (TEM).

### 2.3.1. Atomic Force Microscope

Atomic force microscopy (AFM) is an important non-destructive and fast tool to probe the topography of the sample. It can quantitively measure the local surface information, at an atomic scale, such as the roughness. The critical part of the AFM is a tip attached to a deformable cantilever. The nano-scale radius of curvature of the tip ensures a lateral accuracy of around 20 nm, while the height accuracy is better than an atomic step. When the curvature of the tip approaches the surface to be measured, the cantilever will bend due to the force between the surface and the tip. Then the bending will be measured to calculate the topography.

At Institute FOTON, a 2007 Veeco™ AFM is used for GaP/Si pseudo-substrates. The maximum imaging size is 100 x 100 $\mu m^2$ with about 6 µm in height. A beam of laser is focused on the top

of the cantilever, and the bending of the cantilever is measured by four quadrant photodiode detectors through the position of the reflection beam. The movement on the sample along x and y is realized by a cylinder-shaped piezoelectric tube, which can shrink and expand controlled by the applied voltage. A loop system controls the movement along z according to the signal received in the photodiode detector to avoid hard interaction between the tip and the sample surface.

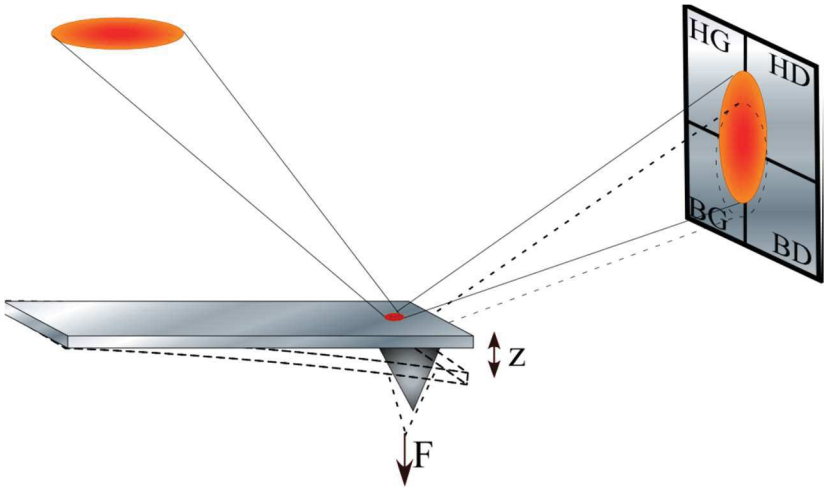


Figure 2-15 Schematic diagram of the photodiode detector system.

There are two basic working modes for this system: tapping and contact modes, and only the tapping mode is applied for the samples in this work.

Compared to contact mode, the tapping mode avoids a strong interaction between the tip and the sample surface. Instead, the cantilever vibrates in high frequency above the sample surface, so that the tip-surface interaction is intermittent. The amplitude of the vibration is highly sensitive to the force between the tip and the surface, and the change of the amplitude will be recorded by the photodiode detector system. The most important advantage of this working mode is to minimize the charge error, which is introduced by the slightly negative charge of the AFM tip .

### 2.3.2. Transmission electron microscope and Scanning Transmission electron microscope

Transmission electron microscope (TEM) is an effective method to observe the fine structure of the sample. The mechanism of TEM is just like the optical microscope, while the optical

beam is replaced by a beam of electrons. The wavelength of the matter wave of electrons is much shorter than the wavelength of photons, so the TEM can exceed the resolution limitation of the optical microscope. The maximum resolution of the TEM can reach 0.05 nm, but the heavy work in the preparation and the analysis steps limit the application of TEM.

The Scanning Transmission electron microscope (STEM) is an improved technique of the traditional TEM, by scanning the sample pixel by pixel with a focused electron beam and a very small probe. Compared to traditional TEM, STEM is performed with a focused electron source which scanning the sample surface and can provide the structural information in a higher contrast. While, the phase information is always lost in STEM due to the incoherent and inelastic beam as a cost.

There are two major working mode in TEM: the imaging mode and the diffraction mode, while only imaging mode is applied in STEM. In the imaging mode, the beam can be controlled by an objective aperture located between the objective lens. If the center part of the beam is selected, the transmitted direct beam contributes to the imaging, and thick areas, heavy atoms and diffracting crystalline areas appear with dark contrast. This mode is called Bright field. Otherwise, the transmitted direct beam can be blocked. Thus, the diffracted beam is selected, and the planar defects or particle sizes can be observed. This is called Dark field.

All the TEM and STEM experiments in this thesis are performed by M. Bahri, G. Patriarche, L. Largeau at the Laboratoire de Photonique et Nanostructures (LPN) in Marcoussis, France or Eric Gautron at IMN, in Nante, France.

## References

[1] K. Yamane, T. Kobayashi, Y. Furukawa, H. Okada, H. Yonezu, and A. Wakahara, “Growth of pit-free GaP on Si by suppression of a surface reaction at an initial growth stage,” *J. Cryst. Growth*, vol. 311, no. 3, pp. 794–797, 2009.

[2] K. Yamane, T. Kawai, Y. Furukawa, H. Okada, and A. Wakahara, “Growth of low defect density GaP layers on Si substrates within the critical thickness by optimized shutter sequence and post-growth annealing,” *J. Cryst. Growth*, vol. 312, no. 15, pp. 2179–2184, 2010.

[3] K. Yamane et al., “Growth of a lattice-matched GaAsPN p–i–n junction on a Si substrate for monolithic III–V/Si tandem solar cells,” *Appl. Phys. Express.*, vol. 10, no. 7, p. 075504, 2017.

[4] X. Yu, P. S. Kuo, K. Ma, O. Levi, M. M. Fejer, and J. S. Harris, “Single-phase growth studies of GaP on Si by solid-source molecular beam epitaxy,” *J. Vac. Sci. Technol.*, vol. 22, no. 3, p. 1450, 2004.

[5] A. C. Lin, M. M. Fejer, and J. S. Harris, “Antiphase domain annihilation during growth of GaP on Si by molecular beam epitaxy,” *J. Cryst. Growth.*, vol. 363, pp. 258–263, 2013.

[6] A. C. Lin et al., “Epitaxial growth of GaP/AlGaP mirrors on Si for low thermal noise optical coatings,” *Opt. Mater. Express.*, vol. 5, no. 8, p. 1890, 2015.

[7] I. Németh, B. Kunert, W. Stolz, and K. Volz, “Heteroepitaxy of GaP on Si: Correlation of morphology, anti-phase-domain structure and MOVPE growth conditions,” *J. Cryst. Growth.*, vol. 310, no. 7–9, pp. 1595–1601, Apr. 2008.

[8] H. Kroemer, “Polar-on-nonpolar epitaxy,” *J. Cryst. Growth.*, vol. 81, no. 1–4, pp. 193–204, 1987.

[9] B. Kunert, I. Németh, S. Reinhard, K. Volz, and W. Stolz, “Si (001) surface preparation for the antiphase domain free heteroepitaxial growth of GaP on Si substrate,” *Thin Solid Films*, vol. 517, no. 1, pp. 140–143, 2008.

[10] I. Németh, B. Kunert, W. Stolz, and K. Volz, “Heteroepitaxy of GaP on Si: Correlation of morphology, anti-phase-domain structure and MOVPE growth conditions,” *J. Cryst. Growth.*, vol. 310, no. 7–9, pp. 1595–1601, 2008.

[11] I. Lucci *et al.*, “Universal description of III-V/Si epitaxial growth processes,” *Phys. Rev. B*, vol. 2, no. 6, p. 060401, 2018.

[12] Y. Wang, “Structural analyses by advanced X-ray scattering on GaP layers epitaxially grown on silicon for integrated photonic applications,” Ph.D., INSA Rennes, Rennes, 2016.

[13] B. Heying *et al.*, “Role of threading dislocation structure on the x‐ray diffraction peak widths in epitaxial GaN films,” *Appl. Phys. Lett.*, vol. 68, no. 5, pp. 643–645, 1996.

[14] X. H. Zheng et al., “Determination of twist angle of in-plane mosaic spread of GaN films by high-resolution X-ray diffraction,” *J. Cryst. Growth*, vol. 255, no. 1–2, pp. 63–67, 2003.

[15] A. Segmüller, J. Angilelo, and S. J. La Placa, "Automatic X-ray diffraction measurement of the lattice curvature of substrate wafers for the determination of linear strain patterns," *J. Appl. Phys.*, vol. 51, no. 12, pp. 6224 – 6230, 1980.

[16] H. Mughrabi and B. Obst, "Misorientations and geometrically necessary dislocations in deformed copper crystals: a microstructural analysis of X-ray rocking curves," *Zeitschrift für Metallkunde*, vol. 96, no. 7, pp. 688–697, 2005.

[17] S. Weissmann, "Method for the study of lattice inhomogeneities combining X - ray microscopy and diffraction analysis," *J. Appl. Phys.*, vol. 27, no. 4, pp. 389 – 395, 1956.

[18] M. Fatemi and R. E. Stahlbush, "X - ray rocking curve measurement of composition and strain in Si - Ge buffer layers grown on Si substrates," *Appl. Phys. Lett.*, vol. 58, no. 8, pp. 825 – 827, Feb. 1991.

[19] M. Tilli and A. Haapalinna, "Properties of Silicon," in *Handbook of Silicon Based MEMS Materials and Technologies*, Elsevier, 2015, pp. 3–17.

[20] P. Y. Wang *et al.*, "Quantitative evaluation of microtwins and antiphase defects in GaP/Si nanolayers for a III–V photonics platform on silicon using a laboratory X-ray diffraction setup," *J. Appl. Crystallogr.*, vol. 48, no. 3, pp. 702–710, 2015.

[21] P. Y. Wang *et al.*, "Abrupt GaP/Si hetero-interface using bistepped Si buffer," *Appl. Phys. Lett.*, vol. 107, no. 19, p. 191603, 2015.

[22] E. Weckert, "The potential of future light sources to explore the structure and function of matter," *IUCrJ*, vol. 2, no. 2, pp. 230–245, Mar. 2015.

[23] "Synchrotron sources accelerate," Nature Photonics, vol. 9, p. 281, 2015.

[24] A. A. Sokolov and I. M. Ternov, *Synchrotron radiation*. Moscow: Akademia Nauk SSSR, Moskovskoie Obshchestvo Ispytatelei prirody, 1966.

[25] H. Winick and S. Doniach, "An Overview of Synchrotron Radiation Research," in *Synchrotron Radiation Research*, H. Winick and S. Doniach, Eds. Boston, MA: Springer US, 1980, pp. 1–10.

[26] K. Codling, "Atomic and Molecular Physics Using Synchrotron Radiation – the Early Years," *J. Synchrotron. Rad.*, vol. 4, no. 6, pp. 316–333, Nov. 1997.

[27] H. Winick and S. Doniach, *Synchrotron Radiation Research*. Springer Science & Business Media, 2012.

[28] P. Willmott, *An Introduction to Synchrotron Radiation: Techniques and Applications*. John Wiley & Sons, 2019.

[29] T. U. Schülli and S. J. Leake, "X-ray nanobeam diffraction imaging of materials," *Curr. Opin. Solid State Mater. Sci.*, no. Scient. Rep. 2017, pp. 188–201, 2018.

[30] A. V. Baez, "A Study in Diffraction Microscopy with Special Reference to X-Rays," *J. Opt. Soc. Am.*, vol. 42, no. 10, p. 756, Oct. 1952.

[31] E. Spiller, "Low‐Loss Reflection Coatings Using Absorbing Materials," *Appl. Phys. Lett.*, vol. 20, no. 9, pp. 365–367, May 1972.

[32] P. Kirkpatrick and A. V. Baez, "Formation of Optical Images by X-Rays," *J. Opt. Soc. Am.*, vol. 38, no. 9, p. 766, Sep. 1948.

[33] M. Montel, "Réflexion et focalisation des rayons X par les miroirs," *Ann. Phys.*, vol. 13, no. 3, pp. 859–914, 1958.

[34] P. Kirkpatrick, "X-Ray Images by Refractive Focusing," *J. Opt. Soc. Am.*, vol. 39, no. 9, p. 796, Sep. 1949.

[35] S. Suehiro, H. Miyaji, and H. Hayashi, "Refractive lens for X-ray focus," *Nature*, vol. 352, no. 6334, pp. 385–386, Aug. 1991.

[36] B. X. Yang, "Fresnel and refractive lenses for X-rays," *Nucl. Instrum. Methods Phys. Res.*, vol. 328, no. 3, pp. 578–587, May 1993.

[37] A. Snigirev, V. Kohn, I. Snigireva, and B. Lengeler, "A compound refractive lens for focusing high-energy X-rays," *Nature*, vol. 384, no. 6604, pp. 49–51, Nov. 1996.

[38] V. V. Aristov *et al.*, "X-ray focusing by planar parabolic refractive lenses made of silicon," *Opt. Commun.*, vol. 177, no. 1–6, pp. 33–38, Apr. 2000.

[39] A. A. Snigirev *et al.*, "Focusing properties of x-ray polymer refractive lenses from SU-8 resist layer," presented at the Optical Science and Technology, SPIE's 48th Annual Meeting, San Diego, California, USA, 2003, p. 21.

[40] A. V. Baez, "Fresnel Zone Plate for Optical Image Formation Using Extreme Ultraviolet and Soft X Radiation," *J. Opt. Soc. Am.*, vol. 51, no. 4, p. 405, Apr. 1961.

[41] K. Saitoh, K. Inagawa, K. Kohra, C. Hayashi, A. Iida, and N. Kato, "Fabrication and Characterization of Multilayer Zone Plate for Hard X-Rays," *Jpn. J. Appl. Phys.*, vol. 27, no. 11A, p. L2131, Nov. 1988.

[42] W. Liu *et al.*, "Achromatic nested Kirkpatrick–Baez mirror optics for hard X-ray nanofocusing," *J. Synchrotron Rad.*, vol. 18, no. 4, pp. 575–579, Jul. 2011.

[43] R. P. Winarski *et al.*, “A hard X-ray nanoprobe beamline for nanoscale microscopy,” *J. Synchrotron Rad.*, vol. 19, no. 6, pp. 1056–1060, Nov. 2012.

[44] C. Riekel, M. Burghammer, and R. Davies, “Progress in micro- and nano-diffraction at the ESRF ID13 beamline,” *IOP Conf. Ser.: Mater. Sci. Eng.*, vol. 14, p. 012013, Nov. 2010.

[45] M. Suzuki *et al.*, “A hard X-ray nanospectroscopy station at SPring-8 BL39XU,” *J. Phys.: Conf. Ser.*, vol. 430, p. 012017, Apr. 2013.

[46] U. Johansson, U. Vogt, and A. Mikkelsen, “NanoMAX: a hard x-ray nanoprobe beamline at MAX IV,” in X-Ray Nanoimaging: Instruments and Methods, 2013, vol. 8851, p. 88510L.

[47] E. Nazaretski *et al*., “Design and performance of an X-ray scanning microscope at the Hard X-ray Nanoprobe beamline of NSLS-II,” *J. Synchrotron Rad.*, vol. 24, no. 6, pp. 1113–1119, Nov. 2017.

[48] G. A. Chahine *et al*., “Imaging of strain and lattice orientation by quick scanning X-ray microscopy combined with three-dimensional reciprocal space mapping,” *J. Appl. Crystallogr.*, vol. 47, no. 2, pp. 762–769, 2014.

[49] C. Liewald *et al.*, “Microdiffraction imaging—a suitable tool to characterize organic electronic devices,” *AIMS Materials Science*, vol. 2, no. 4, pp. 369–378, 2015.

[50] V. Holý *et al*., “Observation of individual stacking faults in GaN microcrystals by x-ray nanodiffraction,” *Appl. Phys. Lett.*, vol. 110, no. 12, p. 121905, 2017.

[51] J. Wallentin, D. Jacobsson, M. Osterhoff, M. T. Borgström, and T. Salditt, “Bending and Twisting Lattice Tilt in Strained Core-Shell Nanowires Revealed by Nanofocused X-ray Diffraction,” *Nano Lett.*, vol. 17, no. 7, pp. 4143–4150, 12 2017.

[52] M. Meduňa *et al.*, “Lattice tilt and strain mapped by X-ray scanning nanodiffraction in compositionally graded SiGe/Si microcrystals,” *J. Appl. Crystallogr*., vol. 51, no. 2, pp. 368–385, Apr. 2018.

[53] S. J. Leake *et al.*, “The Nanodiffraction beamline ID01/ESRF: a microscope for imaging strain and structure,” *J. Synchrotron Rad.*, vol. 26, no. 2, pp. 571–584, 2019.

# Chapitre 3. Sub-micrometer-beam X-ray diffraction on GaP/Si pseudo-substrate for local dislocation distributions

This chapter introduces our work on the sub-micrometer-beam X-ray scattering for local structure characterization of the GaP/Si pseudo-substrate. Firstly, a brief overview is given on the previous structural optimization studies on MT and APD with laboratory set-up and synchrotron X-ray source. Secondly, the sub-micrometer-beam X-ray diffraction experiment setup and the data process methods are proposed to obtain the local relative tilt, strain, and FWHM of line profile. These local scan mappings are then studied with the STEM and the AFM results, to understand the relationship between 60° dislocation, local strain lines, and the surface morphology. Thirdly, a further observation of the origin of the line profile broadening is discussed. Finally, the experiment results are summarized and the potential application of these results on the structural optimization is stated. Some work in the chapter is reproduced by a paper titled "*A study of the strain distribution by scanning X-ray diffraction on GaP/Si for III-V monolithic integration on silicon*", *J. Appl. Crystallogr.*, vol. 52, no. 4, pp. 809–815, Aug. 2019. [1]

## 3.1. Previous structural optimization on GaP/Si pseudo-substrate

The more recent previous works on GaP/Si pseudo-substrate structural optimization has been carried on in FOTON-OHM by Tra Thanh Nguyen [1], Yanping Wang [2] during their thesis. The last work was performed by Yanping Wang mainly on the quantitative measurements on two main defects: microtwins (MT) and antiphase domains (APD) (separated by antiphase boundaries-APB) and the optimization of the growth condition to eliminate them. Thus, sub-micrometer-beam X-ray diffraction can be performed and analyzed on the samples to thoroughly study the structural defects in our GaP/Si pseudo-substrates.

### 3.1.1. Micro-twin quantification and corresponding growth condition optimization

Figure 3-1 is a pole figure image around the nominal GaP (111) reflection for a 140nm GaP/Si (001) 6° -off sample towards the [110] direction. This image is drawn with ϕ and χ polar coordinates, where ϕ is the polar angle and χ is the radius. The inner four reflections are contributed by the MTs in GaP epitaxy layer and the outer signals are mainly from Si as its far higher effective scattering volume compared to GaP. The definition of the MT-A to MT-D is the same as the statement in section 1.4.2. The intensity of the reflections from the MTs is extracted from the image and corrected by removing the background noise. Then the intensity is normalized taking into account the intensity of the incident beam $I_0$ and other measurement corrections, for instance Lorentz and polarization corrections. A more detailed description of the method is shown in A1.

With this method, the epitaxy condition is optimized towards the elimination of the MT. The experiment results showed that the samples grown at a temperature above 500 ℃ have much fewer MTs compared to those grown at a temperature under 500 ℃. Then, the migration enhanced epitaxy (MEE) technique which consists of alternated growth of Ga and P atomic layer in order to favor 2D growth mode has been applied. Finally, a two-step growth procedure which consists growing a first 10 nm-thin MEE followed by MBE growth of GaP has also been proven to eliminate the MT volume fraction. [5]–[8]

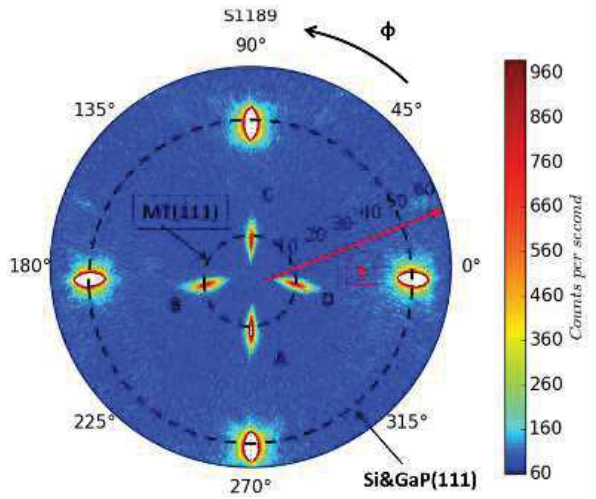


Figure 3-1 Poles figure image around the nominal GaP (111) reflection for the S1477 140nm GaP/Si (001) 6° -off sample towards the [110] direction.

Finally, the volume fraction of MTs can be decreased to below about 0.5%, which is the limit of the sensitivity of the method for GaP layer with a thickness equal to about 100nm, and the r.m.s roughness can reach 0.97 nm for the sample grown with the optimized condition, which is shown as Figure 3-2.

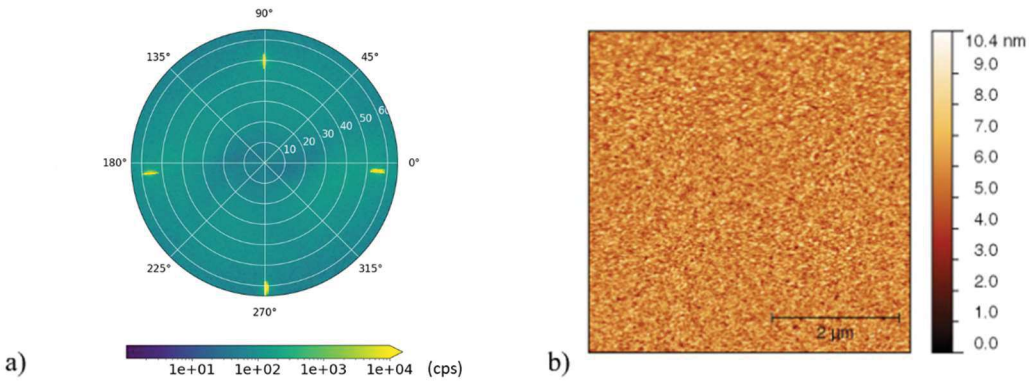


Figure 3-2 The a) Poles figure b) 5×5 µm2 AFM images of a GaP/Si sample grown with the optimized condition.

### 3.1.2. Anti-phase Domain quantification and corresponding growth condition optimization

The quantification of the Anti-Phase Domain (APD) is calculated by the Williamson-Hall-like plot with the results extracted from the RSMs performed with laboratory and synchrotron X-

ray setups [2]. Figure 3-4 (a) and (b) are two RSMs around GaP (002) and (004) reflection for a 45nm GaP/Si (001) sample, respectively.

The intensity around the GaP center scattering spot is intercepted and integrated along $S_x$ to get the corresponding transverse scans, which is shown as Figure 3-4 (c) and (d). Which need to be mentioned is that, the RSM around GaP (002) or (006) are more sensitive to the APDs compared to that around GaP (004). The profile of the transverse scans is fitted with two-component pseudo-Voigt functions, to get the peak position and the Integral Breadth (IB). The narrow and intense component has been attributed to long-range structural correlations, due to the fact that plane displacements are bounded in magnitude by the substrate, which acts as a source of structural coherence (due to the epitaxy) over a relatively large lateral correlation length. The broad diffuse-scattering peak has been attributed to diffuse-scattering for shorter-range correlation lengths and is, therefore, defect induced. [9], [10]

As for last, the peak position $S_x$ and the FWHM of the transverse scans of different Bragg reflections are plot into the same figure, and are fitted into a line with the equation below:

$$\left(\frac{\mathrm{IB(s)}}{\mathrm{S}}\right)^2 = \frac{1}{\xi_x}\frac{\mathrm{IB(s)}}{\mathrm{S}^2} + \Delta \mathrm{M}^2 \tag{3-1}$$

where ***IB(s)*** is equal to the IB, $\mathrm{S} = S_z$, $\boldsymbol{\xi_x}$ is the lateral correlation length of the defects and $\boldsymbol{\Delta M}$ is related to the micro-mosaicity. If the density of other defects except APDs is low, the lateral correlation length $\boldsymbol{\xi_x}$ can be related to an APD correlation length. Furtherly, if the density of APBs is also low, the lateral correlation length $\boldsymbol{\xi_x}$ can correspond to minority APD domains. [2],[3] If polarity (the ratio between main phase and antiphase) is near zero, then the correlation length should correspond to an apparent mean distance between APB, which is what is observed by Yanping Wang when she compares TEM and XRD analysis (see in [7]). As the APDs' contribution on the line profile broadening are different between different Bragg reflection, we can quantitatively analyze the APDs' influence on the line profile broadening by comparing the value of $\boldsymbol{\xi_x}$ with a method called "Williamson-Hall-like" (WHL) plot (the detail of the method is discussed in [3]). An example of the method is shown in Figure 3-3

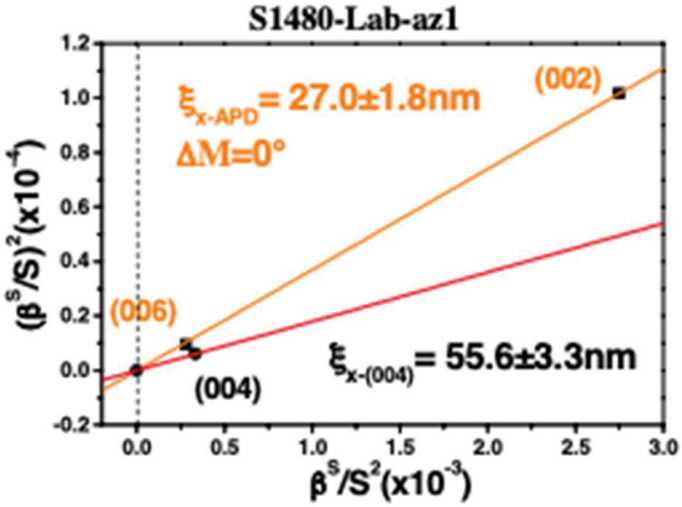


Figure 3-3 Example of Williamson-Hall-like Plot.

With this method, Yanping Wang has demonstrated that the Si surface preparation and Ga coverage at the initial growth stage are the key points in the elimination of the APDs.

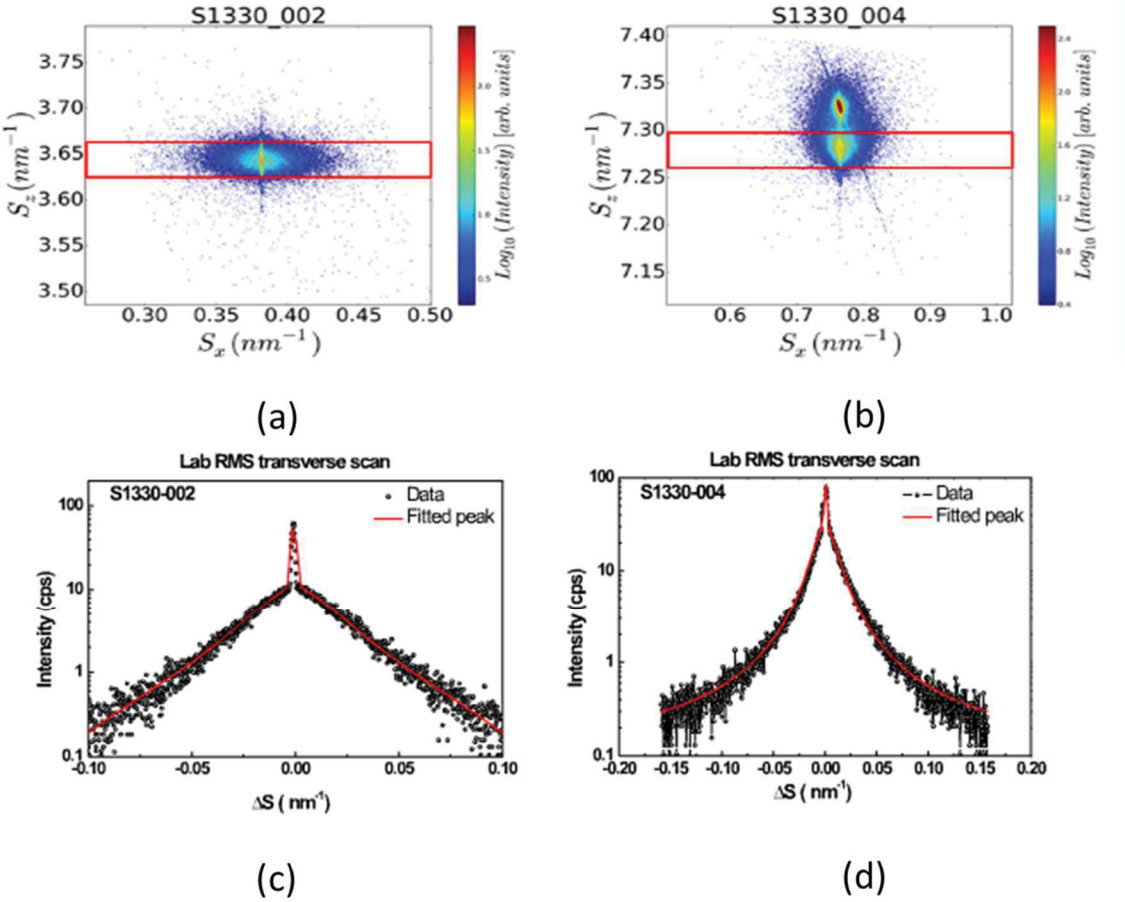


Figure 3-4 Laboratory XRD RSM around (a) 002 and (b) 004 nearly specular reflections for S1330, and their corresponding transverse scans (c) and (d).

Finally, besides the growth optimization described previously, which consists of the 10 nm-thin MEE layer growth followed by the conventional MBE-growth GaP layer, this last GaP layer has been grown including four successive 50-nm-thick GaP layers separated by three AlGaP 2-nm-thin layers [3]. Most APDs are shown to be annihilated within the first 10 nm, and a larger-field observation showed a progressive annihilation through the layers with a final density of about 3 APBs per micrometer at the top (Figure 3-5).

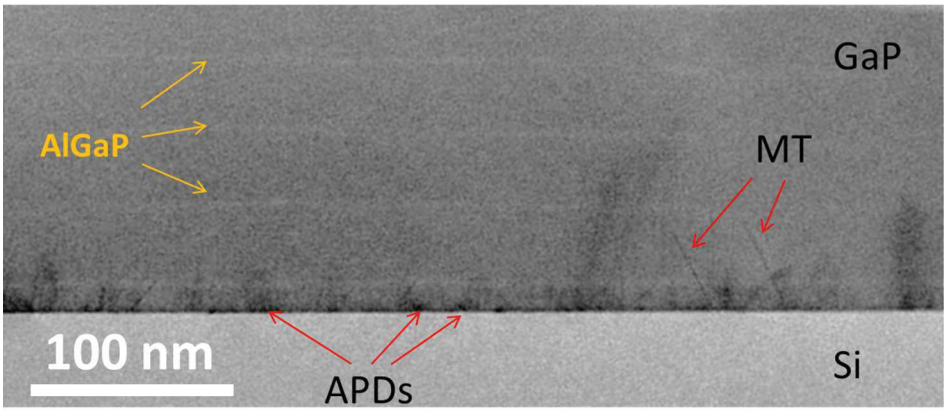


Figure 3-5 Cross-section STEM-BF images for the optimized GaP/Si growth (from ref [7] ).

## 3.2. Characterization of a 200 nm GaP/Si sample

### 3.2.1. Sample growth and lab setup characterization

The sample (S1477) used in this study is a 200 nm-thick GaP layer epitaxially grown using a RIBER solid-source Molecular beam epitaxy (MBE) reactor, on a Si substrate with a 6° -off towards the [-1-10] direction. The MBE GaP layer growth used the two-step procedures introduced in the former chapter: first a 10 nm-thin GaP layer was grown by the migration enhanced epitaxy (MEE) technique, and then a conventional MBE-grown GaP layer which includes four successive 50-nm-thick GaP layers separated by three AlGaP 2-nm-thin layers [7], [11].

The basic structural properties of the sample S1477 are firstly investigated by using the laboratory X-ray diffraction setup, which is detailed in Section 2.2. Based on the result of Reciprocal Space Mapping (RSM) shown as Figure 3-6 (a), a 50±2% plastic relaxation rate is measured. The Micro-Twins (MTs) defects volume fraction measured from the poles figure is lower than the detection limit of about 0.5%, shown in Figure 3-6 (b) [7]. The sample morphology was investigated by AFM (section 2.3.2) in tapping mode. The 5 µm × 5 µm AFM image's first scan axis (x) is parallel to [100] direction to avoid loss of roughness sensitivity along the [-1-10] and [1-10] directions shown in Figure 3-6 (c) and the measured root means square (r.m.s.) roughness is 2.14nm. Dark-Field (DF) TEM measurements was done using a probe corrected Jeol 2200Fs microscope. The diffracted beam chosen for DF imaging are (220) and (400), and the (220) DF graph is shown as Figure 3-6 (d).

### 3.2.2. Performance of K-Map

Before the appearance of the K-Map technique, many researchers have tried to develop X-ray mapping techniques for the local structural information. For instance, P. M. Mooney et al. have applied the X-ray microdiffraction to check the structural quality of SiGe thin layers grown on Si substrates [12]. J. Matsui also performed a series of rocking curve scans on a Silicon on Insulator (SOI) sample to measure the spatial distribution of the lattice strains [13]. Spatial resolution has been considerably enhanced by the recent development of the third-generation synchrotron long beamlines and more performant X-ray optical focusing systems. For faster acquisition, K-Map includes a hardware system that synchronizes the piezo scanner holding the sample, and the detector. The resolution of the K-Map is limited by the size of the beam, times the projection effect and the thickness effect of the projection of the beam in the sample. But the K-Map avoids also sample preparation and is nondestructive. Mondiali et al. have applied the K-Map to investigate SiGe on a patterned wafer [14], and Zoellner et al. used the same method on a 1.6µm-thick SiGe sample on a normal Si substrate. They reported the tilt and the strain distribution mapping result from the (004) and (113) Bragg reflections [15]. B. Vianne et al. have aslo investigated thermo-mechanical strain, induced by a Through Silicon Via (TSV) process in silicon, using K-map measurements combined with finite element modelling [16].

The K-Map is performed using the beamline ID01 at ESRF [17], [18]. The 8 keV X-ray beam was focused by a Fresnel zone plate (FZP) with a beam stop (BS) and an order sorting aperture (OSA) to the center of rotation of the goniometer. The beam cross section is around 300 nm (horizontal) × 100 nm (vertical) at the goniometer center, which is shown in Figure 3-7 (a).

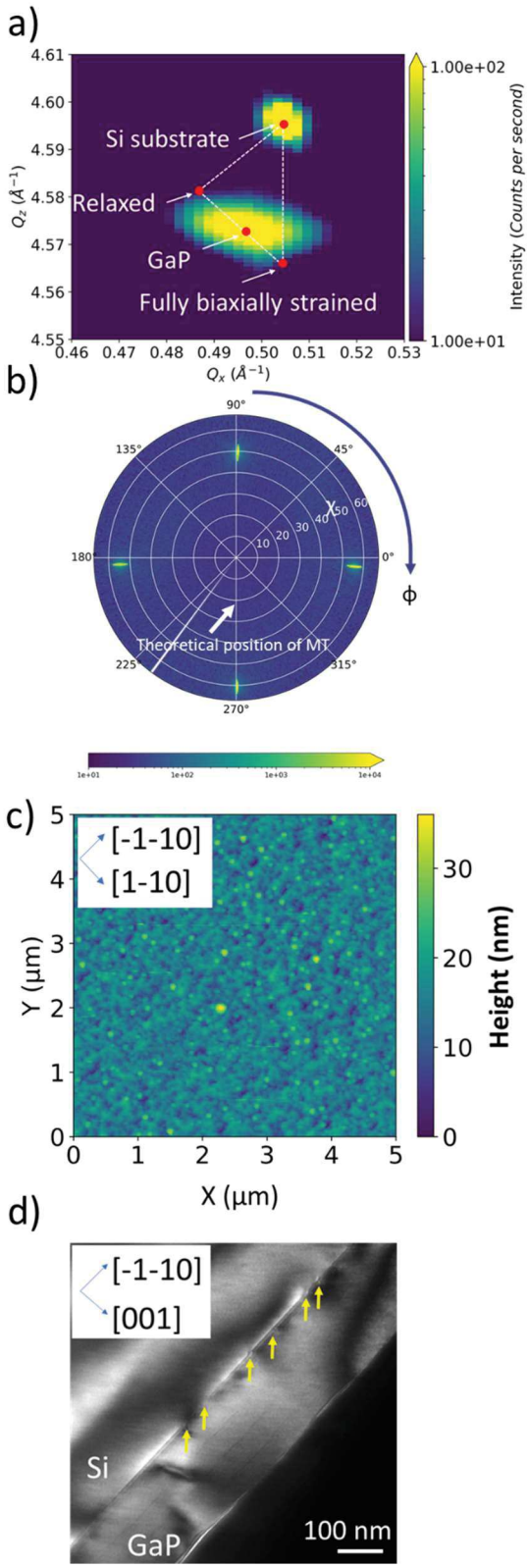


Figure 3-6 (a)RSM image of (004) diffraction. (b) PF image (c) 5µm×5µm AFM image under tapping mode. (d) Cross-sectional (220) Dark-Field (DF) TEM image. The misfit dislocations are labelled with yellow arrows.

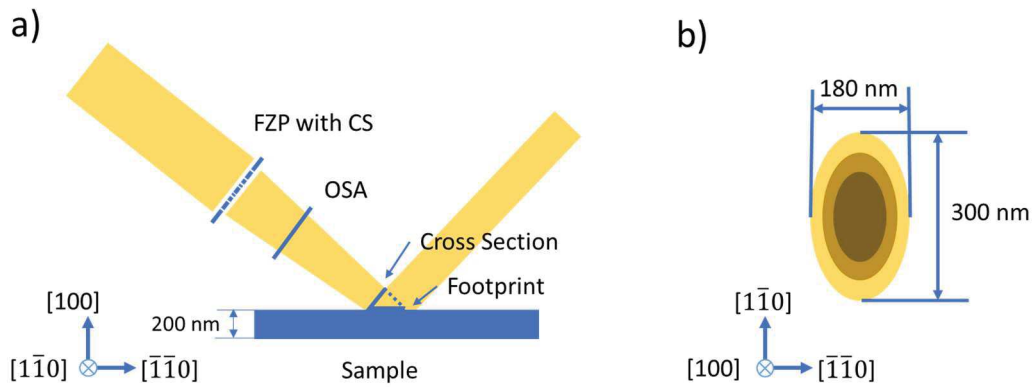


Figure 3-7 a) The experimental setup of the K-Map and b) the footprint of the X-ray beam for the (004).

The effective spatial resolution depends on incidence angle and sample thickness, which is shown as Figure 3-8, and can be calculated with the equation below:

$$L = \frac{d}{sin\,\omega} + \frac{z}{tan\,\omega} \tag{3-2}$$

where L is the corrected vertical resolution, d is the vertical X-ray beam cross-section, z is the thickness of the sample, and ω is the incident angle.

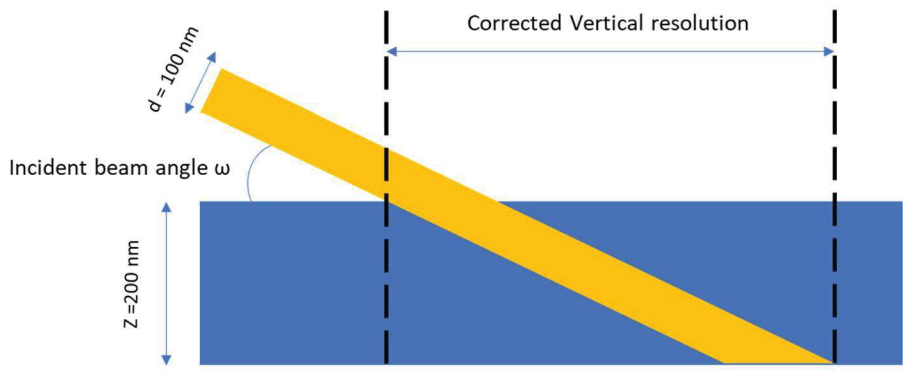


Figure 3-8 Sketch of the corrected vertical resolution in a thin layer, broadened by the projection of the cross-section and the sample thickness.

The footprint of the X-ray beam on the sample surface is 300 nm (horizontal) × 180 nm (vertical) for the (004) (shown as Figure 3-7 (b)) and 300 nm (horizontal) × 350 nm (vertical) for the (002). Due to the geometrical projection of the sample surface, the vertical beam cross-section broadens up to about 400nm for (004) and 800nm for (002) Bragg reflections, by projection

effect on the sample surface and depth, but variations can be observed under this resolution limit. The reason is that the intensity function of the X-ray spot is not a box with sharp boundaries, and most of the intensity is in the centre of the spot. According to actually experimental condition, the spatial resolution is presumed to be around 100~200 nm for both [1-10] and [-1-10]. In addition, the movement of the sample is controlled by the nanomotor and the step is 100 nm, which is shown in Figure 3-90. As the scattering spot only partially overlap with each other, the intensity of the scattering spot will show the difference between the neighbour positions.

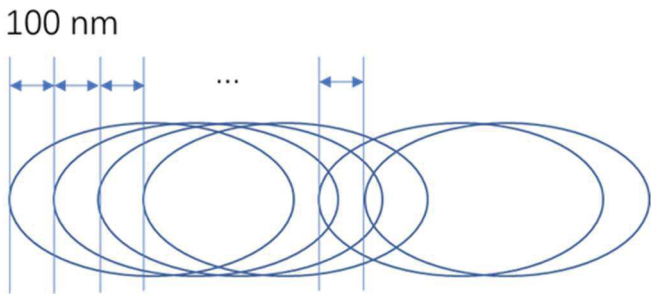


Figure 3-9 The movement of the X-ray spot on the sample surface controlled by the nanomotor.

For each studied Bragg reflection, a complete acquisition consists of a 5D scan (2D at sample surface and 3D in reciprocal space) as follows: the incident rocking angle is fixed at different positions around the GaP nominal one, and the 2D Maxipix™ detector (square of 4 chips, 516 × 516 pixels with 55 µm pitch) is centered around the scattered beam position. An x-y piezo scan is then performed, with 100nm x 100nm steps, covering a sample surface of 10×6 $\mu m^2$.

### 3.2.3. Data processing

The 5D dataset is analyzed using a Python program named X-ray Strain Orientation Calculation Software (XSOCS), developed at ESRF [19]. XSOCS can extract a region of interest (ROI) from the 3D RSM, which nearly eliminates the Si substrate peak contribution and therefore facilitates the GaP layer analysis. A miscut of 5.93°±0.02° towards the [-1-10] direction is measured for the Si substrate. qx and qz axes of reciprocal space are set respectively parallel to [-1-10] and [001] directions of the Si substrate. Very rich information can be extracted from the reciprocal space analysis, for each point of the 2D space, such as lattice parameter, tilt, etc.[20]–[22] To this end, the local components qx, qy and qz of the diffraction vectors are

calculated for each point of the 5D dataset. To analyze the full 3D RSM dataset for each direct-space point, it is convenient to project these data in the (qx, qz) and (qy, qz) planes. To increase the signal to noise ratio, the summed 2D datasets are furtherly summed up to 1D curves, whose main dimensions are aligned with either the qx, or the qy axes. These 1D curves are then fitted by a Gaussian function to determine the key parameters of the peak at each direct space position, i.e. the reciprocal space peak maximum position, the Full Width at Half Maximum (FWHM) and integrated intensity.

Since the $q_x$ and $q_y$ are parallel to the [-1-10] and [1-10] mean crystallographic directions respectively, the local tilts towards [-1-10] and [1-10] can be directly calculated by the shift of $q_x$ and $q_y$ peak positions respectively:

$$\alpha_{[-1-10]} = sin^{-1}\left(\frac{q_x}{q}\right) \tag{3-3}$$

$$\alpha_{[1-10]} = sin^{-1}(\frac{q_y}{q}) \tag{3-4}$$

In addition, the total tilt angle, which is the angle between the local normal vectors and the Si substrate [004] direction, is as follow:

$$\alpha = cos^{-1}(\frac{q_z}{q}) \tag{3-5}$$

Being $q_z$ the scattering vector component aligned with the GaP (004) signal, that is corrected from the miscut.

The local lattice constant $a$ can be extracted with the following equation:

$$a = \frac{2\pi}{q} * \sqrt{h^2 + k^2 + l^2} \tag{3-6}$$

where (h, k, l) is the corresponding Miller indices of the reflection.

As the reciprocal lattice point studied is the (004) Bragg reflection for our experiment in general, the equation above can be written as:

$$a_{\perp} = \frac{8\pi}{q} \tag{3-7}$$

In addition, because of the defects or the strain, the local normal scatter vector may rock around the theoretical position. This variation let that $q_x$ and $q_y$ have small value instead of 0, and the Equation (3-7) can be written as:

$$a_{\perp} = \frac{8\pi}{\sqrt{q_x^2 + q_y^2 + q_z^2}} \tag{3-8}$$

And the out-of-plane lattice constant $a_{\perp}$ provides the local in-plane strain compared to the bulk GaP based on the following equation [23]:

$$\varepsilon_{\parallel} = \frac{a_{\parallel} - a_{GaP}}{a_{GaP}} = -\frac{C_{11}}{2C_{12}} \times \frac{a_{\perp} - a_{GaP}}{a_{GaP}} \tag{3-9}$$

where $\boldsymbol{\varepsilon}_{\parallel}$ is the in-plane strain compared to the bulk GaP, $C_{11}$=140.5 GPa and $C_{12}$=62 GPa are the elastic stiffness constants of GaP [24], $a_{GaP} = 5.4505\text{Å}$ is the bulk lattice constant of GaP [25], and the $\boldsymbol{a}_{\parallel}$ is the mean local in-plane lattice constant of all the lattice vectors in (001) plane.

### 3.2.4. The measurement resolution

According to the measurement, the angular resolution provided by the 2D pixel scanner is 0.0036 °/pixel. Thus, the resolution of the tilt along $Q_x$ or $Q_y$ is 0.0036°.

The resolution of the strain is complex. The strain is calculated from the distance of the Q in the reciprocal space, while the parameters to determine the resolution of $Q_x$, $Q_y$ and $Q_z$ are different. As the $Q_z$ contributes most to the norm of Q, we can approximately assume that the resolution of strain is determined with the same parameters with $Q_z$.

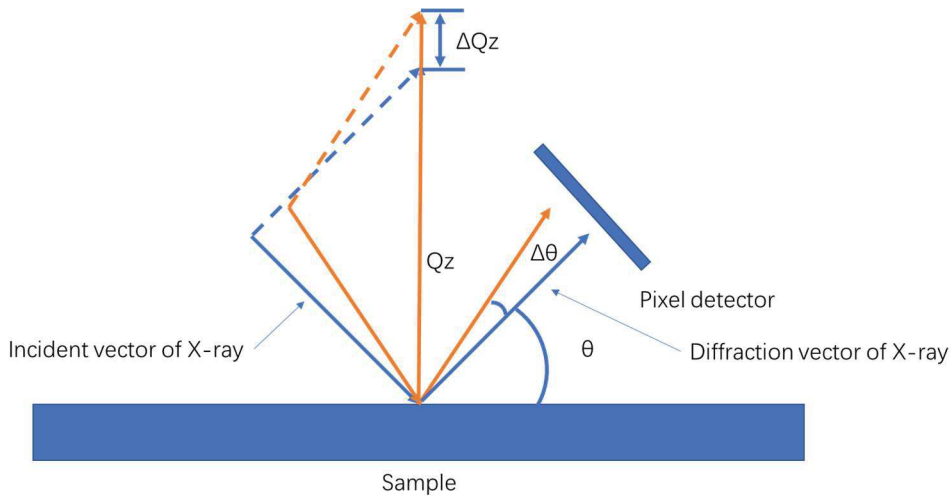


Figure 3-10 The resolution of Qz determined by the rotation of the diffraction vector.

In this work, the resolution of $Q_z$ is mainly determined by the rotation of $\frac{2\theta}{2}$, which is shown in Figure 3-10. Then, according to Bragg's law, we have these equations for (004) diffraction:

$$2dsin\left(\frac{2\theta}{2}\right) = n\lambda \tag{3-10}$$

$$\mathrm{d} = \frac{\mathrm{a}}{4} \tag{3-11}$$

where λ is the wavelength of the X-ray (8keV), $\frac{2\theta}{2}$ is the Bragg angle of our sample (34.5°) and $\Delta\frac{2\theta}{2}$ is equal to the angular resolution provided by the 2D pixel scanner (1°/278), a is the out-of-plane lattice constant of the measured material (GaP).

$$\Delta a = -2n\lambda\frac{cos\left(\frac{2\theta}{2}\right)}{\sin^2\left(\frac{2\theta}{2}\right)}\Delta\frac{2\theta}{2} \tag{3-12}$$

The resolution of the lattice constant of GaP, Δa is equal to $5\times10^{-5}$ nm.

As the in-plane strain $\boldsymbol{\varepsilon}_{\parallel}$ is as below:

$$\varepsilon_{\parallel} = \frac{\mathrm{a}_{\parallel} - \mathrm{a}_{\mathrm{GaP}}}{\mathrm{a}_{\mathrm{GaP}}} = -\frac{\mathrm{C}_{11}}{2\mathrm{C}_{12}}\frac{\mathrm{a}_{\perp} - \mathrm{a}_{\mathrm{GaP}}}{\mathrm{a}_{\mathrm{GaP}}} \tag{3-13}$$

We have:

$$\Delta\varepsilon_{\parallel} = -\frac{C_{11}}{2C_{12}}\frac{\Delta a}{a_{GaP}} \tag{3-14}$$

where $\boldsymbol{\varepsilon}_{\parallel}$ is the in-plane strain with respect to the bulk GaP, $\boldsymbol{C_{11}} = 140.5\ \mathrm{GPa}$ and $\boldsymbol{C_{12}} = 62\ \mathrm{GPa}$ are the elastic stiffness constants of GaP, $a_{GaP} = 0.54505$ nm is the bulk lattice constant of GaP. So, the resolution of the in-plain strain is approximately equal to 0.01%.

While the resolutions calculated above can be worse in real for some reasons. For instance, in the discussion above, we assume that the diffraction beam can be distinguished between the neighborhood pixels on the 2D pixel scanner. But the real diffraction signal may have a width cover more than one pixel of the scanner.

But according to our experience, the information in the tilt and strain mapping is still in within the allowable range of the resolution.

## 3.3. The local structural characterization with sub-micrometer-beam X-ray diffraction

Two mapping of the tilt towards [-1-10] and [1-10] directions are shown as Figure 3-11 (a) and (b) respectively. They exhibit lines, of high tilt values, that are respectively nearly parallel to the [-1-10] and [1-10] directions. To confirm the existence of these regions with high tilt values, a K-Map is also performed on the (002) reflection of the sample. The result is shown Figure 3-11 (c) for tilt towards [1-10]. When comparing Figure 3-11 (b & c), very similar patterns are identified with a slight shift that can be due to both imperfect alignment and drift of the x-y piezo stage with the large incidence angle shift.

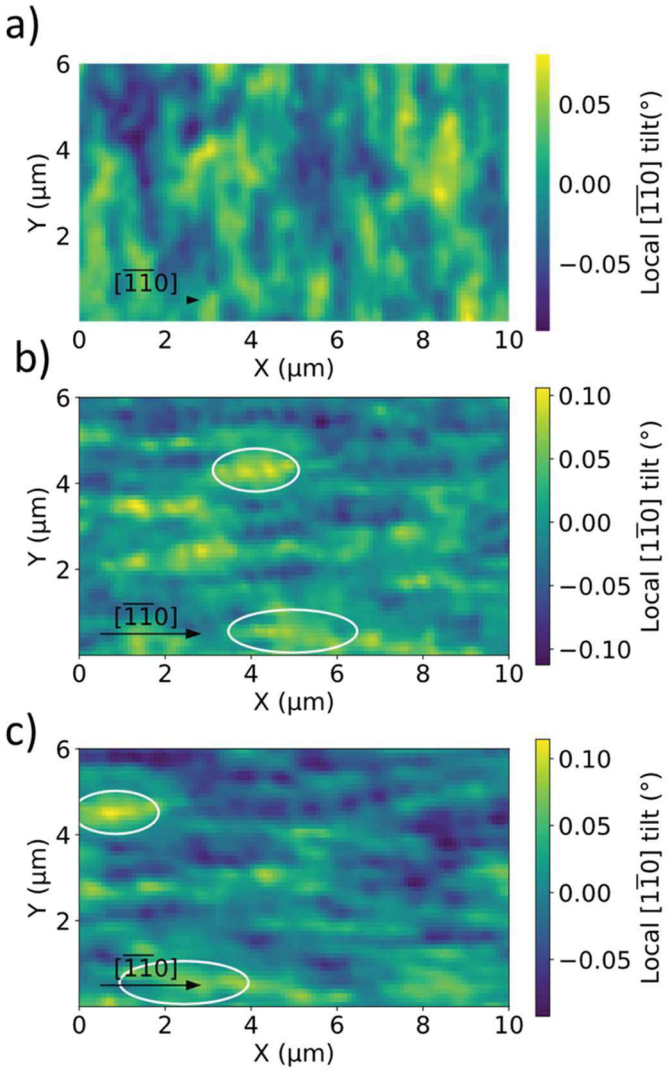


Figure 3-11 Tilt mapping towards (a) the [-1-10] and (b) the [1-10] using the (004) Bragg reflection. (c) Tilt mapping towards the [1-10] direction for the (002) Bragg reflection which exhibits similar tilts with (b) (the shift along the X direction is due to imperfect alignment or drift between measurements).

The local strain mapping is shown in Figure 3-12 (a). The mean local in-plane strain is -0.172%, which is equal to 48.2% relaxation, close to the 50±2% value measured from the laboratory setup RSM, probing a much larger area of the sample. Moreover, the mapping reveals lines with high strain value (yellow and green) which are nearly parallel to [1-10]. For the perpendicular direction ([-1-10]), that is the direction perpendicular to the statistically dominant steps on the Si substrate surface, the lines are less obvious and are less parallel to each other. According to literature, similar pattern has been observed along the misfit dislocations lines occurring at the GaP/Si (6° miscut toward [011]) as shown by electron

channeling contrast imaging (ECCI) [26]. The anisotropy of the distribution of strain is most likely influenced by the terraces on the Si surface with 6° miscut, which typical length is between 1.29 nm for atomic steps and 2.584 nm for bi-atomic steps. This ensemble forms a cross-hatch like a pattern that suggests the presence of linear or planar relaxing defects more or less aligned along [110] type crystallographic directions. This assumption is strengthened by cross-section TEM imaging performed on the same sample for <1 -1 0> zone axis (see Figure 3-6(d)) that reveals the presence of dislocation lines parallel to [1 -1 0]. The linear density of the dislocations along [-1-10] measured by TEM is 10 $\mu m^{-1}$ (see in Figure 3-6 (d)). Most of these dislocations are observed to be 60° type (which is introduced in section 1.4.1) and the 10 $\mu m^{-1}$ linear density corresponds (if considering the same density along the other direction) to a plastic strain relaxation rate of about 45%, i. e. of the same order that the values determined both from X-ray laboratory and synchrotron sub microbeam measurements. This suggests that 60° dislocations correspond to the main relaxation processes in our system, in agreement with other literature results [27]. From these observations, we can assume that the observed broadening of the scattering line profile is mainly due to a local increase of the dislocation density [28], [29].

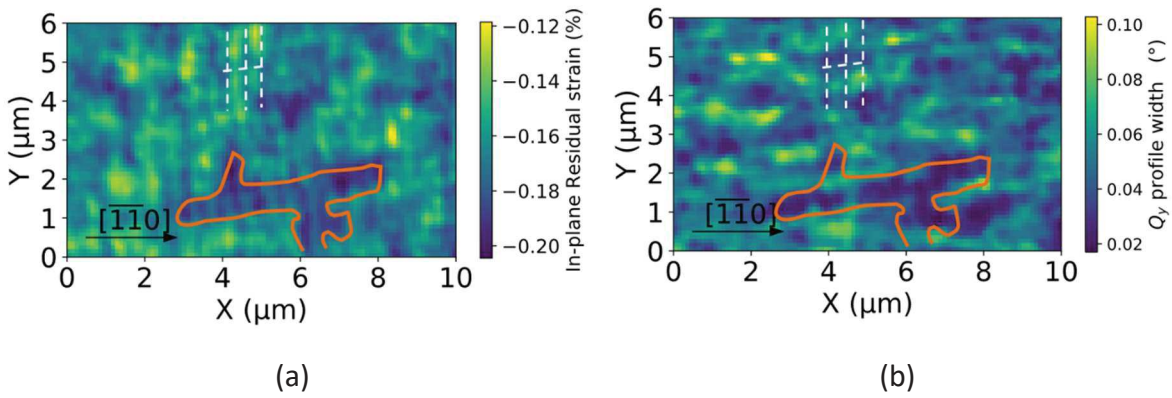


Figure 3-12 (a)Local strain (%) (b) FWHM of the $Q_y$ profile (°) mapping on (004) Bragg reflection of Sample S1477, which is 200nm GaP on Si substrate with 6° -off towards the [-1-10] direction.

To study the distribution of the strain, the in-plain strain mapping Figure 3 (a) is filtered with a local binary patterns(LBP) function and the cross-hatch like network is extracted in Figure 3-14 (a) [30], [31]. Different from the normal binary filter, LBP does not have a fixed threshold. Instead of that, the threshold in LBP is given by the mean value of the neighborhood pixels

(except itself). Three LBPs with neighborhood ranges equal to 1, 2 and 3 are shown in Figure 3-13,respectively. The neighborhood range in our analysis is 3, which means the threshold is equal to the mean value is from the neighborhood 24 pixels. The chosen of the neighborhood range will slightly influence the quality of the threshold, while in the normal situation, the difference is really small. According to manual observations, 3 is the best one to extract the pattern of the lines with high strain, while has nearly no error.

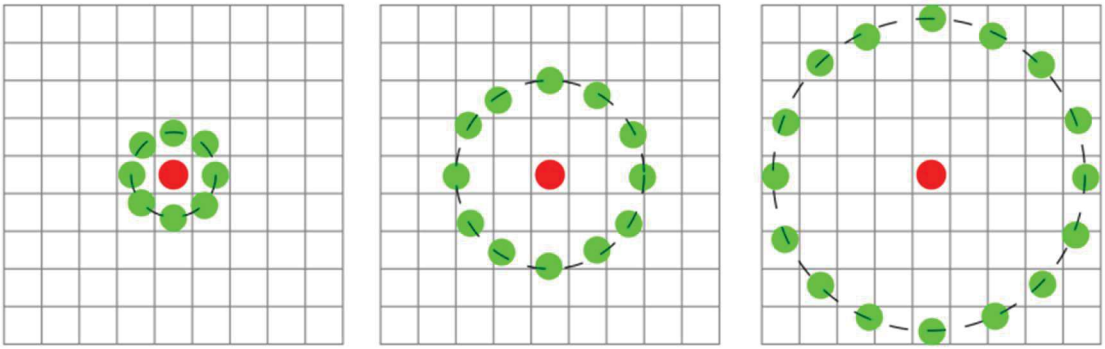

Figure 3-13 Three LBPs with neighborhood ranges equal to 1, 2 and 3.

Then the cross-hatch like network is transformed into frequency field by two-dimensional Fourier transform. The spatial frequency of the lines with high strain along [-1-10] is measured to be 1.91 µm-1 (Figure 3-14 (b) blue line), while the strain lines along the perpendicular direction ([-1-10]) has not obvious spatial frequency (Figure 3-14 (b) orange line).

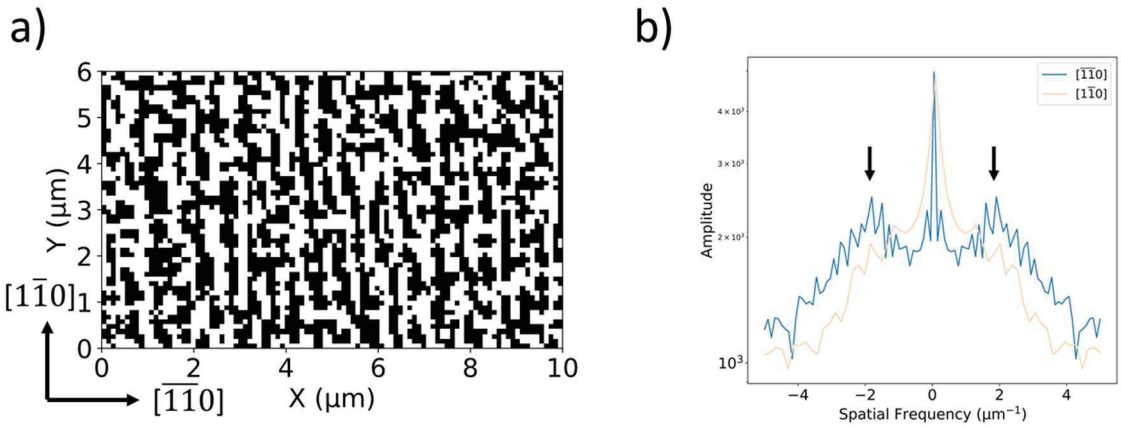


Figure 3-14 (a) Local binary image extracted from the residual strain mapping (Figure 3-12 a). (b) Spatial frequency of the lines with high strain along [-1-10] (blue) and [1-10] (orange).

Otherwise, the density of the dislocations along [-1-10] measured by TEM is 10 µm-1. As the 60° dislocations (which is introduced in section 1.4.1) are here the main relaxation process

[19], this indicates that the distribution of the dislocations is not homogeneous, and the 60° dislocations is likely to form bunches, which is also observed in the cross-section TEM dark field images. P. Kightley et al. have observed that in InGaAs layers grown on (001) GaAs substrates (2° off-cut towards [-1-10]), the 60° misfit dislocations do not lie exactly along the in-plane [-1-10] direction [32], which is shown in Figure 3-15. So, it is reasonable to suspect that 60° misfit dislocations along [-1-10] direction are less parallel to [-1-10] compared to those along [1-10] direction in our sample because the steps of Si substrate are along [-1-10]. As the 60° dislocations are the main contribution for the relaxation process in our sample, the less parallel 60° dislocations along [-1-10] also may introduce the less parallel strain lines, which coincides with the observation of the strain mapping. So, a possible explanation of the anisotropy of the distribution of strain can be the influence of the terraces.

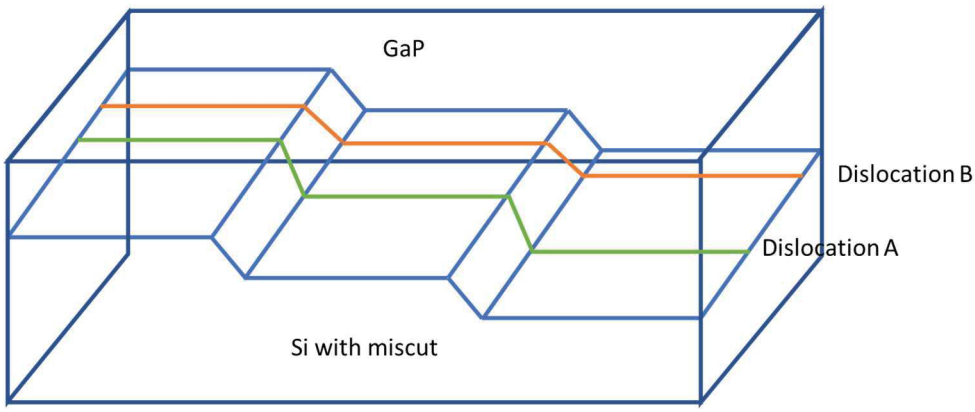


Figure 3-15 Sketch of the unparallel dislocations for the steps of the substrate (redrew based on figure 5(c) in ref [32]).

Finally, Dai and Chiang have reported that the roughening of free surfaces surface can be a result of the strain paths [33]. The cross-hatch surface morphology in partially or fully relaxed epitaxial films resulting from subsurface misfit dislocations was modelled by A.M. Andrews et.al [34]. We can notice that, in our experiment, the GaP epitaxial layer is thick, so the APDs' influence on the surface roughness is smaller as compared to other causes [28]. The cross-hatch surface morphology cannot be clearly observed in the AFM images. The spatial frequency of the lines with high in-plane strain, from the K-Map, and the surface roughness lines from AFM can be statistically compared. The AFM image Figure 3-6 (c) is also processed by the two-dimensional Fourier transform. The spatial frequency of along [-1-10] is 1.95 µm-1, which is shown as Figure 3-16 blue line, while the identification of the spatial frequency

along [1-10] is less obvious shown as Figure 3-16 orange line. Through this analysis, we can further assume that the strain line network introduced by the misfit dislocations may impact the surface morphology.

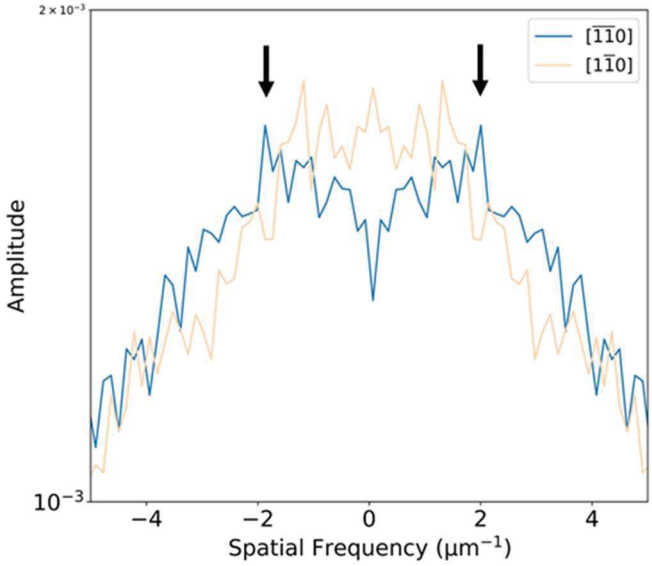


Figure 3-16 Spatial frequency of AFM image Figure 1(b) along [-1-10] (blue) and [1-10] (orange).

## 3.4. Other observation and discussion on the line profile of the scattering spot along Qy

In section 3.3, the FWHM mapping of $Q_y$ line profile has been shown. The difference of the local broadening can be a result of dislocations. To study this hypothesis, a further discussion will be given in this section for the line profile broadening of the scattering spot along $Q_y$.

In the former analysis of the FWHM of the $Q_y$ line profile mapping of sample S1477, the FWHM value is measured from the Gaussian function fitted to the $Q_y$ line profile. While, although the $Q_y$ line profiles have only one peak for most of the scanning points on the sample, we observe some special points have double peaks by the direct analysis of the 2D-CCD images.

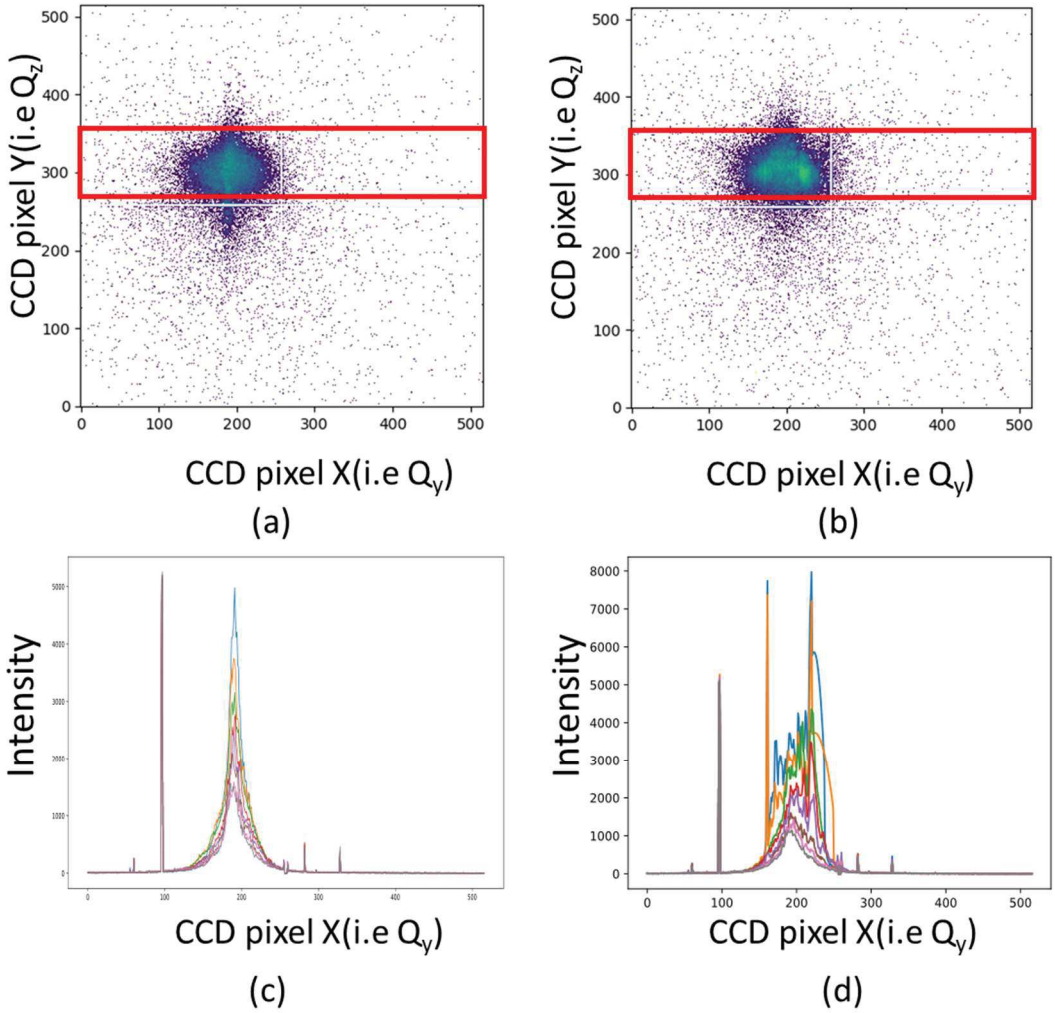


Figure 3-17 (a) The single-peak point CCD image with ω = 40.40° for (004) Bragg reflection and (c) the corresponding transverse scan with 0.01° width. (b) The double-peak point CCD image with ω = 40.40° for (004) Bragg reflection and (d) the corresponding transverse scan with 0.01° width.

Figure 3-17 (a) and (b) are respectively the direct CCD image for an single-peak point and a double-peak point from the sample S1477 (004) Bragg reflection with ω = 40.40°. And the intensity is integrated along CCD pixel Y (i.e. $Q_z$) direction for a width of 0.01° for different ω angle range from 40.38° to 40.52° with 0.02° step, which are the closest 8 angles to the normal (004) GaP Bragg reflection.

As the introduction in Chapter 2 on the RSM, the scattering point position of a crystal plane family (i.e. isometric crystal planes) in the RSM is only determined by the Bragg angle or the

tilt angle. Thus, we can define a model to identify the different modes of the diffraction image, which is shown as Figure 3-18.

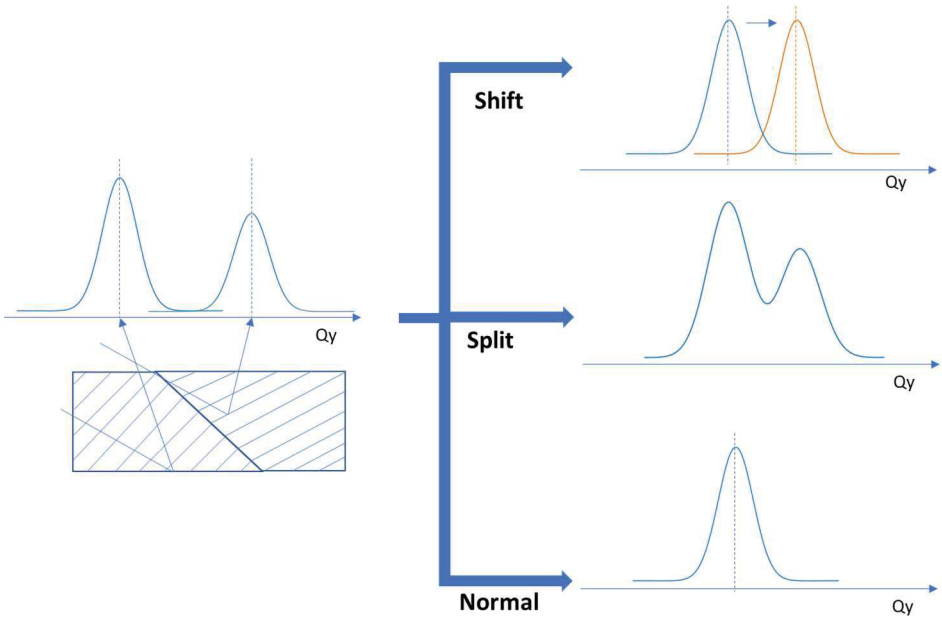


Figure 3-18 Sketch of different modes in the diffraction image.

As only the double-peak instead of the multi-peak condition is observed in the analysis, we assume that in each scanning point of the sample surface, only one or two coherent domains of diffraction (crystallites) are seen. So, for each scanning point, there are three possible modes: normal, shift and split (Figure 3-18). The normal mode means that there is only one crystallite and the tilt towards [1-10] is under the detection limit, which is set at 0.02°. The shift mode means that there is one crystallite with tilt value towards [1-10] larger than 0.02°. And the split mode means that there are two crystal plane families with different tilts or a large difference between the lattice constants.

The modes for each scanning point on the sample surface are identified and plotted as Figure 3-19 (a). The green, white and red colors are responding for the normal, shift and the split modes. And we overlap the peak mode identification results on the tilt mapping towards [1-10] of (004) Bragg reflection, which is shown in Figure 3-19 (b). The white lines surround the shift areas, and the red lines surround the split areas. In the tilt mapping, the local tilt angle is determined only by the shift of main peak. The results of Figure 3-19 (a) and (b) well coincides with each other. In addition, the red lines surround areas, i.e. the split areas, are observed to have large positive local tilt values, which have a mean value equal to 0.105°.

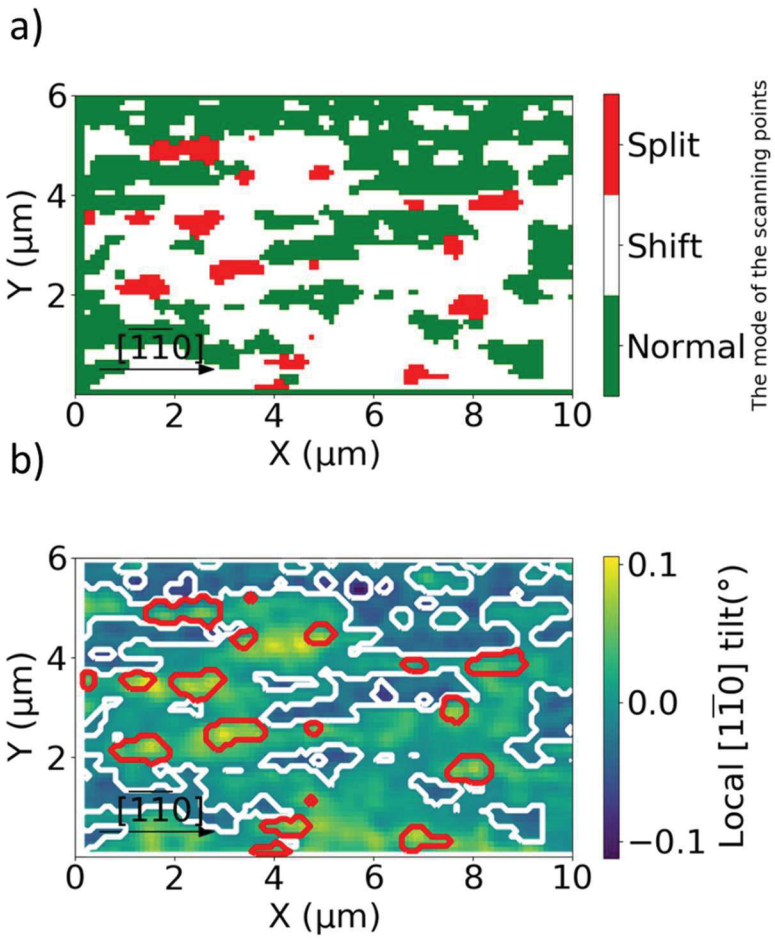


Figure 3-19 (a) The mode mapping for sample S1477. The red, white and green areas respond to "split", "shift" and "normal" modes respectively. (b) Tilt mapping towards $[1\bar{1}0]$ using the (004) Bragg reflection (i.e. Figure 3-11.b) and the overlapping contour lines base on (a), where the red lines labelled "split" areas and the white lines labelled "shift" areas.

The peak mode identification results are also overlapped on the FWHM mapping of main peak along Qy and in-plane residual strain mapping, as shown in Figure 3-20 (a) and (b), respectively. In Figure 3-20 (a), the split areas are observed to be well fitted with the high FWHM areas. In In Figure 3-20 (b), the split areas are not perfectly fitted with high strain areas, but the strain in the split areas are obviously larger than the mean value (-0.147% of the split areas compared to -0.172% for the whole mapping). As stated in the former section 3.3, the ***FWHM*** of scattering spot and the local strain are related to the density of the defects, which are mostly dislocations in this sample. So, we suspect that the splitting of the diffraction peak may be a result of the dislocations. A recent result on a 600nm-thick SiGe/Si sample also shown the strong relationship between the dislocations and the local tilt [36]. In addition, the local

strain is influenced by the density of dislocations along two directions $Q_y$ and $Q_x$, which is different from the ***FWHM*** along $Q_y$. This may explain why the split areas are better fitted with the pattern in the FWHM mapping than the in-plane residual strain mapping.

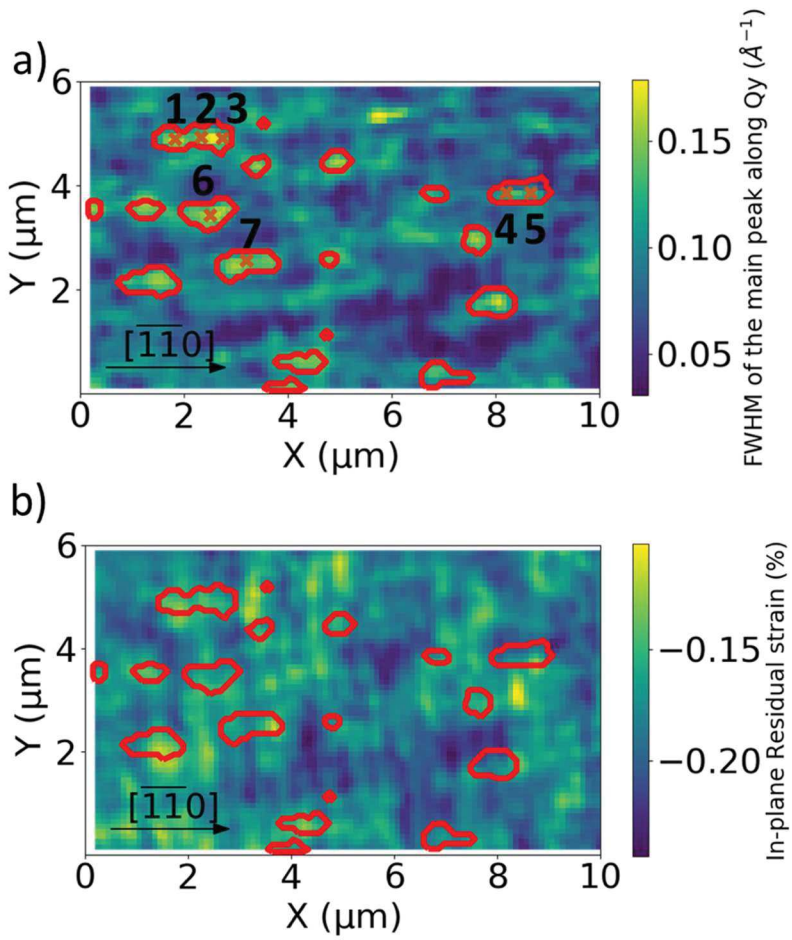


Figure 3-20 (a) FWHM mapping of the main peak along $Q_y$ and (b) In-plane residual strain mapping with overlapped contour lines (red) of the "split" areas based on Figure 3-19(a).

A further analysis is performed by sampling the split areas. Twenty different points in the split area are randomly chosen, and seven of these points are labeled in Figure 3-20(a). The CCDs images of these points are extracted for different ω angle range from 40.38° to 40.52° with 0.02° step, which are the closest 8 angles to the normal GaP Bragg reflection. According to the direct X-ray beam reflection point at the CCD and the angular resolution of 278.1 pixels/°, the CCD x-y pixel axis is transformed into $Q_y$-$Q_z$ axis for further analysis.

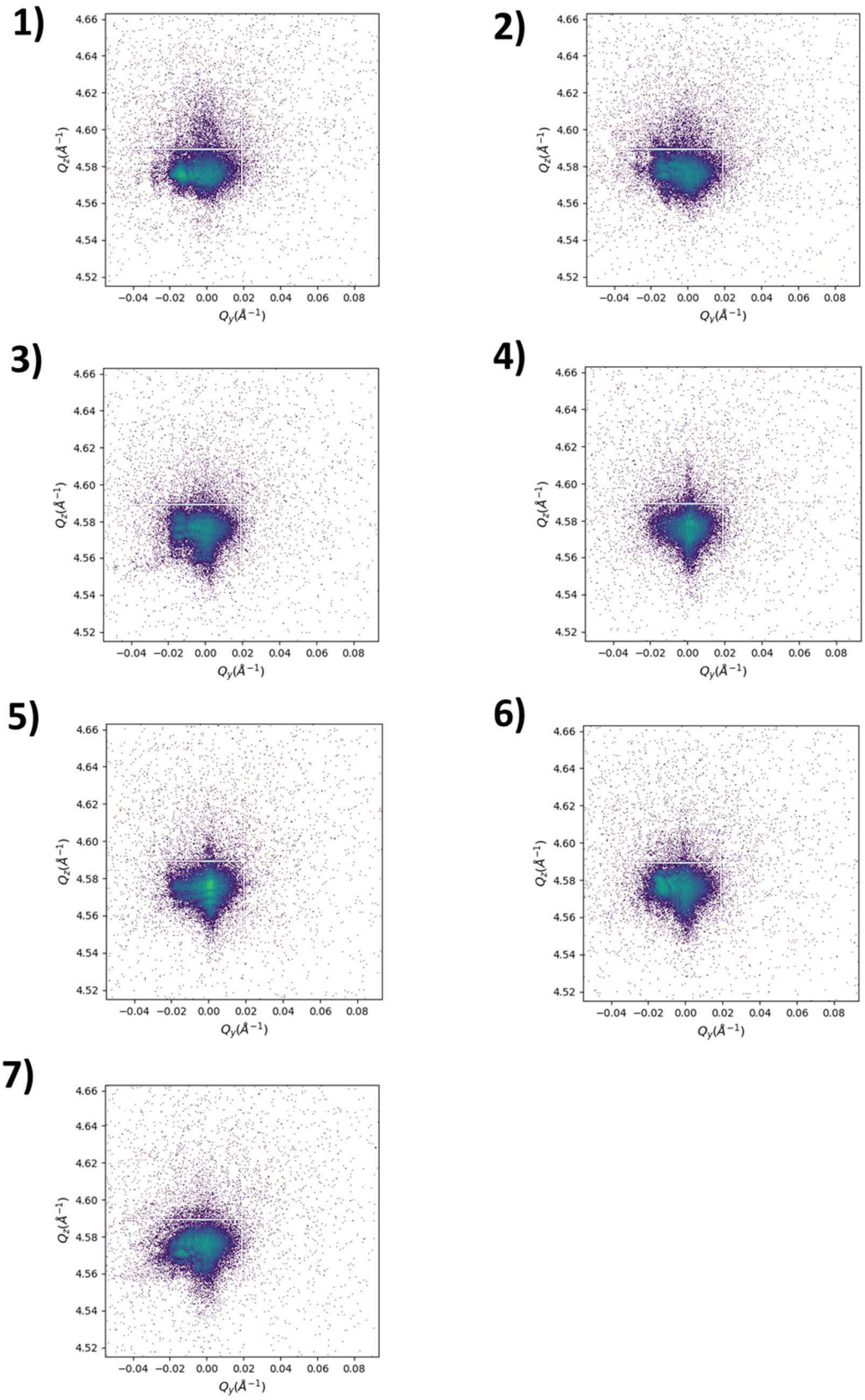


Figure 3-21 The direct CCD images of seven sampling points shown in Figure 3-20 (a).

The CCD images of the seven points at ω = 40.40° are shown in Figure 3-21 as a sample. We observed that, compared to those points in the normal or shift areas, these points in split areas always have a main diffraction spot and a side diffraction spot, and the two spots have nearly the same value along $Q_z$. The norm of the scattering vector **Q** and the distance $\boldsymbol{\delta}$ between the two diffraction peaks are calculated from the CCD images, which is shown as Table 3-1.

| Index | $\|\mathbf{Q}\|$ (Å$^{-1}$) | δ (°) |
|---|---|---|
| 1 | 4.575035 | -0.22542 |
| 2 | 4.578039 | -0.23779 |
| 3 | 4.572039 | -0.2381 |
| 4 | 4.580028 | -0.20016 |
| 5 | 4.576032 | -0.21285 |
| 6 | 4.575016 | -0.15028 |
| 7 | 4.570032 | -0.21313 |

Table 3-1 The norm of the scattering vector **Q** and tilt angle $\delta$ of the side diffraction spot calculated from the CCD images of seven sampling points.

The mean value of the $\|\mathbf{Q}\|$ and $\boldsymbol{\delta}$ for 20 points are 4.575 ± 0.005 Å$^{-1}$ and -0.22 ± 0.02 ° respectively. The $\|\mathbf{Q}\|$ and δ values have less than 0.1% and 10% difference compared to each other respectively, although they have very different shapes in the CCD images. The result suggests that the splitting in different positions is introduced by the same mechanism. In addition, according to Section 2.2.3, these two scattering spots are from two crystallites with nearly same $\boldsymbol{d_{hkl}}$ but different tilt angles.

In conclusion, the splitting scattering spots (peaks if integrated along $\boldsymbol{Q_z}$) show two crystallites with different tilt angles, which may be introduced by the dislocations. Because the strain is relaxed by the dislocations, the local residual strain is lower for the areas with high density of dislocations. Thus, the local out-of-plain lattice constant is lower than the neighborhood areas, and the difference between the out-of-plane lattice constants may be the explanation of the local tilt. A hypothetical sketch of the mechanism is plotted as Figure 3-22.

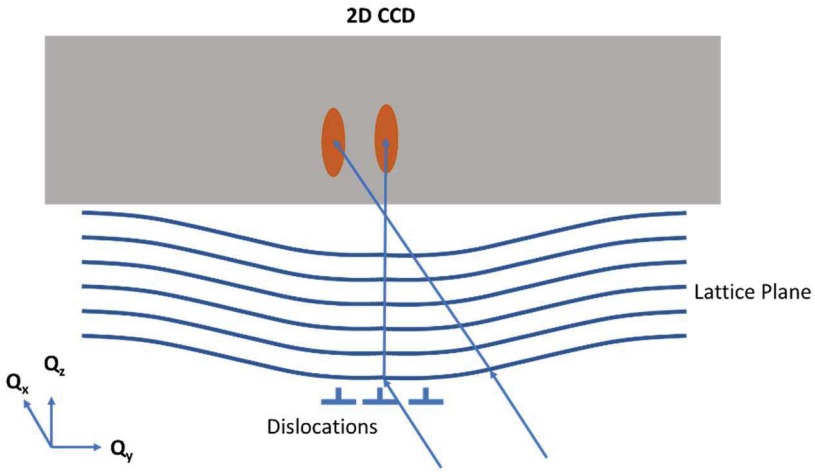


Figure 3-22 Hypothetical sketch of the mechanism related to the “split” area.

## 3.5. Summary

local tilt and strain mappings with sub-micrometer resolution are performed by measuring the (002) and (004) Bragg reflection on a partially relaxed GaP/Si pseudo substrate with the non-destructive K-Map X-ray technique. The complex 5D dataset provides rich local structural information, such as the lattice tilt and the strain. Cross-hatch like patterns parallel to the [-1-10] and [1-10] impact both local tilt and strain mappings. The anisotropy of the distribution of strain may be a result of the Si miscut. Combined with TEM measurements, the relaxation rate measured by K-map on the (004) Bragg reflection shows that 60° dislocations seem to be the main mechanism in the strain relief process, and the distribution of the dislocations is not homogeneous. We suggest that the cross-hatch pattern at the GaP/Si interface influences the free surface roughness, as demonstrated by a strong correlation between the K-Map strain mapping and the surface roughness mapping measured by AFM. Finally, the dislocations are suspected to be the reason, which induces the scattering spot to split.

In this chapter, K-Map has been shown as a free, nondestructive method to extract the local structural properties, such as tilt, strain and dislocation intensity for instance. While, due to the resolution limited by the scattering spot size, only 1D information of the 3D RSM is employed in this work to increase the signal-noise ratio. Certainly, new K-Map experiments performed with more focused beam can provide more local structural details with an analysis on the 2D or 3D RSM datasets instead of 1D, such as the boundary, the MTs, the misfit dislocation type for instance. With this local information from K-Map, a further growth

optimization can be carried out within some specially selected region, for instance, in the application of III-V quantum dot structure analysis.

## References


[1] A. Zhou *et al.*, "A study of the strain distribution by scanning X-ray diffraction on GaP/Si for III–V monolithic integration on silicon," *J. Appl. Crystallogr.*, vol. 52, no. 4, pp. 809–815, Aug. 2019.

[2] T. T. Nguyen, "Sillicon photonics based on monolithic integration of III-V nanostructures on silicon," Ph.D., INSA Rennes, Rennes, 2013.

[3] Y. Wang, "Structural analyses by advanced X-ray scattering on GaP layers epitaxially grown on silicon for integrated photonic applications," Ph.D., INSA Rennes, Rennes, 2016.

[4] B. E. Warren, *X-ray diffraction*, Dover edition, Unabridged and Corrected republication of the work originally published in 1969 by Addison-Wesley Publishing Company. New York: Dover Publications, Inc, 1990.

[5] T. Nguyen Thanh *et al.*, "Structural and optical analyses of GaP/Si and (GaAsPN/GaPN)/GaP/Si nanolayers for integrated photonics on silicon," *J. Appl. Phys.*, vol. 112, no. 5, p. 053521, Sep. 2012.

[6] T. Nguyen Thanh *et al.*, "Synchrotron X-ray diffraction analysis for quantitative defect evaluation in GaP/Si nanolayers," *Thin Solid Films*, vol. 541, pp. 36–40, Aug. 2013.

[7] P. Y. Wang *et al.*, "Quantitative evaluation of microtwins and antiphase defects in GaP/Si nanolayers for a III–V photonics platform on silicon using a laboratory X-ray diffraction setup," *J. Appl. Crystallogr.*, vol. 48, no. 3, pp. 702–710, 2015.

[8] P. Y. Wang *et al.*, "Abrupt GaP/Si hetero-interface using bistepped Si buffer," *Appl. Phys. Lett.*, vol. 107, no. 19, p. 191603, 2015.

[9] O. Durand, A. Letoublon, D. J. Rogers, and F. Teherani, "Interpretation of the two-components observed in high resolution X-ray diffraction ω scan peaks for mosaic ZnO thin films grown on c-sapphire substrates using pulsed laser deposition," *Thin Solid Films*, vol. 519, no. 19, pp. 6369–6373, 2011.

[10] O. Durand, A. Létoublon, D. J. Rogers, F. H. Teherani, C. Cornet, and A. Le Corre, "Studies of PLD-grown ZnO and MBE-grown GaP mosaic thin films by x-ray scattering methods: beyond the restrictive Omega rocking curve linewidth as a figure-of-merit," in Oxide-based Materials and Devices II, 2011, vol. 7940, p. 79400L.

[11] P. Guillemé *et al.*, “Antiphase domain tailoring for combination of modal and 4¯ -quasi-phase matching in gallium phosphide microdisks.,” *Opt. Express*, vol. 24, no. 13, pp. 14608–17, 2016.

[12] P. M. Mooney, J. L. Jordan-Sweet, I. C. Noyan, and S. K. Kaldor, “Observation of local tilted regions in strain-relaxed SiGe/Si buffer layers using x-ray microdiffraction,” *Appl. Phys. Lett.*, vol. 74, no. 5, pp. 726–728, 1999.

[13] J. Matsui *et al.*, “Microscopic strain analysis of semiconductor crystals using a synchrotron X-ray microbeam,” *J. Cryst. Growth,* vol. 237, pp. 317–323, 2002.

[14] V. Mondiali *et al.*, “Dislocation engineering in SiGe on periodic and aperiodic Si(001) templates studied by fast scanning X-ray nanodiffraction,” *Appl. Phys. Lett.*, vol. 104, no. 2, p. 021918, 2014.

[15] M. H. Zoellner *et al.*, “Imaging Structure and Composition Homogeneity of 300 mm SiGe Virtual Substrates for Advanced CMOS Applications by Scanning X-ray Diffraction Microscopy,” *ACS Appl. Mater. Interfaces*, vol. 7, no. 17, pp. 9031–9037, 2015.

[16] Vianne, B., Escoubas, S., Richard, M.-I., Labat, S., Chahine, G., Schülli, T., Farcy, A., Bar, P., Fiori, V. & Thomas, O. (2015). *Microelectron Eng*. 137, 117–123.

[17] T. U. Schülli and S. J. Leake, “X-ray nanobeam diffraction imaging of materials,” *Curr. Opin. Solid State Mater. Sci.*, no. Scient. Rep. 2017, pp. 188–201, 2018.

[18] S. J. Leake *et al*., “The Nanodiffraction beamline ID01/ESRF: a microscope for imaging strain and structure,” *J. Synchrotron Rad.*, vol. 26, no. 2, pp. 571–584, 2019.

[19] G. A. Chahine *et al.*, “Imaging of strain and lattice orientation by quick scanning X-ray microscopy combined with three-dimensional reciprocal space mapping,” *J. Appl. Crystallogr.*, vol. 47, no. 2, pp. 762–769, 2014.

[20] M. Keplinger *et al.*, “Strain distribution in single, suspended germanium nanowires studied using nanofocused x-rays,” *Nanotechnology*, vol. 27, no. 5, p. 055705, Feb. 2016.

[21] D. Kriegner *et al.*, “Twin domain imaging in topological insulator Bi2Te3 and Bi2Se3 epitaxial thin films by scanning X-ray nanobeam microscopy and electron backscatter diffraction,” *J. Appl. Crystallogr.*, vol. 50, no. Pt 2, pp. 369–377, Apr. 2017.

[22] M. Hadjimichael, E. Zatterin, S. Fernandez-Peña, S. J. Leake, and P. Zubko, “Domain Wall Orientations in Ferroelectric Superlattices Probed with Synchrotron X-Ray Diffraction,” *Phys. Rev. Lett.*, vol. 120, no. 3, p. 037602, Jan. 2018.

[23] Y. Takagi, Y. Furukawa, A. Wakahara, and H. Kan, “Lattice relaxation process and crystallographic tilt in GaP layers grown on misoriented Si(001) substrates by metalorganic vapor phase epitaxy,” *J. Appl. Phys.*, vol. 107, no. 6, p. 063506, 2010.

[24] Y. K. Yoğurtçu, A. J. Miller, and G. A. Saunders, “Pressure dependence of elastic behaviour and force constants of GaP,” *J. Phys. Chem. Solids*, vol. 42, no. 1, pp. 49–56, Jan. 1981.

[25] G. Giesecke and H. Pfister, “Präzisionsbestimmung der Gitterkonstanten von AIIIBv‐Verbindungen,” *Acta. Crystallogr.*, vol. 11, no. 5, pp. 369‐371, 1958.

[26] S. D. Carnevale *et al.*, “Applications of Electron Channeling Contrast Imaging for the Rapid Characterization of Extended Defects in III-V/Si Heterostructures,” *IEEE J. Photovolt.*, vol. 5, no. 2, pp. 676–682, 2014.

[27] S. Kishinû, M. Ogirima, and K. Kurata, “A Cross-Hatch Pattern in $GaAs_{1-x}P_x$ Epitaxially Grown on GaAs Substrate,” *J. Electrochem. Soc.*, vol. 119, no. 5, pp. 617–622, 1972.

[28] E. A. Fitzgerald *et al.*, “Relaxed Ge x Si1- x structures for III-V integration with Si and high mobility two-dimensional electron gases in Si,” *J. Vac. Sci. Technol.*, vol. 10, no. 4, pp. 1807–1819, 1992.

[29] M. Albrecht *et al.*, “Surface ripples, crosshatch pattern, and dislocation formation: Cooperating mechanisms in lattice mismatch relaxation,” *Appl. Phys. Lett.*, vol. 67, p. 1232, 1995.

[30] T. Ojala, M. Pietikainen, and D. Harwood, “Performance evaluation of texture measures with classification based on Kullback discrimination of distributions,” in Proceedings of 12th International Conference on Pattern Recognition, Jerusalem, Israel, 1994, vol. 1, pp. 582–585.

[31] T. Ojala, M. Pietikäinen, and D. Harwood, “A comparative study of texture measures with classification based on featured distributions,” *Pattern Recognit.*, vol. 29, no. 1, pp. 51–59, Jan. 1996.

[32] P. Kightley, P. J. Goodhew, R. R. Bradley, and P. D. Augustus, “A mechanism of misfit dislocation reaction for GaInAs strained layers grown onto off-axis GaAs substrates,” *J. Cryst. Growth*, vol. 112, no. 2–3, pp. 359–367, 1991.

[33] Y. Z. Dai and F. P. Chiang, “Strain path and surface roughness,” *Mech. Mater.*, vol. 13, no. 1, pp. 55–57, 1992.

[34] A. Andrews, J. Speck, A. Romanov, M. Bobeth, and W. Pompe, “Modeling cross-hatch surface morphology in growing mismatched layers,” *J. Appl. Phys.*, vol. 91, no. 4, pp. 1933–1943, 2002.

[35] B. Kunert, I. Németh, S. Reinhard, K. Volz, and W. Stolz, “Si (001) surface preparation for the antiphase domain free heteroepitaxial growth of GaP on Si substrate,” *Thin Solid Films*, vol. 517, no. 1, pp. 140–143, 2008.

[36] F. Rovaris *et al.*, “Misfit-Dislocation Distributions in Heteroepitaxy: From Mesoscale Measurements to Individual Defects and Back,” *Phys. Rev. Appl.*, vol. 10, no. 5, p. 054067, Nov. 2018.

# Chapitre 4. X-ray diffraction characterization on the CIGS grown on GaP/Si pseudo-substrate

This chapter is dedicated to introducing the CIGS grown on GaP/Si pseudo-substrate for photovoltaic application. Indeed, photovoltaic technology is becoming one of the main pillars for the energy transition. To date, the best conversion efficiencies have been obtained with multijunction solar cells on III-V substrates. However, maintaining the GaAs or Ge substrates to build these high-efficiency III–V solar cells is costly. The development of low-cost alternative routes in the fabrication of high efficiency tandem solar cells could be a key to grant a leading role in the energy market our strategy is to develop a tandem cell on Si, in order to benefit from both the low cost and technological maturity of Si cells. Indeed, it has been shown that a tandem cell consisting of a 1.7 eV bandgap material on a 1.1 eV Si cell would reach efficiencies up to 37% [1]. Therefore, in collaboration with IPVF (Institut Photovoltaique d'Ile de France) and IMN (Institut des Matériaux Jean Rouxel, de Nantes), we propose to explore tandem junctions associating single crystalline silicon bottom cell, with a bandgap of 1.12 eV and CIGS top cell, specially optimized for working in the blue/UV range (bandgap around 1.7 eV), with an approach based on using wide bandgap GaP intermediate layers.

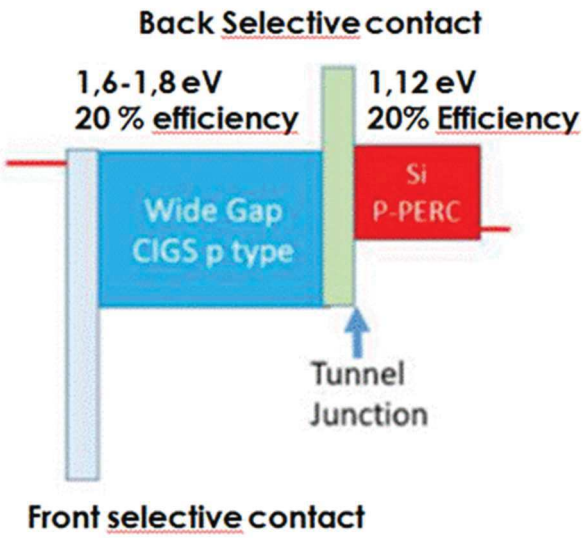


Figure 4-1 Tandem concept with CIGS top cell with selective contacts and Si bottom cell.

To this end, we plan to grow wide band gap CIGS films under epitaxial conditions on GaP to improve the CIGS top cell efficiency, thanks to a reduction of the structural defect density detrimental for the cell performance.

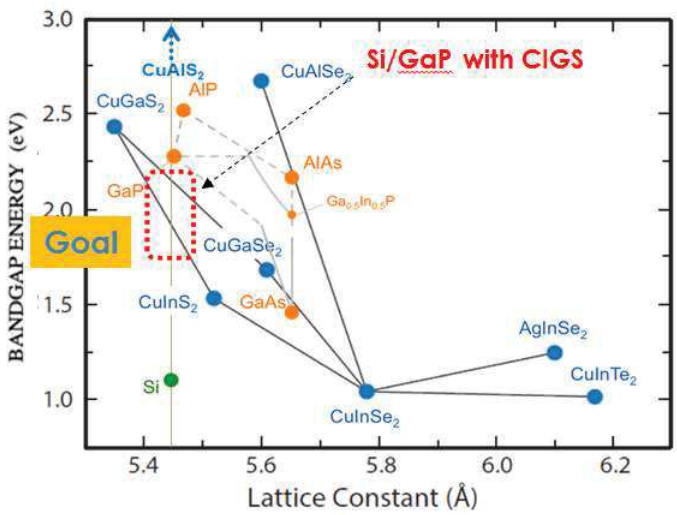


Figure 4-2 structural matching criteria for the epitaxial growth of wide gap chalcopyrite on GaP/Si. Adapted from S. Chichibu et. al. [2]

We expect that the GaP layer (potentially with Al leading to GaAlP ternary compound, in order to adapt the electronic bandlineup) leads to a better structural and electronic matching than with the commonly-used Glass/Mo substrates, so that quasi-epitaxial CIGS-Si tandem solar cells can emerge as cost competitive for the next generation of PV modules.

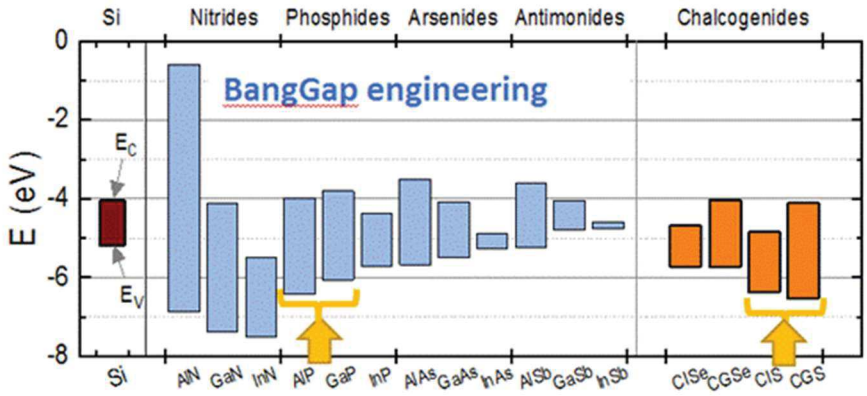


Figure 4-3 band offset criteria for the optimization of photovoltaic properties of the CIGS/Si tandem devices. Values extracted by IPVF from literature data[2]–[6], [7, p.], [8].

As a first step, the aim of this study is to study the growth of $Cu(In,Ga)(S,Se)_2$ (CIGS) on GaP/Si pseudo-substrates, towards the development of the monolithic tandem junctions. First results on the CIGS growth on a GaP/Si (001) pseudo-substrate are reported. [9]

## 4.1. CIGS on GaP/Si pseudo-substrate for photo-voltaic application

CIGS solar cells currently deliver record efficiencies in a small zone of band gap values around 1.1 to 1.2 eV, corresponding to a Ga/(Ga+In) ratio (noted GGI) around 30%, with 22.6% for $CuIn_{0.7}Ga_{0.3}Se_2$ pure selenides (CIGSe) and 22.9% $CuIn_{0.7}Ga_{0.3}(S,Se)_2$ selenosulfides (CIGSSe). The record efficiency (22.9%) has been obtained by Solar Frontier using a two-stage deposition process, without any concentration and for selenosufides.

Concerning wide bandgap CIGS, the in the range of 1.6-1.8 eV, which are needed for top cells, the corresponding solar cells display much lower efficiencies, as compared to the theoretical ones. Recent breakthroughs have occurred when using pure sulfide which raise a record efficiency above 15% at 1.6 eV. [10] These results were obtained by the two-stage process (sulfurization of metal precursors) developed at Solar Frontier. Moreover, a breakthrough of 11.9% has been achieved for pure $CuGaSe_2$ at 1.7 eV using co-evaporation.[11] This shows that rapid progress is made for wide band gap polycrystalline CIGSSe solar cells deposited on classical Mo substrates.

Then, moving to the case of growth of CIGS on GaP(001) and Si(001), an epitaxial growth of $CuGaS_2$ on GaP (100) by MOVPE has been reported in 1987 by Hara, [12] and then extended to a wide class of materials such as $CuGa(S,Se)_2$, or $CuGaSe_2$. [13] Then, other results on the $Cu(Al,Ga,In)(S,Se)_2$ system on GaP (100) has been reported. [2] Epitaxial growth has also been achieved on Si (100). [14] Moreover, Cieslak et al report on direct epitaxial growth on silicon. [15] Epitaxy of CIGS on GaAs substrate is not reported here.

Therefore, an optimization of the epitaxy and electronic band-line-up at the CIGS/Si interface, through the interfacial GaP layer, could lead to the development of high efficiency tandem cells.

## 4.2. Characterization of the CIGS grown on GaP/Si pseudo substrate.

### 4.2.1. CIGS structural description

CIGS is a I-III-$VI_2$ compound semiconductor material, which consists of copper, indium, gallium, selenium and sulfur. In the room temperature, the crystal structure of CIGS is tetragonal system, and the space group is $I\bar{4}2d$. The unit cell of CIGS is shown in Figure 4-4.

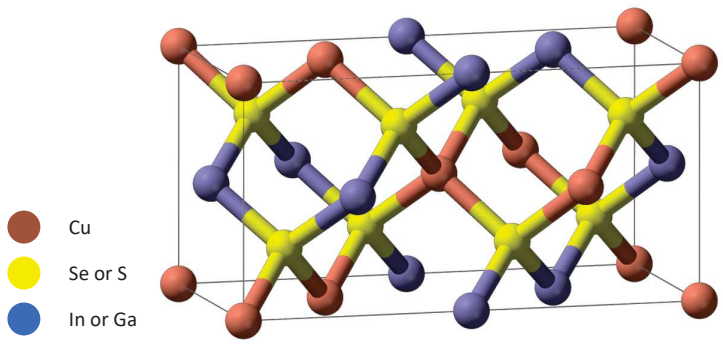


Figure 4-4 The unit cell of CIGS.

This material is a solid solution of $CuIn(Se, S)_2$ (CIS) and $CuGa(Se, S)_2$ (CGS). CIGS is usually expressed with a chemical formula $CuIn_xGa_{1-x}(Se, S)_2$, where the x ranges from 0 (pure CIS) to 1(pure CGS).

The $CuIn_xGa_{1-x}Se_2$, the lattice constants ***a*** and ***c*** range from 0.56 nm to 0.59 nm and from 1.10 nm to 1.17 nm, respectively. [16], [17] The lattice constant increases when x increases

(Figure 4-2). The bandgap of CIGS ranges from 1.0 eV to 1.7 eV. [18] The bandgap increases when x increases (Figure 4-2).

### 4.2.2. Sample preparation

The samples used in this study are $Cu(In_xGa_{1-x})Se_2$ (CIGS) layer, with a nominal thickness equal to 300 nm, grown on two different GaP/Si pseudo substrates, and on Mo/glass for comparison, using co-evaporation in a high vacuum. The detailed growth information is shown as Table 4-1. The purpose of this study is to thoroughly study the CIGS growth on the GaP/Si platform.

#### 4.2.2.a. Preparation of GaP/Si pseudo-substrate

The two undoped GaP/Si pseudo substrates used here were both grown by the Solid Source MBE reactor in Institut FOTON, some years ago during the PhD of Weiming Guo. [19] Since the aim is to study and optimize the growth of CIGS, we do not use in this first step dedicated state-of-the-art GaP/Si platform. First, 90nm (S554) and 600nm (S597) GaP layer respectively grown on (001)-oriented Si 4°-off substrates toward the [110] direction was used for subsequent growth of CIGS. The mismatch between GaP and silicon at room temperature is around 0.37%, so that the critical thickness of GaP grown on Si substrate is about 90nm. [20] Therefore, S554 is partially strained (Figure 4-5 a)), while S597 is nearly fully relaxed (Figure 4-5 b)). For both samples, the MEE with Ga as the pre-layer is applied. The growth temperature (GTs) for S554 is 450°C, while for S597 is 580°C.

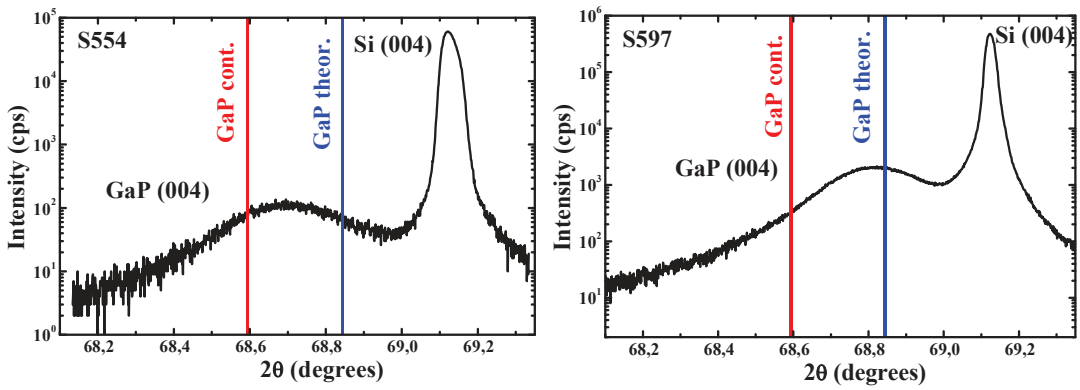


Figure 4-5 ω/2θ XRD scans a) from sample S554 (90nm grown at 450°C) and b) from sample 597 (600nm GaP grown at 580°C). The red tick (resp. the blue one) gives the theoretical fully strained GaP Bragg peak position (resp. the theoretical fully relaxed one).

The samples had not been optimised so that they contain structural defects such as antiphase domains (APDs) and microtwins (MTs) (not shown here) [21], [22].

#### 4.2.2.b. Growth of CIGS

The CIGS growth is performed by Nicolas Barreau et.al. from Institut des Matériaux Jean Rouxel (IMN) – UMR6502 in University Nantes. The two GaP/Si pseudo-substrates are both cut into several parts to perform different deposition methods of CIGS, and CIGS on glass substrate are also respectively grown with the same deposition method for comparison. Two runs have been performed for the CIGS growths, by coevaporation and NaF Postdeposition treatment:

Run #1743: 3-stage isotherm (with post annealing recrystallization).

Run #1744: one-shot isotherm (without recrystallization).

Sample 1743/Glass, 1743/S554 and 1743/S597 are grown by using 3-stage isotherm with recrystallization on glass, S554 and S597 GaP/Si pseudo substrates respectively. Sample 1744/S554, 1744/S597 are grown by one shot isotherm without recrystallization on S554 and S597 GaP/Si pseudo substrates respectively. All the samples are treated by a post-deposition treatment with NaF (NaF-PDF) to increase the hole concentration in CIGS and improve the performance. [23]–[26]

| Index | Sub | Thickness for GaP | GT for Sub | CIGS Growth method |
|---|---|---|---|---|
| 1743/Glass | Glass | | | Three-stage isotherm |
| 1743/S554 | S554 | 90 nm | 450°C | Three-stage isotherm |
| 1743/S597 | S597 | 600 nm | 580°C | Three-stage isotherm |
| 1744/S554 | S554 | 90 nm | 450°C | One-shot isotherm |
| 1744/S597 | S597 | 600 nm | 580°C | One-shot isotherm |

Table 4-1 Growth condition of CIGS on Glass and GaP/Si pseudo substrate.

### 4.2.3. ω/2θ scans and reciprocal space mapping

#### 4.2.3.a. Experiment Setup

The structural properties of the samples are investigated by using the lab setup X-ray diffraction. The ω/2θ scans and RSMs are performed under high-resolution mode. The setup of the experiments is detailed in Section 2.2.4.

4.2.3.b. Discussions

First, the results of ω/2θ scans with 2θ ranged from 20° to 80° on sample 1743/Glass is shown in Figure 4-6.

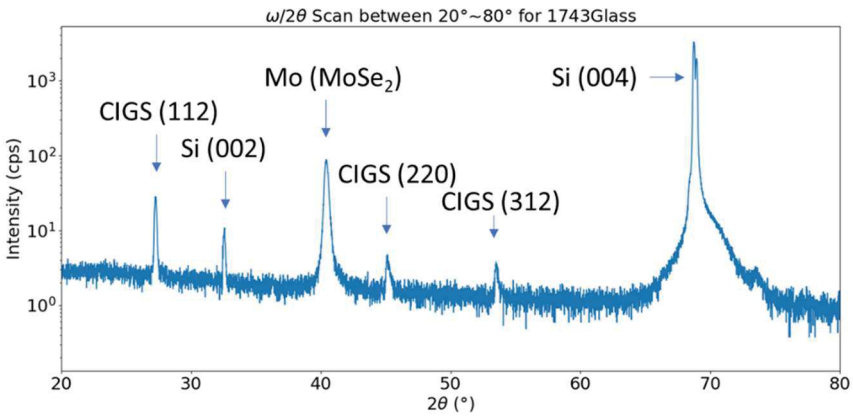


Figure 4-6 ω/2θ scans with 2θ ranged from 20° to 80° for sample 1743/Glass.

The sample is placed on a Si (001) substrate, itself laid on the goniometer sample holder, so that the Si (002) and Si (004) are observed in the diffraction pattern. In the ω/2θ scan from sample 1743/Glass, (112), (220) and (312) diffraction peaks of CIGS are observed. The 2θ positions of these peaks coincide with other literature results [27], [28]. The result indicates that CIGS grown on the glass in 1743/Glass is polycrystalline.

Second, the same scans are performed on the CIGS samples grown on the GaP/Si pseudo-substrates, which are shown in Figure 4-7. As no characteristic peak is observed between 40° and 60°, the scan in this region is not shown. The intensities are plotted in a logarithmic scale in order to enhance all the diffraction peak contributions even weak contributions, and constants are multiplied to these intensities to separate them isometrically. The Si substrates used here are the same, so the curves are aligned in 2θ according to the nominal Si (004) diffraction peak position to reduce experimental error. The curves correspond respectively to 1743/S554, 1743/S597, 1744/S554 and 1744/S597, from top to bottom.

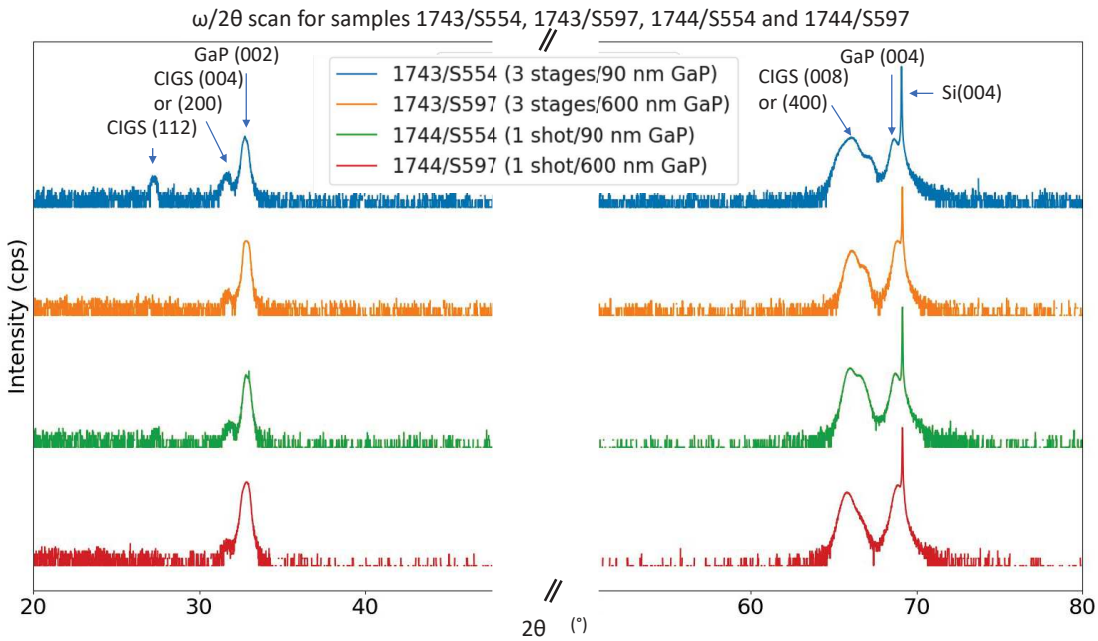


Figure 4-7 ω/2θ scans with 2θ ranged from 20° to 80° for sample 1743/S554, 1743/S597, 1744/S554 and 1744/S597.

Different from 1743/Glass, the diffraction patterns of 1743/S554-1744/S597 in Figure 4-7 mainly show CIGS (004) (or CIGS(200))and CIGS (008) (or CIGS(400))Bragg diffractions, from either a strong fibre texture or an epitaxy. To discriminate between both (fibre texture and epitaxy), we have performed pole figures where the diffraction vector has an in-plane component (results are shown in the next paragraph). 1743/Glass, in some scans, a small CIGS (112) contribution appears, which likely comes from a small CIGS polycrystalline contribution. A selected area electron diffraction (SAED) result performed by TEM on 1743/S554 at IMN, Nantes/France (not shown here) by Eric Gautron (shown in Figure 4-8) also shows a strong diffraction of CIGS along the growth direction, which can be attributed either to a (008) or a (400) Bragg reflection, which coincides with the XRD result.

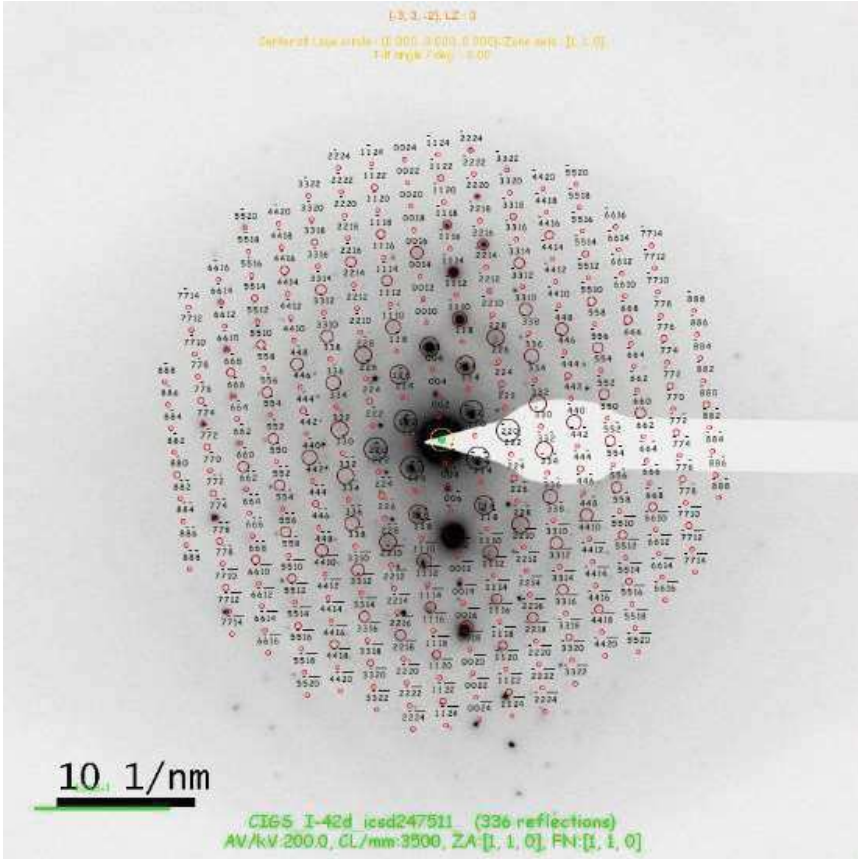


Figure 4-8 A selected area electron diffraction by TEM on 1743/S554.

The thickness of CIGS layers is about 400 nm, measured by HRSTEM, and the CIGS layers are nearly fully relaxed. The composition of the $Cu(In_xGa_{1-x})Se_2$ (given by x) can be calculated by the equation below:

$$x = \frac{a_{EXP} - a_{CGS}}{a_{CIS} - a_{CGS}} \tag{4-1}$$

where $\boldsymbol{a_{EXP}}$ is the lattice constant a or c calculated from measurement, and $\boldsymbol{a_{CIS}}$ and $\boldsymbol{a_{CGS}}$ are the corresponding bulk lattice constants. The 2θ values of the CIGS ranges approximatively from 65.5 degrees to 67.2 degrees. This, again, can be attributed either to a gradient of composition, or a mixing between both (400) and (008) Bragg contributions, or both. To study more thoroughly the structure of the CIGS, IMN has performed on 1743/S554 an Energy-dispersive X-ray spectroscopy (EDX) experiment, shown in Figure 4-9. From this analysis, IMN has measured the atomic fraction profile of all the elements along the growth direction, and in particular the atomic fractions of both the In and Ga elements. The profiles are characteristics of a gradient of composition, coming from a 3-stage CIGS growth. We have made a rough analysis of these profiles and found that the relative atomic fraction between

In and Ga, labelled x in the following, in the $Cu(In_xGa_{1-x})Se_2$ compound ranges roughly from 0.33 to 0.62 (bump of In atomic fraction, at around 550 nm).

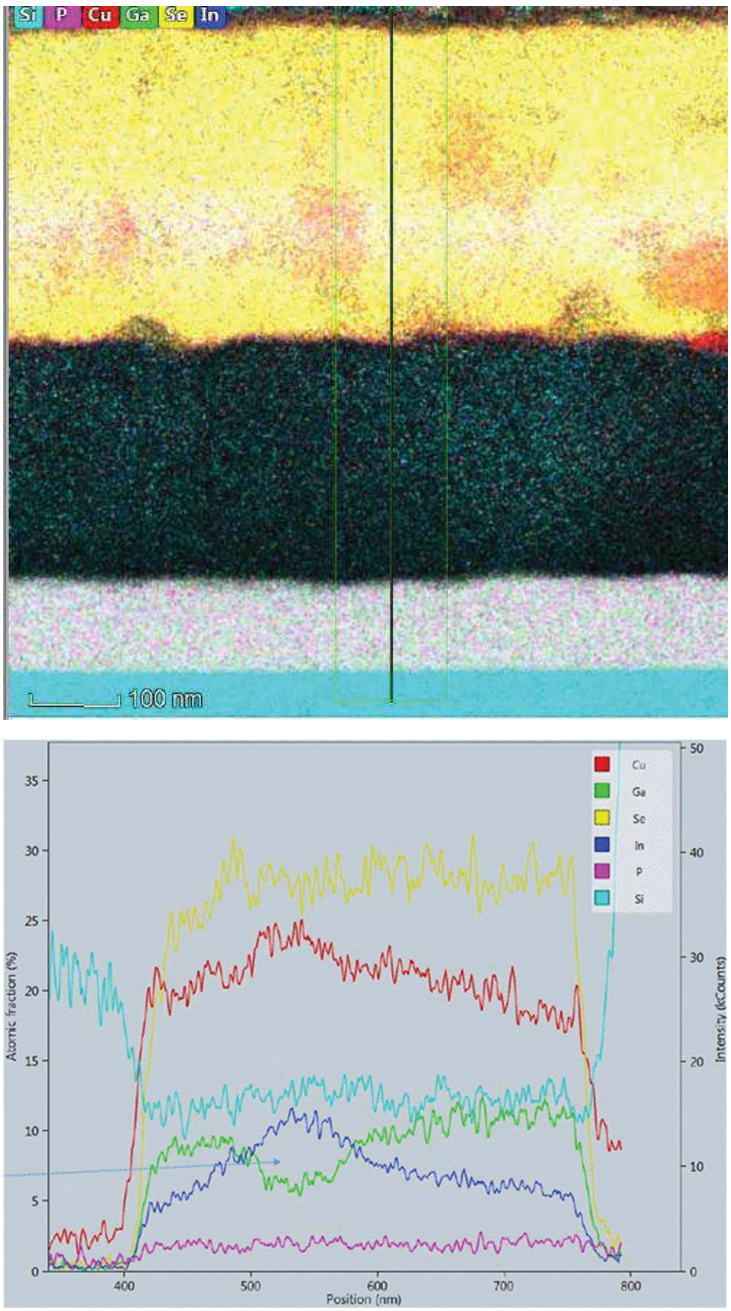


Figure 4-9 EDX cartography performed on the 1743/S554 sample, showing the atomic fraction of all the CIGS elements, in particular the In and Ga elements.

Now, considering the lattice constants of $CuGaSe_2$ (CGS) and $CuInSe_2$ (CIS) reported in the literature [16], [17], as well as the evolution of the lattice parameters between CIS and CGS reported in ref [29], one can draw the lattice parameters with respect to the ***x***, the In composition (

Figure 4-10), as well as the corresponding expected Bragg peak positions for the (008) and (400) reflections. Then, from the EDX experiments, we have deduced the experimental minimum and maximum values of x (vertical lines in

Figure 4-10 right). These values fit pretty well with the experimental range of 2θ in the XRD diffraction profile (Figure 4-7). Although the experimental range of the diffraction peak in 2θ fit better with the large variation of the (008) peak position than the (400) one, it is hard to discriminate between both until now. The textured phase seen in the XRD profiles may come from either a (400) diffraction contribution or a (008) one, or both. Again, this is due to the fact that, in CIGS, the ***c*** parameter is very close to twice the ***a***. While, an RSM study in the next section indicates that the (008) may be the main phase seen here.

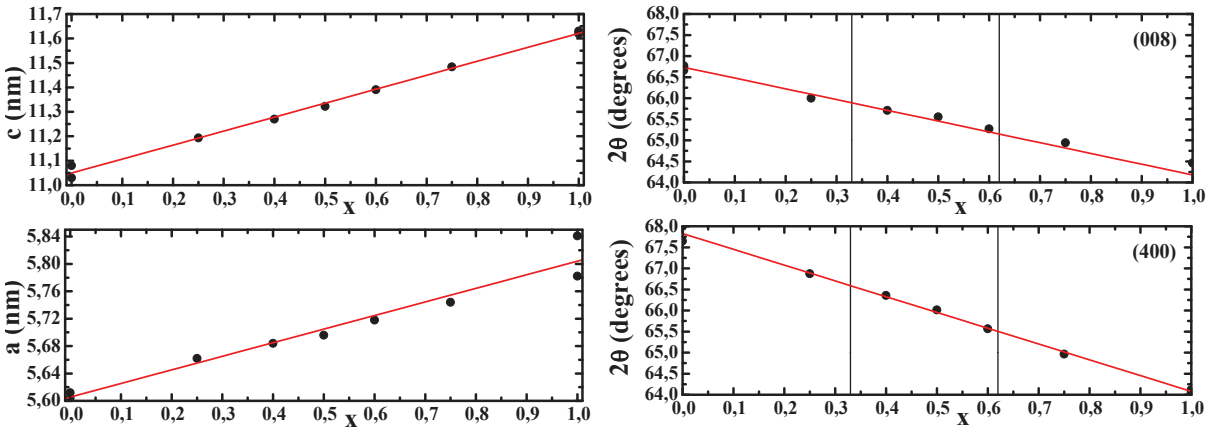


Figure 4-10 Left: evolution of the CIGS lattice parameters with respect to x, according to ref [16], [17] and [29]. Right: variations of the corresponding XRD (008) and (004) Bragg peak positions with respect to x. The vertical lines correspond to the variation of x deduced from the atomic fractions measured by EDX.

To compare the samples grown under different parameters, the ω/2θ scans with 2θ ranged from 25° to 35° and from 65° to 70° are overlapped with each other, which are shown as

Figure 4-11 (a) and (b) respectively.

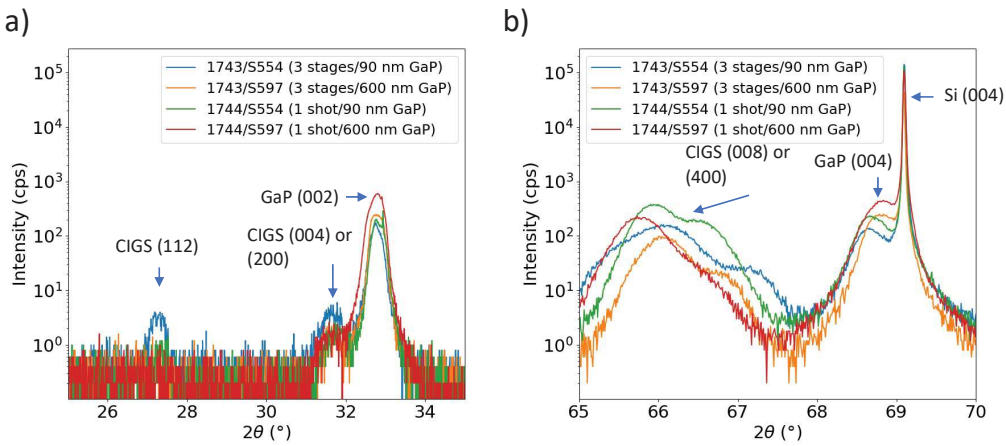


Figure 4-11 ω/2θ scans with 2θ ranged a) from 25° to 35° and b) from 65° to 70° for sample 1743/S554, 1743/S597, 1744/S554 and 1744/S597.

From

Figure 4-11 (a), CIGS (112) are observed to be under the background noise in all the samples except 1743/S554. Double peaks are observed for both 1-shot and 3 stage growth at around 66°. This could correspond to a composition variation that is compliant with EDX mapping (Figure 4-9) and lattice parameter variation dependency (Figure 4-10).

Then, the characteristic diffraction peaks CIGS around 66° in

Figure 4-11 (b) are fitted by the combination of two Pseudo-Voigt functions with different center position. Then, the function with a higher maximum value in the two Pseudo-Voigt function is selected as the primary peak. Thus, the Maximum Intensity (MI), relative intensity (RI) (compared to 1743/S554) and the Integrated Breath (IB) of the primary peak for 1743/S554, 1743/S597, 1744/S554 and 1744/S597 are measured. Considering XRD profiles from longitudinal ω/2θ peaks, the IBs of the peaks may come from two contributions, the correlation lengths of the defects, also called crystallites size, and the microstrains. The results are detailed in Table 4-2. The larger integrated breath can relate to larger density of some defects, for instance MTs, MDs and APDs [30]. These defects are reported to decrease the eventually performance of devices or solar cells based on CIGS or GaP/Si [31]–[35].

| | MI (cps) | RI (%) | IB (Rad) |
|---|---|---|---|
| 1743/S554 | 188.31 | 100 | 0.0184 |
| 1743/S597 | 76.54 | 41 | 0.0131 |

| | | | |
|---|---|---|---|
| 1744/S554 | 318.03 | 169 | 0.0171 |
| 1744/S597 | 163.91 | 87 | 0.0129 |

Table 4-2 Maximum intensity, relative intensity and integrated breath of the primary diffraction peaks at around 66° for 1743/S554, 1743/S597, 1744/S554 and 1744/S597.

We also observed that the MIs of GaP (004) are lower for the CIGS samples grown with 3-stage isotherm compared to those grown with one-shot isotherm. A further comparison between the pseudo-substrate S554 before and after growth is shown in

Figure 4-12. 1743/S554 grown with 3-stage isotherm has a lower MI of GaP (004) compared to that before growth, while 1744/S554 grown with one-shot isotherm has hardly any decrease. The decrease in the MIs is the result of thinner GaP layer. A suspect is that GaP layer is eroded in the 3-stage isotherm growth, which is supported by the rough interface between CIGS and GaP layer by HRTEM, which is shown in Figure 4-13.

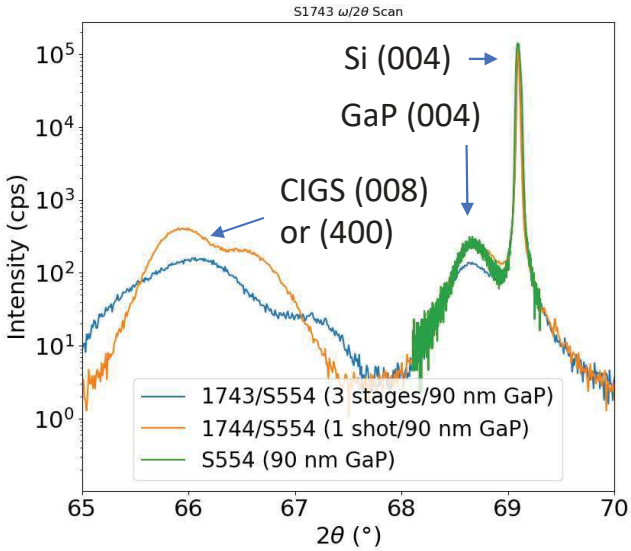


Figure 4-12 ω/2θ scans with 2θ ranged from 65° to 70° for sample 1743/S554, 1744/S554 and GaP/Si pseudo-substrate before growth.

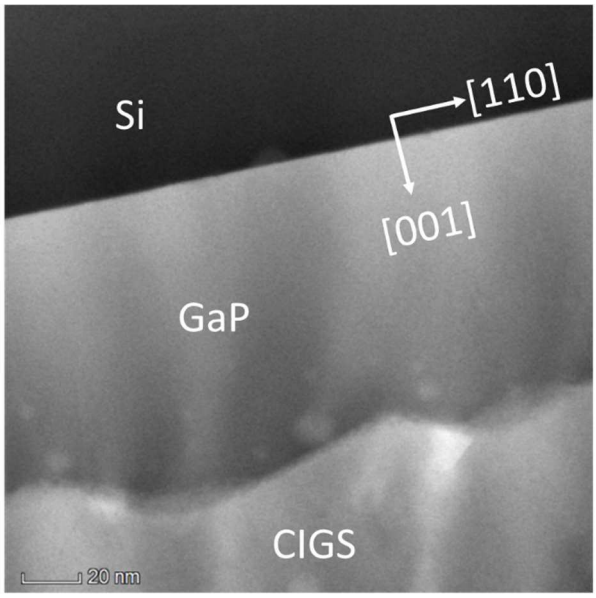


Figure 4-13 Cross-sectional (220) Bright-Field (BF) TEM image of a CIGS sample grown on GaP/Si substrate.

### 4.2.4. Epitaxy of CIGS on the GaP/Si platform.

#### 4.2.4.a. Crystallographic orientation along the growth direction.

RSM is performed around GaP/Si (115) diffraction on 1744/S554, which is shown in Figure 4-14. The observation of the CIGS (1 1 10) Bragg diffraction (fully relaxed) in the RSM containing both the Si (115) and GaP (115), shows that the CIGS is (008) oriented along the growth direction. If assuming the CIGS is (400) oriented along the growth direction, then the diffraction, which is closest to the position, is CIGS (152) or CIGS (512). But the diffraction cannot be CIGS (152) or CIGS (512) according to the lattice constants ***a*** and ***c*** calculated from the high resolution ω/2θ scan.

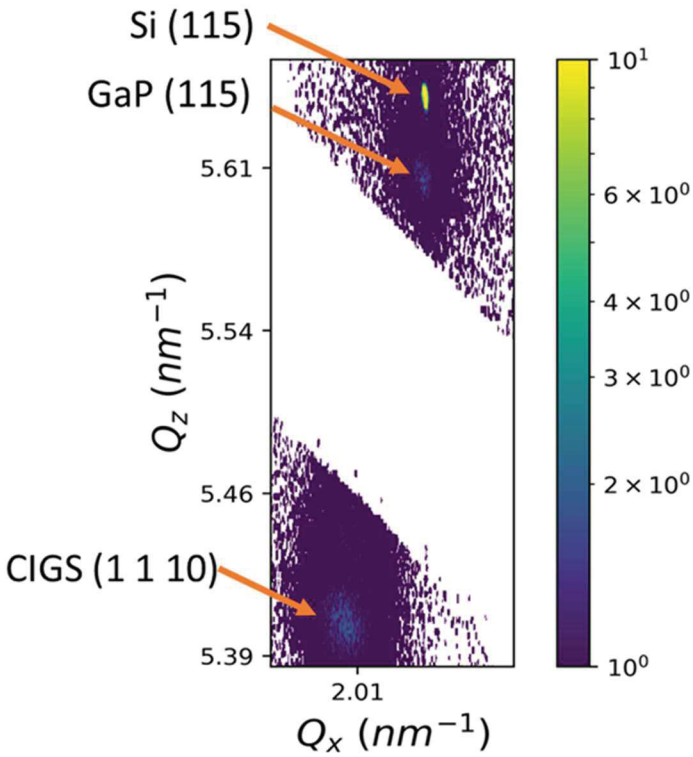


Figure 4-14 RSM image of CIGS (1 1 10) and GaP/Si (115) diffraction.

Moreover, a pole figure performed on a (204) Bragg peak (shown in Figure 4-15 (a) ) and an ω/2θ scan around the (204) Bragg reflection(shown in Figure 4-15 (b)), found at around $\chi$ = 45 degrees and 2θ equal to 45.5 degrees is attributed to a (008) orientation of the crystallographic planes along the growth direction.

A complementary STEM-HAADF (high angle annular dark field) image (performed at IMN) (Figure 4-16) confirms the epitaxial nature of the CIGSe growth, evidenced by the continuity of the atomic planes at the interface and by the Fast Fourier transforms (FFT) of each layer. Other TEM analyses (not shown here) have demonstrated that this leads to a high degree of epitaxy of CIGS on GaP.

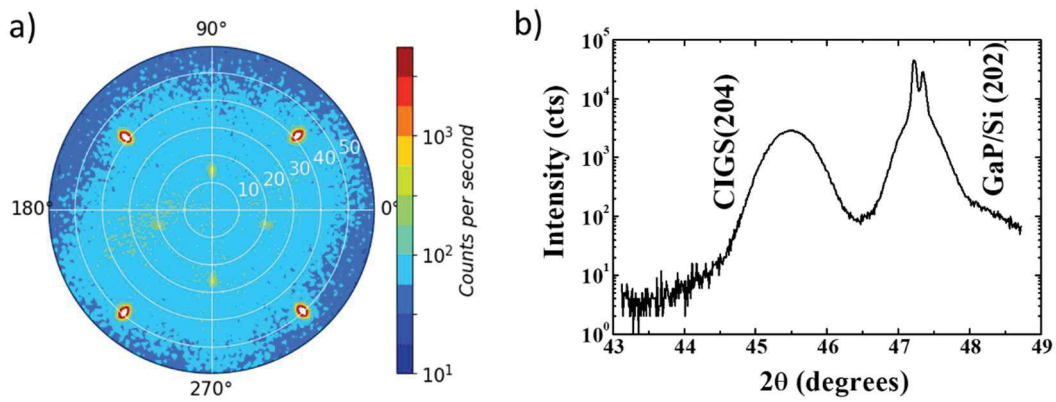

Figure 4-15 a) Pole figure at χ = 45.5°, which corresponds to the (204) CIGS Bragg reflection and b) ω/2θ scan around the (204) Bragg reflection (oblique planes) on sample 1743/S597.

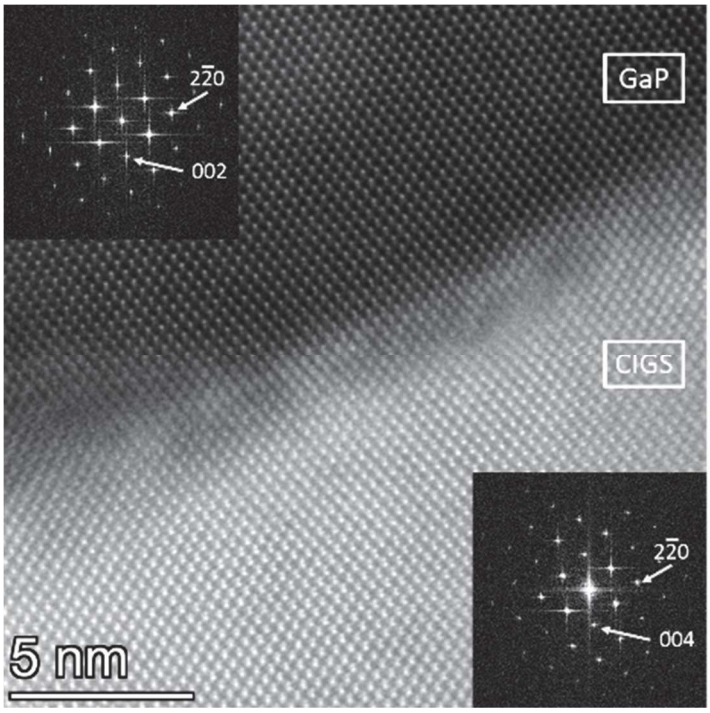


Figure 4-16 STEM-HAADF image of the interface between the CIGS and the GaP layers (with FFT of each layer as insets), showing the epitaxy between both layers.

### 4.2.5. Study of the Pole figures

#### 4.2.5.a. Experiment Setup

The PFs are performed to examine the texture of the CIGS for 1743/S554 – 1744/S597. During the scan, the 2θ was fixed at the Bragg angles of either CIGS (112), or GaP/Si (111), or CIGS (220/204), or Si (220), or CIGS (008), which have been measured by ω/2θ scans before the PFs. Then the **ϕ** rotates from 0° to 180° with a step of 1°, when the **χ** rotates from 0° to 80° (for most of samples) with the same step with ϕ. For each (**ϕ**, **χ**) pair, the scanning time is 1 s. The scanning results are visualized by self-programmed codes driven by Python.

To calculate the intensity of the poles, the PFs are plotted as Figure 4-17. The boundary of poles is identified by a local threshold filter using the Otsu's method [36], and the intensities of the pixel inside the boundary are integrated to be $I_0$. The number of pixels inside the boundary is $N$. The background intensity $I_{bg}$ is the corresponding value of the maximum of the

intensity histogram of the whole image. Thus, the final integrated intensity of the poles ***I*** is equal to $\mathrm{I} = \mathrm{I}_0 - NI_{bg}$.

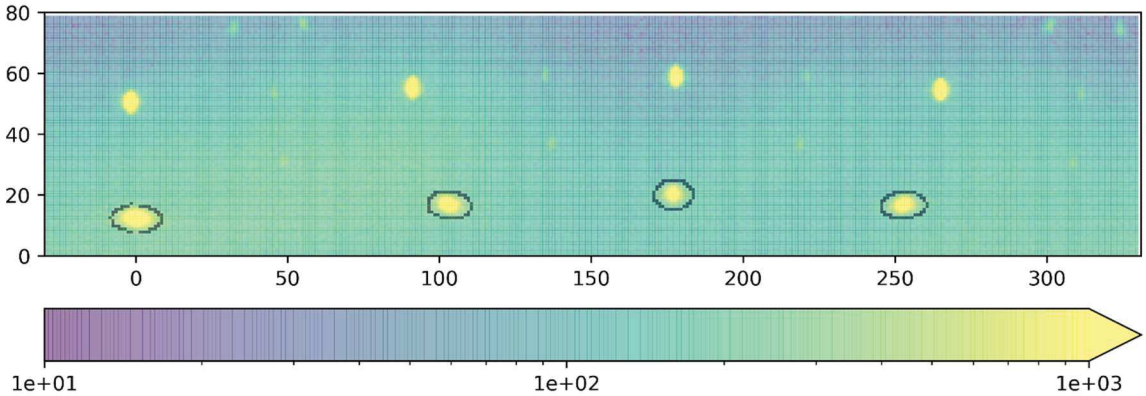


Figure 4-17 An example of the integrated intensity calculation of the poles.

4.2.5.b. Discussions

The angles between some crystallographic planes and nominal (0 0 1), for GaP, Si, and CIGS bulk, is shown in Table 4-3. The ratio ***a***/***c*** of the lattice constants of CIGS is 0.45, the mean value calculated from the results of EDX.

| | crystallographic plane (h, k, l) | | | Angles to (0 0 1) (°) |
|---|---|---|---|---|
| Si or GaP | 0 | 0 | 1 | 0 |
| | 1 | 1 | 1 | 54.73561 |
| | 2 | 0 | 2 | 45 |
| CIGS | 0 | 0 | 1 | 0 |
| | 1 | 1 | 2 | 56.04229 |
| | 2 | 0 | 4 | 43.60282 |

Table 4-3 The angles between some crystallographic planes and nominal (0 0 1), for GaP, Si, and CIGS.

The PFs performed at CIGS (112) and GaP (111), i.e. 27.28° and 28.34°, are shown in Figure 4-18 for 1743/S554 – 1744/S597. The left column shows the PF images at CIGS (112) and the right column shows the PF images at GaP (111). From top to bottom, the images correspond to 1743/S554 – 1744/S597 respectively. The PFs are plotted in a polar coordinate system, with χ to be the radius and ϕ to be the angle.

In the PFs of CIGS (112), there are 3 groups of poles, which have different ϕ values but similar χ values. These poles are labeled as G(roup)-A, G(roup)-B and G(roup)-C in the Figure 4-18.

Due to the vicinal Si substrate, the center of the symmetry of PF is shifted towards direction of the steps. So, a normalization is performed on the position of the poles, and the χ values of the poles are measured. The G-A, G-B and G-C poles located at about 55°, 16° and 78° along the χ axis, respectively. In the PFs of GaP (111), besides the 3 groups referred above, two additional groups of poles G(roup)-D and G(roup)-E are also observed, at about 30° and 53° along the χ axis.

Displaying the highest intensity, the G-A corresponds to the (001) epitaxy of the CIGS on the GaP/Si(001) pseudo substrate, because the angle between the (001) planes and the CIGS (112) planes are around 55°, very close to the angle between GaP(111) and GaP(001). In addition, an ω/2θ scan from 26° to 30° with ϕ = 90° and χ = 55°, i.e. the position of the orange point in Figure 4-18 (e), is performed, which is shown in Figure 4-19 (a). Two well-defined diffraction peaks attributed to the CIGS (112) and GaP/Si (111) are observed. This result corresponds to the fact the CIGS is epitaxially grown on the following epitaxial relationship: CIGS [100] (001) // GaP/Si [100] (001).

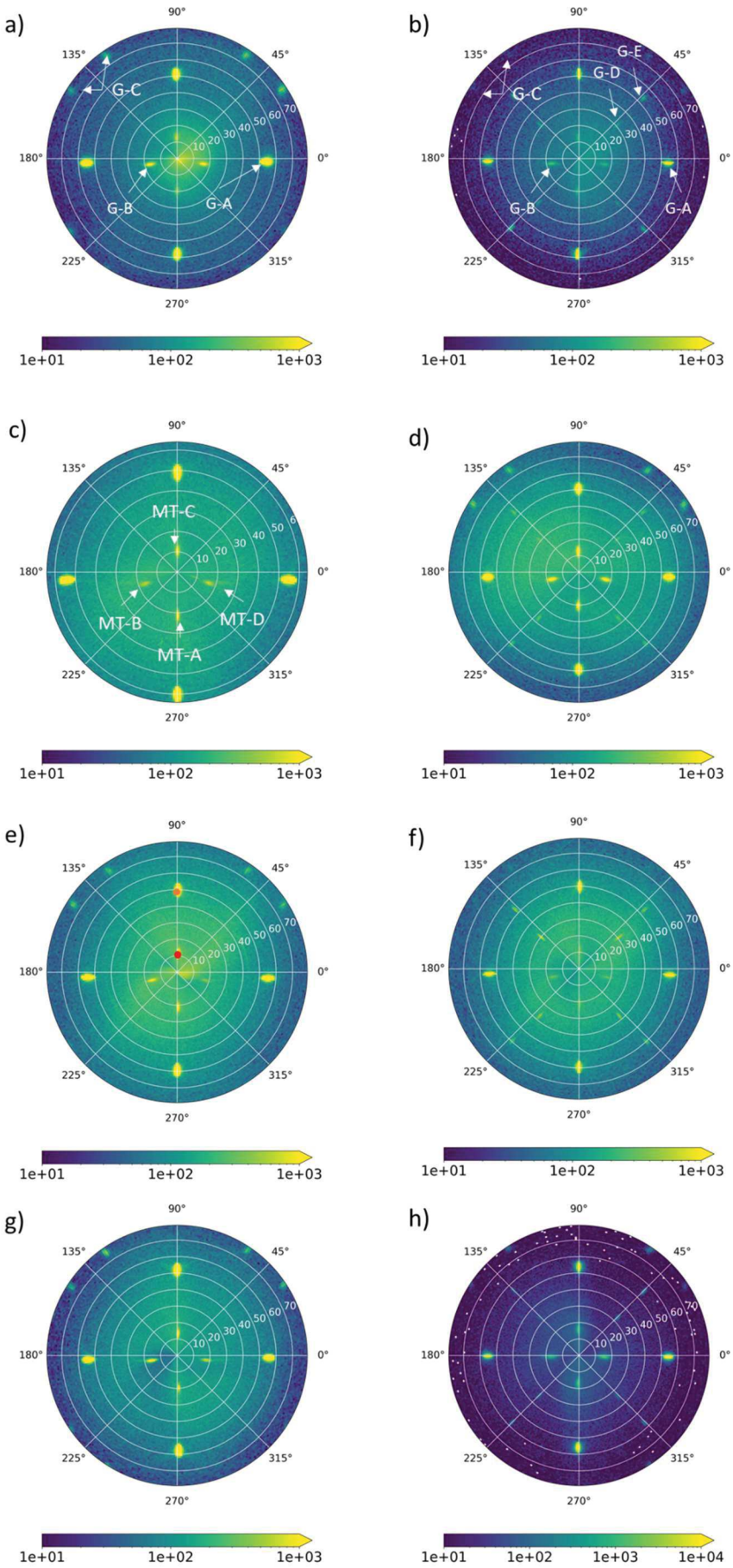
a)
G-C
G-B
G-A
b)
G-E
G-D
G-C
G-B
G-A
c)
MT-C
MT-B
MT-D
MT-A
d)
e)
f)
g)
h)
90°
45°
0°
315°
270°
225°
180°
135°
10
20
30
40
50
60
70
1e+01
1e+02
1e+03
1e+04

Figure 4-18 The Pole Figures at CIGS (112) (left) and at GaP(111), for sample a, b) 1743/S554, c, d) 1743/S597, e, f) 1744/S554 and g, h) 1744/S597.

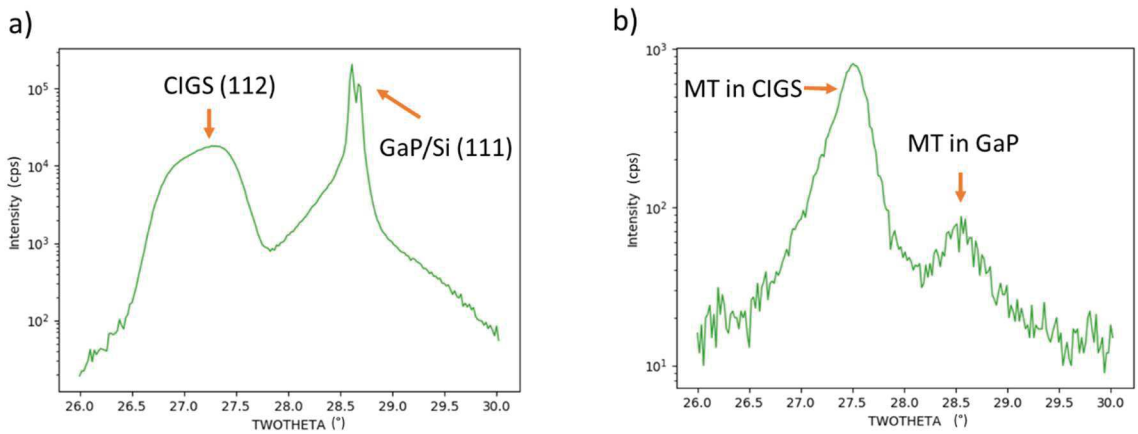


Figure 4-19 ω/2θ scans from 26° to 30° with ϕ = 90° and a) χ = 16° or b) χ = 55°.

The G-B and G-C are weaker poles compared to G-A. According to the literature, The G-B and G-C are associated with micro-twins (MT) (detailed in section 1.4.2) having twin boundaries on the {111} planes. Such MTs have been reported in GaP [25], [26], [37], [38] and many other cubic crystal materials, such as SiC, GaN and SiGe [39]–[41]. G. A. Devenyi et.al. have reported a similar result in InP and AlSb on nominal and vicinal substrates [42]. As the CIGS crystal cell can be seen as two vertically stacked cubic cells, the G-B and G-C poles in CIGS are likely to be poles from the MTs, too. An ω/2θ scan from 26° to 30° with ϕ = 90° and χ = 16°, i.e. the position of the red point in Figure 4-18 (e), is performed. The result shown in in Figure 4-19 (b) indicates that the θ/2θ peak positions corresponding to the CIGS and GaP MT are well-defined. This seems to show that either the MT in the GaP propagate in the CIGS crystalline structure during the CIGS growth, and/or some MT appear at the CIGS/GaP interface. A thorough TEM study is on the way to elucidate this XRD observation.

Moreover, a structure consisting of two CIGS phases is built. One phase represents the nominal CIGS and the other one corresponds to a twinned phase. Sketches of the nominal CIGS planes and the planes of the MTs, which shown as G-B and G-C in the PFs, are shown in Figure 4-20 (a) and (b), respectively. A calculation of the positions of the poles due to the MTs is performed with the structure, and the result is shown in Figure 4-21. The calculated χ values are 15.2° and 78.2° for G-B and G-C respectively. The χ values coincide well with the values measured from PFs.

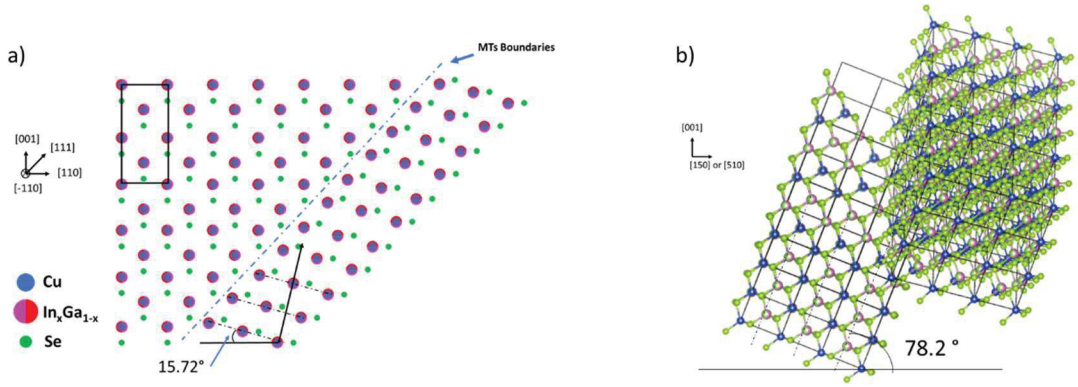


Figure 4-20 Sketches of the nominal CIGS planes and planes of the MTs related to a) G-B and b) G-C poles respectively.

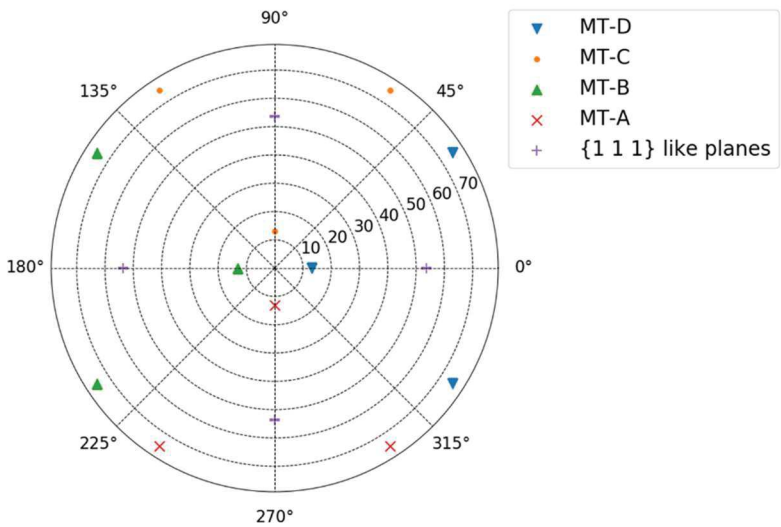


Figure 4-21 Stimulation result of the pole figure of the nominal CIGS planes and planes of the MTs.

The integrated intensities of the poles of G-B are measured. The different MTs are labelled in Figure 4-18 (c), and the result is shown as Table 4-4. If the measured material is the same and the experiment setup is the same, the volume fraction of the MTs should be proportional to the integrated intensity [30].

| | MT-A | MT-B | MT-C | MT-D |
|---|---|---|---|---|
| 1743/S554 | 62650 | 12396 | 77992 | 12248 |
| 1743/S597 | 19196 | 19650 | 40798 | 18442 |
| 1744/S554 | 68042 | 42318 | 112508 | 67684 |
| 1744/S597 | 25670 | 33294 | 48080 | 16512 |

Table 4-4 The Integrated intensities of the poles of G-B.

The G-D and G-E are weakest poles in the five groups of poles and have never been observed in GaP/Si pseudo-substrate in our lab or reported in literature as I know. A possible explanation is that an inter-layer is formed between GaP and CIGS, and [100] of the inter-layer is parallel to [110] of the [110] of the nominal GaP.

## 4.3. First try of CIGSe solar cell on the GaP/Si (001) platform

A 300 nm-thick CIGSe is grown on S553, a 90 nm-thick non-optimised undoped GaP/Si(001), using one-shot isotherm, which is shown in Figure 4-22. Then, the CdS, ZnMgO and Al doped ZnO (AZO) layers are grown in sequence on top of CIGSe to form a solar cell. A top-top electrical contact is applied due to the undoped GaP/Si pseudo-substrate. The external quantum efficiency (EQE) has been measured for the solar cell (black line) and then compared with a PV cell for CIGS grown on glass substrates with the same growth conditions (red line), which is also shown in Figure 4-22. The CIGS solar cell grown on GaP/Si shows only slightly lower EQE than the one grown on glass, in the whole working spectrum. Therefore, the External Quantum Efficiency (EQE) is encouraging, considering that the solar cell structure is far from being optimized, so far. A $J_{SC}$ of 14.5 mA/cm² has been deduced from this EQE. However, the L-I_V curve (I-V curve under AM1.5 illumination) displays a characteristic showing large series and shunt resistances. Moreover, the I-V characteristic displays a behavior which seems to be due to two diodes in series. Therefore, the solar cell needs to be optimized and a top-bottom cell, that is grown on a doped GaP/Si substrate, will be developed soon. However, the result opens promising perspectives for future layer grown on optimized GaP/Si pseudo-substrates.

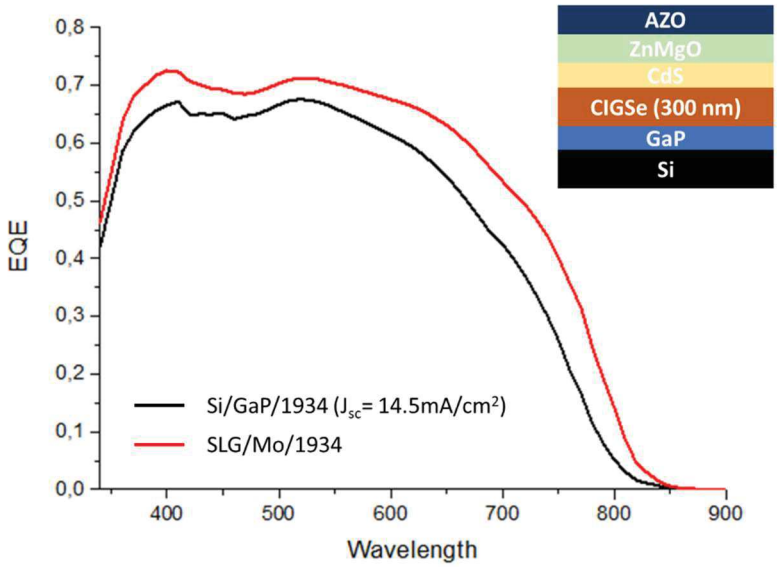


Figure 4-22 External quantum efficiency of CIGS solar cell on non-optimized GaP/Si pseudo-substrate compared to CIGS solar cell on glass (Mo) substrate.

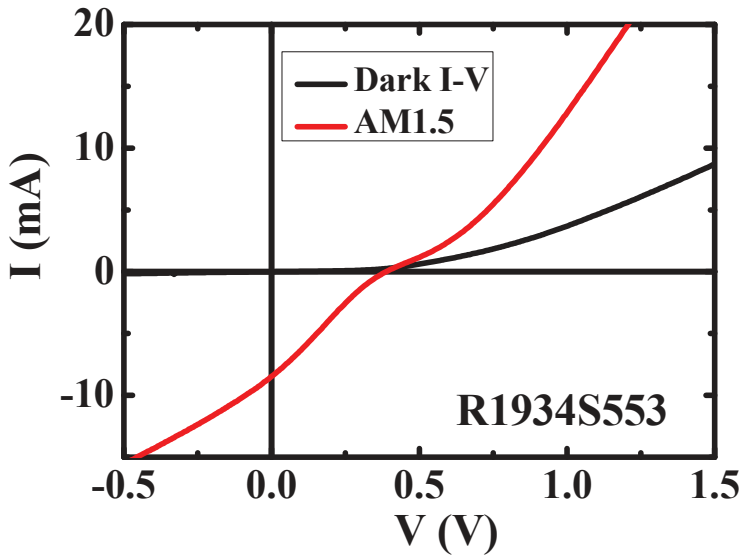


Figure 4-23 Dark I-V and I-V curves under illumination (AM1.5) on the solar cell.

## 4.4. Summary

CIGS has been grown on GaP/Si pseudo-substrate for the application of low-cost and high-efficiency tandem solar cells. XRD experiments, for instance long-range high-resolution ω/2θ scans, RSM and PF are performed on the CIGS/GaP/Si samples to characterize the structural quality. In the long-range high-resolution ω/2θ scans, the CIGS/GaP/Si samples have shown only (00l) diffraction peaks characteristic from either a fiber texture or an epitaxy while a XRD

pattern characteristic from a polycrystal has been measured on the CIGS/Glass samples. In the RSM, the (1 1 10) diffraction of CIGS is observed. In the PFs, a (112) diffraction of CIGS besides the GaP (111) is also observed and confirmed by the transverse scans. Combining the result of TEM with XRD, we have shown that the CIGS growth on the GaP/Si platform leads to a quasi-monocrystalline CIGSe monolayer, as expected. We also observed a few evidences which shown that, depending on the CIGS growth condition, the interface between GaP and CIGS can be damaged. But these results are still too few to conclude the influence of the grown mode or the substrate on the final structural quality. In addition, the MTs in CIGS layer is observed in PFs and a possible formation mechanics is also discussed. At last, the EQE of a CIGSe solar cell on the GaP/Si (001) is measured and compared to a CIGS PV cell grown on glass substrate, which shows the promising future of the CIGS/GaP/Si tandem solar cell.

## References


[1] J. F. Geisz and D. J. Friedman, “III N V semiconductors for solar photovoltaic applications,” *Semicond. Sci. Technol.*, vol. 17, no. 8, pp. 769–777, Aug. 2002.

[2] S. Chichibu, Y. Harada, M. Sugiyama, and H. Nakanishi, “Metalorganic vapor phase epitaxy of Cu(AlxGa1−x)(SySe1−y)2 chalcopyrite semiconductors and their band offsets,” *J. Phys. Chem. Solids*, vol. 64, no. 9–10, pp. 1481–1489, Sep. 2003.

[3] S. Wei and A. Zunger, “Band offsets and optical bowings of chalcopyrites and Zn-based II-VI alloys,” *J. Appl. Phys.*, vol. 78, no. 6, pp. 3846 – 3856, Sep. 1995.

[4] R. Hunger, C. Pettenkofer, and R. Scheer, “Surface properties of (111), (001), and (110)-oriented epitaxial CuInS2/Si films,” *Surf. Sci.*, vol. 477, no. 1, pp. 76–93, Apr. 2001.

[5] M. Turcu, I. M. Kötschau, and U. Rau, “Composition dependence of defect energies and band alignments in the $Cu(In_{1-x}Ga_x)(Se_{1-y}S_y)_2$ alloy system,” *J. Appl. Phys.*, vol. 91, no. 3, pp. 1391–1399, Feb. 2002.

[6] M. Turcu and U. Rau, “Compositional trends of defect energies, band alignments, and recombination mechanisms in the $Cu(In,Ga)(Se,S)_2$ alloy system,” *Thin Solid Films*, vol. 431–432, pp. 158–162, May 2003.

[7] S. Siebentritt and U. Rau, Eds., *Wide-gap chalcopyrites*. Berlin: Springer, 2006.

[8] Ioffe Physico Chemical Institute, “Semiconductors on NSM.” .

[9] D. Lincot *et al.*, “Exploring New Convergences between PV Technologies for High Efficiency Tandem Solar Cells: Wide Band Gap Epitaxial CIGS Top Cells on Silicon Bottom Cells with III-V Intermediate Layers,” in 35th European Photovoltaic Solar Energy Conference and Exhibition, 2018, pp. 23–28.

[10] H. Hiroi, Y. Iwata, H. Sugimoto, and A. Yamada, “Progress Toward 1000-mV Open-Circuit Voltage on Chalcopyrite Solar Cells,” *IEEE J. Photovolt.*, vol. 6, no. 6, pp. 1630–1634, Nov. 2016.

[11] F. Larsson *et al.*, “Record 1.0 V open-circuit voltage in wide band gap chalcopyrite solar cells,” *Prog. Photovolt. Res. Appl.*, vol. 25, no. 9, pp. 755–763, Sep. 2017.

[12] K. Hara, T. Kojima, and H. Kukimoto, “Epitaxial Growth of $CuGaS_2$ by Metalorganic Chemical Vapor Deposition,” *Jpn. J. Appl. Phys.*, vol. 26, no. Part 2, No. 7, pp. L1107–L1109, Jul. 1987.

[13] K. Hara, T. Shinozawa, J. Yoshino, and H. Kukimoto, “MOVPE growth and characterization of I-III-VI2 Chalcopyrite compounds,” *J. Cryst. Growth*, vol. 93, no. 1–4, pp. 771–775, 1988.

[14] K. Oishi, H. Katagiri, S. Kobayashi, and N. Tsuboi, “Growth of Cu(In,Ga)S2 on Si(100) substrates by multisource evaporation,” *J. Phys. Chem. Solids*, vol. 64, no. 9–10, pp. 1835–1838, Sep. 2003.

[15] J. Cieslak *et al.*, “Epitaxial $CuIn_{1-x}Ga_xS_2$on Si(111) ( $0 \leqslant x \leqslant 1$ ) : Lattice match and metastability,” *Phys. Rev. B*, vol. 75, no. 24, Jun. 2007.

[16] C. Rincón and F. Ramírez, “Lattice vibrations of CuInSe2 and CuGaSe2 by Raman microspectrometry,” *J Appl Phys*, vol. 72, no. 9, pp. 4321–4324, 1992.

[17] M. L. Fearheiley, K. J. Bachmann, Y.-H. Shing, S. A. Vasquez, and C. R. Herrington, “The lattice constants of $CuInSe_2$,” *J. Electron. Mater.*, vol. 14, no. 6, pp. 677–683, Nov. 1985.

[18] T. Tinoco, C. Rincón, M. Quintero, and G. S. Pérez, “Phase Diagram and Optical Energy Gaps for $CuInyGa_{1-y}Se_2$ Alloys,” *Phys. Status Solidi A*, vol. 124, no. 2, pp. 427–434, Apr. 1991.

[19] G. Weiming, “Heterogeous MBE growth of GaP on silicon substrate and nanostructure for photonics application Epitaxie,” Ph.D., INSA Rennes, Rennes, 2010.

[20] T. Soga, T. Jimbo, and M. Umeno, “Dislocation generation mechanisms for GaP on Si grown by metalorganic chemical vapor deposition,” *Appl. Phys. Lett.*, vol. 63, no. 18, pp. 2543–2545, Nov. 1993.

[21] P. Y. Wang *et al.*, “Quantitative evaluation of microtwins and antiphase defects in GaP/Si nanolayers for a III–V photonics platform on silicon using a laboratory X-ray diffraction setup,” *J. Appl. Crystallogr.*, vol. 48, no. 3, pp. 702–710, 2015.

[22] P. Y. Wang *et al.*, “Abrupt GaP/Si hetero-interface using bistepped Si buffer,” *Appl. Phys. Lett.*, vol. 107, no. 19, p. 191603, 2015.

[23] P. Reinhard *et al.*, “Features of KF and NaF Postdeposition Treatments of $Cu(In,Ga)Se_2$ Absorbers for High Efficiency Thin Film Solar Cells,” *Chem. Mater.*, vol. 27, no. 16, pp. 5755–5764, 2015.

[24] F. Pianezzi *et al.*, “Unveiling the effects of post-deposition treatment with different alkaline elements on the electronic properties of CIGS thin film solar cells,” *Phys. Chem. Chem. Phys.*, vol. 16, no. 19, pp. 8843–8851, 2014.

[25] B. Bissig *et al.*, “Effects of NaF evaporation during low temperature Cu (In, Ga) Se2 growth,” *Thin Solid Films*, vol. 582, p. 56, 2015.

[26] E. Handick *et al.*, “NaF/KF post-deposition treatments and their influence on the structure of Cu (In, Ga) Se 2 absorber surfaces,” presented at the P*roc.* of IEE 44th Photovoltaic Specialist Conference, 2016, pp. 0017–0021.

[27] M. G. Panthani *et al.*, “Synthesis of $CuInS_2$, $CuInSe_2$, and $Cu(In_xGa_{1-x})Se_2$ (CIGS) Nanocrystal ‘Inks’ for Printable Photovoltaics,” *J. Am. Chem. Soc.*, vol. 130, no. 49, pp. 16770–16777, 2008.

[28] D. Fraga, E. Barrachina, I. Calvet, T. Stoyanova, and J. B. Carda, “Developing CIGS solar cells on glass-ceramic substrates,” *Mater. Lett.*, vol. 221, pp. 104–106, 2018.

[29] D. K. Suri, K. C. Nagpal, and G. K. Chadha, “X-ray study of $CuGa_xIn_{1-x}Se_2$ solid solutions,” *J. Appl. Crystallogr.*, vol. 22, no. 6, pp. 578–583, Dec. 1989.

[30] B. E. Warren, *X-ray diffraction*, Dover edition, Unabridged and Corrected republication of the work originally published in 1969 by Addison-Wesley Publishing Company. New York: Dover Publications, Inc, 1990.

[31] C. J. Gibbings, D. L. Murrell, D. M. Cooper, and P. C. Spurdens, “Impact of GaInP growth by MOVPE on laser performance,” in IEEE Colloquium on III-V Compound Semiconductor Materials Growth, 1992, pp. 5/1-5/4.

[32] T. Nakada, K. Furumi, and A. Kunioka, “High-efficiency cadmium-free Cu(In,Ga)Se/sub 2/ thin-film solar cells with chemically deposited ZnS buffer layers,” *IEEE Trans. Electron Devices*, vol. 46, no. 10, pp. 2093–2097, Oct. 1999.

[33] C. L. Andre *et al.*, “Impact of dislocations on minority carrier electron and hole lifetimes in GaAs grown on metamorphic SiGe substrates,” *Appl. Phys. Lett.*, vol. 84, no. 18, pp. 3447–3449, May 2004.

[34] A. Beyer, I. Németh, S. Liebich, J. Ohlmann, W. Stolz, and K. Volz, “Influence of crystal polarity on crystal defects in GaP grown on exact Si (001),” *J. Appl. Phys.*, vol. 109, no. 8, p. 083529, 2011.

[35] C. Heidelberger and E. A. Fitzgerald, “GaAsP/InGaP HBTs grown epitaxially on Si substrates: Effect of dislocation density on DC current gain,” *J. Appl. Phys.*, vol. 123, no. 16, p. 161532, Apr. 2018.

[36] N. Otsu, “A Threshold Selection Method from Gray-Level Histograms,” *IEEE Trans. Syst. Man Cybern.*, vol. 9, no. 1, pp. 62–66, Jan. 1979.

[37] T. Nguyen Thanh *et al.*, “Synchrotron X-ray diffraction analysis for quantitative defect evaluation in GaP/Si nanolayers,” *Thin Solid Films*, vol. 541, pp. 36–40, Aug. 2013.

[38] T. Grassman *et al.*, “Control and elimination of nucleation-related defects in GaP/Si(001) heteroepitaxy,” *Appl. Phys. Lett.*, vol. 94, no. 23, p. 232106, 2009.

[39] X. H. Zheng *et al.*, “Comprehensive analysis of microtwins in the 3C–SiC films on Si(001) substrates,” *J. Cryst. Growth*, vol. 233, no. 1, pp. 40–44, Nov. 2001.

[40] K. Arimoto *et al.*, “Crystalline morphologies of step-graded SiGe layers grown on exact and vicinal (110) Si substrates,” *J. Cryst. Growth*, vol. 311, no. 3, pp. 809–813, Jan. 2009.

[41] B. Qu, X. H. Zheng, Y. T. Wang, S. M. Lin, H. Yang, and J. W. Liang, “Polarity dependence of hexagonal inclusions and cubic twins in GaN/GaAs(001) epilayers measured by conventional X-ray pole figure and grazing incident diffraction pole figure,” *J. Cryst. Growth*, vol. 226, no. 1, pp. 57–61, Jun. 2001.

[42] G. Devenyi *et al.*, “The role of vicinal silicon surfaces in the formation of epitaxial twins during the growth of III-V thin films,” *J. Appl. Phys.*, vol. 110, no. 12, p. 124316, 2011.

# Chapitre 5. General conclusions and perspective work

## 5.1. Summary and conclusions

This thesis focuses on the structural analysis of the GaP/Si pseudo substrates and the application of the pseudo substrate in the CIGS/GaP/Si tandem solar cell. The final purpose is the growth of high-quality GaP/Si pseudo substrate, which have a low defect density and homogenous distribution of defects. The main work in the thesis can be divided into two part:

In the first part, an advanced sub-micrometer-beam X-ray scattering, quicK continuous Mapping, have been employed for a local structure characterization of the GaP epitaxy layer on Si substrate. The diffraction pattern received by the 2D sensors is processed with a program called XSOCS into a multi-dimension dataset which consist of 2D location information from the real space, 3D structural information from the reciprocal space and the diffraction beam intensity. The result, along with general structure measurements by XRD, surface roughness measurements by AFM and local evidence of dislocations by TEM, have allowed understanding the effect of the 60° dislocations (misfit dislocations) on the relaxation process and the final surface roughness of the epitaxial layer.

60° dislocations seem to be the main mechanism in the strain relief process of GaP/Si pseudo substrate, along with the experimental results and the literature. The distribution of the 60° dislocations is also observed to be not homogenous, which tends to form bunches. The cross-hatch pattern at the GaP/Si interface is also believed to influence the free surface roughness, as demonstrated by a strong correlation between the K-Map strain mapping and the surface roughness mapping measured by AFM. An assumption on the local tilt, which may be introduced by the dislocation bunches, is also proposed after a further analysis on the K-map result.

In the second part, CIGS grown on GaP/Si pseudo-substrate for photovoltaic application is introduced. The epitaxy quality is analyzed based on long-range ω/2θ scan, reciprocal space maps and pole figures using laboratory XRD setups. The CIGS is demonstrated to be epitaxially grown on the GaP/Si pseudo-substrate, which is confirmed in local structure by TEM and in a larger area by pole figures, which is shown in Figure *5-1*. The MTs are also observed in the PFs, and the formation mechanism has been discussed along with the experimental results and based on the assumptions proposed in literature.

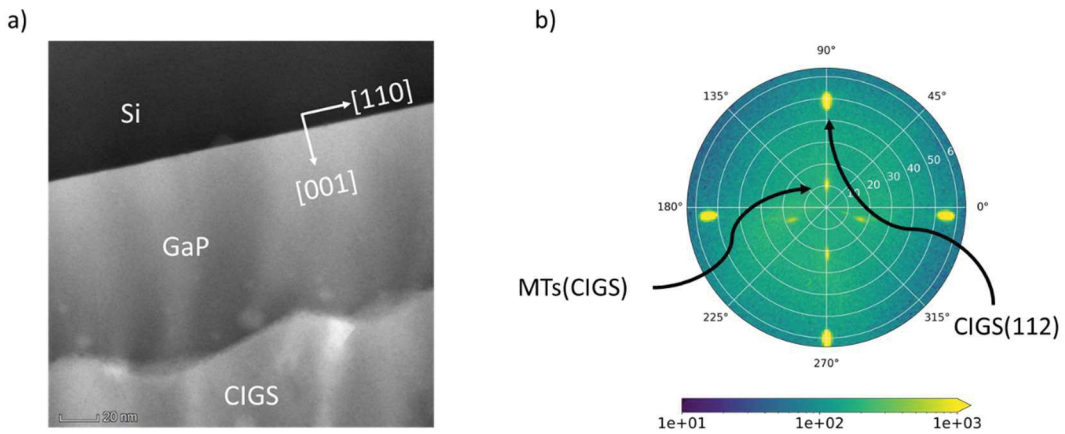


Figure 5-1 a) TEM images of CIGS/GaP/Si b) pole figure of CIGS/GaP/Si, which shows a clear CIGS (112) diffraction, as well as the MTs form in the CIGS layer. A transverse scan around the CIGS (112) position confirmed the diffraction is not an illusion from GaP (111).

As a conclusion, a new non-destructive and fast method to quantify the local structural quality of GaP/Si platform with sub-micrometer-beam X-ray scattering is proposed, which can be used to optimize the growth conditions for the fabrication. This platform is used to fabricate CIGS/GaP/Si tandem solar cell, which explores a low-cost alternative route in the fabrication of high efficiency tandem solar cells.

## 5.2. Suggestions for future works

1. For K-map, a more focused X-ray beam, which is recently developed by ESRF staff [1], opens the route for detection of other defects, for instance APBs. Specially fabricated samples with for instance a grid pattern including numbering in order to be able to correlate the same area analysed through different reciprocal space positions such as (002), (004) (006) and (115), forbidden or MT reflection positions. The potential of the multi-dimension dataset in the K-map is still large, because the data process method in the work did not use up all the dimensions. A combination of K-map and electro-optical experiments which have a similar spatial resolution, for instance, scanning electron microscopy, can furtherly reveal the influence of dislocation bunches on the electro-optical properties.
2. It is important to study the formation mechanism of the dislocation bunches. It should be of great interest to study the GaP samples grown on vicinal substrates with different miscut, in order to reveal the relationship between the dislocation bunches and the steps on the substrate surface.

3. For CIGS grown on GaP/Si, the electro-optical properties of the tandem solar cells are still waiting for the test. The abnormal diffraction in the pole figures, which may lead by the interface between GaP and CIGS, requires further analysis and this will lead to an improvement of the CIGS growth, as well as the obtaining of a 1.7 eV gap CIGS likely with pure sulfur CIGS lattice-matched on the GaP/Si platform. Finally, forthcoming developments of the CIGS top cell on a doped GaP/Si platform , for top-bottom cell configuration, will allow the rapid development of a CIGS/Si tandem solar cell with an tunnel junction (all Si) between both sub cells.

## References

[1] S. J. Leake *et al.*, "The Nanodiffraction beamline ID01/ESRF: a microscope for imaging strain and structure," *J. Synchrotron Rad.*, vol. 26, no. 2, pp. 571–584, 2019.

# Appendices

## A1. Performance of PF scans for Microtwin (MT) quantification

During PFs scan, the 2θ was fixed at the Bragg angles of either CIGS (112), or GaP/Si (111) of the test samples. Then the ϕ rotates from 0° to 180° with a step of 1°, when the χ rotates from 0° to 80° (for most of samples) with the same step with ϕ. For each (ϕ, χ) pair, the scanning time is 1 s. The scanning results are visualized by self-programmed codes driven by Python.

The definition of the MT-A to MT-D are shown in Figure Figure_ex 1 (detailed in section 1.4.2). To calculate the intensity of the poles, the PFs are plotted as Figure_ex 2. The x-axis of image is ϕ and the y-axis is χ. The four poles with lower χ values are from the MTs. Because the miscut of the substrates is towards [110] in our samples, the poles with the lowest χ is MT-C. Two selection methods for the integration area of MTs poles are used by us.

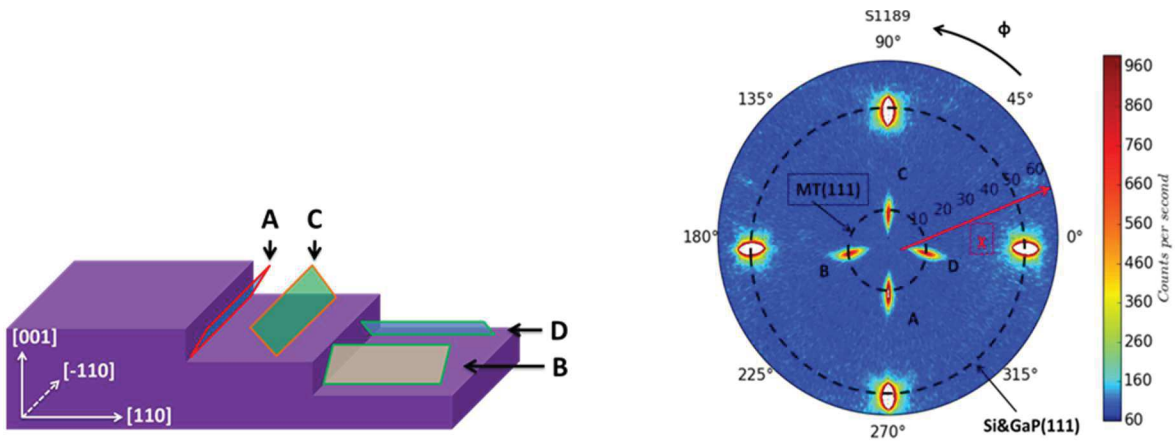


Figure_ex 1. The definition of the MT-A to MT-D.

The method for the integration area selection is shown in Figure_ex 2. A 1°(vertical) × 20° (horizontal) area centred at the maximum of the MT poles are selected. The intensities of the pixel inside the selected areas are integrated to be $\boldsymbol{I_0}$. The number of pixels inside the boundary is $\boldsymbol{N}$. The background intensity $\boldsymbol{I_{bg}}$ ($counts\ per\ second\ (cps)$) is the corresponding value of the maximum of the intensity histogram of the whole image. Thus, the final integrated intensity of the poles $\boldsymbol{I}$ ($counts\ per\ second\ (cps)$) is equal to $\mathrm{I} = \mathrm{I}_0 - NI_{bg}$.

The volume fraction $\boldsymbol{V_{pct}}$(%) is:

$$\mathrm{V_{pct}}(\%) = I * \eta_{corr} \tag{1}$$

where $\boldsymbol{\eta_{corr}}$ is the correction coefficient.

The correction coefficient is determined for each MT from a reference sample with the same thickness and the same structure as the test samples. For the reference sample, both MT quantification and Rocking Curve (RC) quantification is performed. Thus, the correction coefficient $\boldsymbol{\eta_{corr}}$ is:

$$\eta_{corr} = \frac{1}{\mathrm{I_{PF}}} RCV_{pct} \tag{2}$$

where $\boldsymbol{I_{PF}}$ $(counts\ per\ second\ (cps))$ is the integrated intensity of the poles in the reference sample and $\mathbf{RCV_{pct}}$ (%) is volume fraction of MTs measured by RC quantification.

During the RC quantification, $\mathbf{RCV_{pct}}$ is calculated as below:

$$\frac{1}{RCV_{pct}} = \frac{1}{\mathrm{I_{exp}}} \frac{\Phi_0}{\dot{\omega}} \mathrm{r_0^2} \frac{\mathrm{V}\lambda^3 \mathrm{F_T^2}}{\mathrm{v_a^2}} PL \tag{3}$$

where $\boldsymbol{I_{exp}}$ $(counts\ per\ second\ (cps))$ is the integrated intensity of the RC signals, $\boldsymbol{\Phi_0}$ (rad) is the intensity of the incident beam, $\boldsymbol{\dot{\omega}}$ (rad/s) is the angular velocity, $\boldsymbol{r_0^2}$ is the scattering cross-section of the electron, $\boldsymbol{V}$ is the effective volume of unit cell, $\boldsymbol{\lambda}$ (m) is the incident X-ray beam wavelength, $\boldsymbol{F_T}$ is unit cell structure factor taking into account of the Debye-Walle factor, and ***PL*** is the Lorentz-polarization factor.

The method is developed during the thesis of Yanping Wang, *Structural analyses by advanced X-ray scattering on GaP layers epitaxially grown on silicon for integrated photonic applications,* 2016. The details of the performance of the experiments could be found in her thesis document. The integration area selection method is changed to the current one during this thesis.

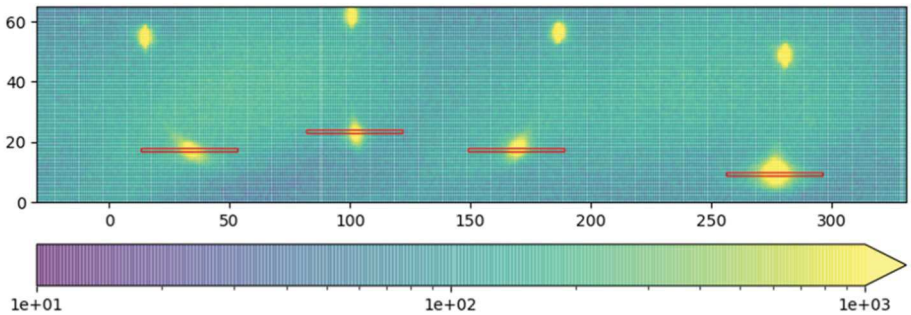


Figure_ex 2. Poles figures of S2062 and the sketch of integration area selection method.

# Résumé de thèse

Les matériaux semi-conducteurs sont des briques de base à la fois pour la conversion de l'énergie solaire et les technologies de l'information (micro et optoélectronique). Le silicium, en tant que matériau semi-conducteur le plus mature, est largement utilisé dans les industries de la microélectronique et du photovoltaïque, en raison de son abondance naturelle, de son faible coût, de sa grande pureté et de la disponibilité sous forme de gros monocristaux. Néanmoins, la bande interdite indirecte du Si empêche à la fois une émission de lumière efficace et une absorption efficace, ce qui limite ses applications. De l'autre côté on trouve un grand nombre de semi-conducteur direct parmi les composés III-V qui sont donc particulièrement appréciés pour les applications en photonique, malgré des coûts de fabrication élevés. Ainsi, l'intégration des semi-conducteurs III-V sur silicium est considérée comme la pierre angulaire de l'intégration cohérente de la photonique dans la technologie du silicium mature et des cellules solaires à haut rendement et à faible coût. Parmi les différentes approches, l'hétéroépitaxie est considérée comme la technique la plus prometteuse et la plus attrayante en raison de son faible coût et de sa capacité d'intégration à grande échelle.

Le phosphure de gallium (GaP), qui présente un désaccord de maille 0,37% à température ambiante, par rapport au réseau cristallin du silicium, a été utilisé dans ces travaux, comme couche intermédiaire efficace pour l'intégration ultérieure d'hétérostructures à base de III-V. Les défauts de l'hétéroépitaxie de GaP et de Si, tels que les dislocations, les micro-macles (MT) et les parois de domaines d'antiphase, peuvent limiter les propriétés électro-optiques des dispositifs finaux (rendement, durabilité…). L'objectif de la thèse est donc de caractériser les défauts structuraux et de développer des méthodes de caractérisation à l'échelle sub-micrométrique en d'améliorer les propriétés de la plateforme GaP / Si et de mieux les comprendre. Le but est aussi d'explorer l'application du GaP / Si aux cellules solaires tandem. La thèse comprend 5 chapitres. Le chapitre 1 décrit l'objectif du travail de thèse et introduit les défauts cristallins dans la plate-forme GaP / Si. Le chapitre 2 présente les techniques de croissance et de caractérisation. Le chapitre 3 est consacré à la caractérisation d'une couche GaP/Si partiellement relaxée plastiquement, à l'échelle globale (par diffraction des rayons X en laboratoire) et l'échelle sub-micrométrique en utilisant une technique à l'état de l'art, de diffractométrie de rayons X à balayage avec une résolution sub-micrométrique. Le chapitre 4

présente une analyse de plusieurs couches CIGS élaborée par CVD sur pseudo-substrats GaP/Si. Ceci met en évidence une croissance de type épitaxial CIGS (001) sur GaP/Si (001). Une première cellule tandem de type « top-top » a ensuite été réalisée. Le dernier chapitre fait la synthèse des résultats et permet d'ouvrir des perspectives.

Dans ce travail, tous les pseudo-substrats GaP / Si sont basés sur des plaquettes de Si (001) de 2 pouces avec un *miscut* de 4 ° ou 6 ° dans la direction [110]. Avant l'épitaxie de GaP, le substrat de silicium est nettoyée avec le « procédé HF optimisé » pour éliminer les impuretés de carbone, d'oxydes, métalliques et organiques à la surface du Si. Après la préparation, la plaquette de Si est immédiatement transférée dans la chambre MBE et chauffée à 800 ° C pour la déshydrogénation. Ensuite, la plaquette est ramenée à plus basse température pour l'épitaxie de GaP. Les méthodes de caractérisation incluent la diffraction des rayons X (DRX), microscope à force atomique (AFM), microscopie électronique en transmission (et à balayage) (SEM, TEM et STEM) entre autres.

Au chapitre 3, nous présentons l'analyse d'une couche de 200nm de GaP/Si avec un angle de coupe de 6° par rapport à la direction [001]. Les propriétés cristallines sont tout d'abord étudiées en DRX en laboratoire et révèlent une très faible densité de micro-macles, grâce à l'optimisation du procédé de préparation chimique. Une relaxation plastique de l'ordre de 50% est ensuite mesurée ce qui est cohérent avec le fait que l'épaisseur critique est de l'ordre de 50 à 90 nm. Une technique à l'état de l'art, développée sur la ligne synchrotron ID01 (ESRF) a été employée pour étudier cet échantillon. Cette technique consiste à balayer, la surface de l'échantillon avec un faisceau sub-micrométrique, au voisinage des conditions de Bragg. Ceci permet d'extraire des informations de complexes de type déformation, tilt et longueur de corrélation locale. Ceci a permis de mettre en évidence une distribution de dislocations dans le pseudo-substrat GaP / Si. L'ensemble de données est analysé à l'aide d'un programme Python appelé « X-ray Strain Orientation Calculation Software (XSOCS) », développé à l'ESRF. [3] L'inclinaison locale $\boldsymbol{\alpha}$ et la déformation locale dans le plan $\boldsymbol{\varepsilon}_{\parallel}$ sont mesurées. La résolution de l'inclinaison locale et de la déformation dans le plan est égale à 0,0036 ° et 0,01%, respectivement.

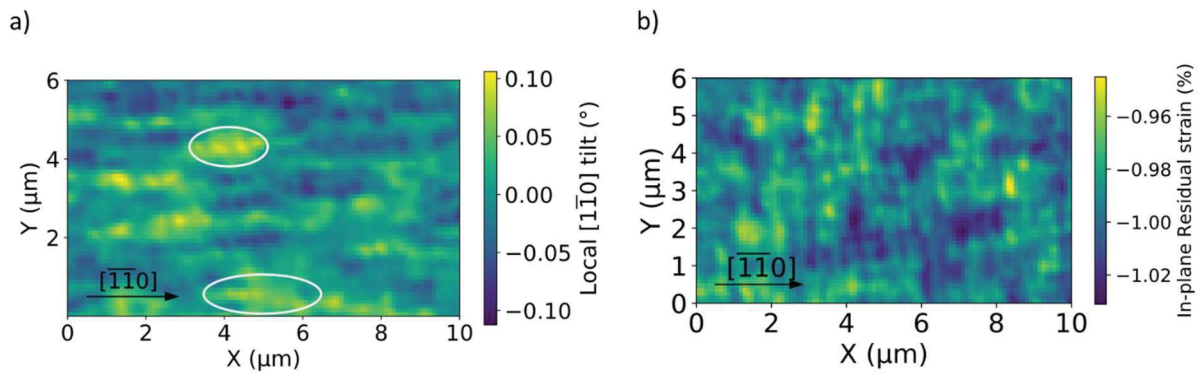


Figure 1 a) Cartographie de l'inclinaison vers la [1-10] et b) Cartographie de la déformation locale (%) à l'aide de la réflexion de Bragg (004).

La cartographie d'inclinaison vers la [1-10] et la cartographie de contrainte locale utilisant la réflexion (004) de Bragg sont illustrées aux figures 1 a) et b) respectivement. Dans la cartographie d'inclinaison, les lignes avec une valeur d'inclinaison élevée sont presque parallèles à [-1-10]. La cartographie des contraintes révèle des lignes à forte contrainte (jaune et vert) parallèles à [1-10] et à [-1-10]. Mais, pour la direction [-1-10], c'est-à-dire la direction perpendiculaire aux bords de marche de la surface du substrat ; les lignes sont moins évidentes et moins parallèles dans la direction parallèle à [1-10]. L'anisotropie de la distribution est très probablement influencée par les terrasses à la surface vicinale du Si.

La déformation locale moyenne dans le plan est de -0,172%, ce qui correspond à une relaxation de 48,2%, proche de la valeur de 50 ± 2% mesurée à partir du la cartographie RSM au laboratoire (représentée à la Figure 2 a)), ce qui permet de sonder une zone beaucoup plus grande de l'échantillon. Une expérience TEM (Figure 2 c)) réalisée sur le même échantillon montre que la plupart des dislocations dans l'échantillon sont de type 60° et que la densité linéaire de 10 $\mu m^{-1}$ correspond (si on considère la même densité le long des autres directions) à un taux de relaxation de déformation plastique d'environ 45%, ce qui est de même ordre de grandeur que les valeurs déterminées à la fois par des mesures de DRX de laboratoire et de sub-micrométrique. Ceci suggère que les dislocations à 60° correspondent aux processus de relaxation principaux.

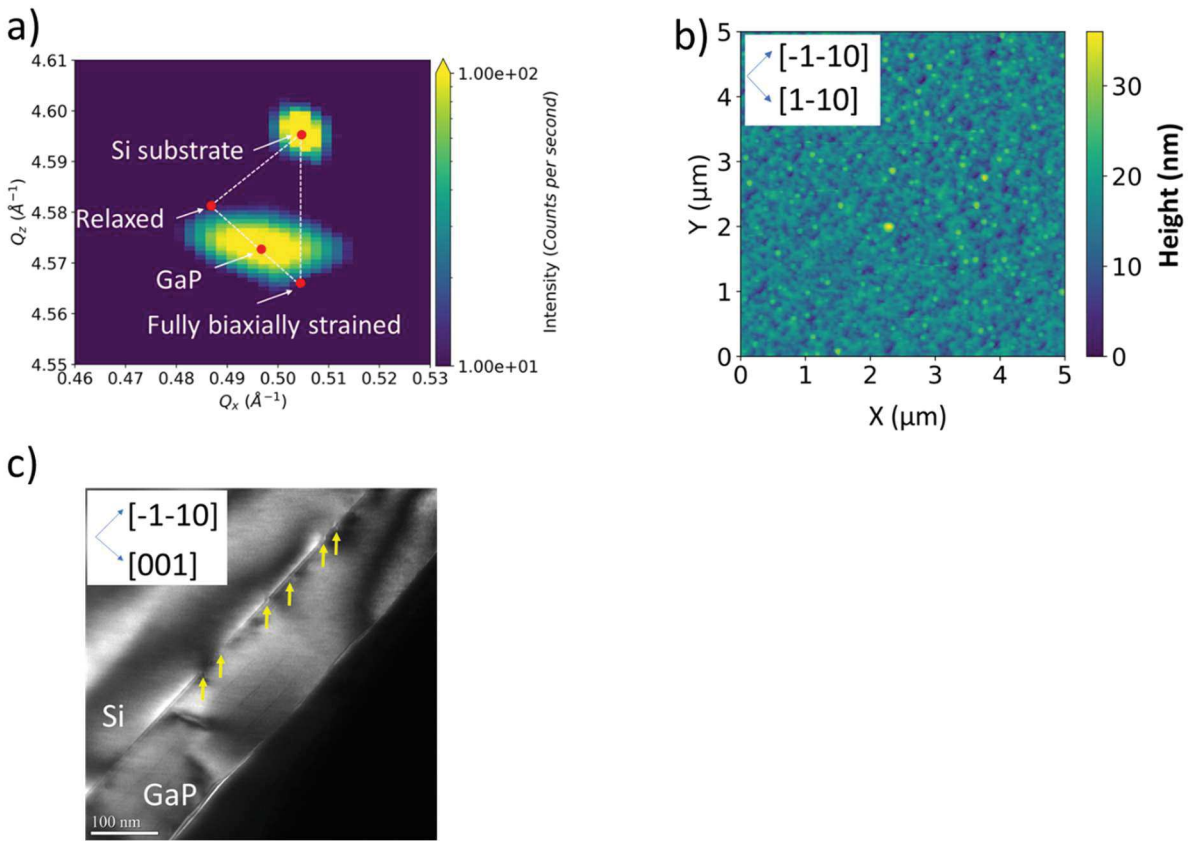


Figure 2 a) Image de la cartographie en espace réciproque de la diffraction (004). b) Image de le microscope à force atomique (AFM) 5µm × 5µm en mode tapotement. c) Image de la microscopie électronique en transmission (TEM) en coupe transversale (220) de champ sombre (DF). Les dislocations de désaccord de maille, sont identifiées par des flèches jaunes.

La cartographie des déformations à l'échelle locale (figure 1 (b)) est filtrée à l'aide d'une fonction de motifs binaires locaux (LBP) La fréquence spatiale des lignes à forte déformation le long de [-1-10] est mesurée à 1,91 µm$^{-1}$. Considérant que la densité des dislocations le long de [-1-10] mesurée par TEM est de 10 µm$^{-1}$, on peut en conclure que la distribution des dislocations n'est pas homogène et que les dislocations à 60 ° sont susceptibles de former des paquets, ce qui est également observé dans les images en champ sombre TEM (figure 2 (c)). L'image AFM (représentée sur la figure 2 b)) mesurée sur le même échantillon est également traitée par transformée de Fourier bidimensionnelle. La fréquence spatiale de [-1-10] est de 1,95 µm$^{-1}$, comme illustré à la figure 3 (b). Ainsi, nous supposons en outre que le réseau de lignes de déformation introduit par les dislocations de désaccord de maille peut avoir un impact sur la morphologie de surface.

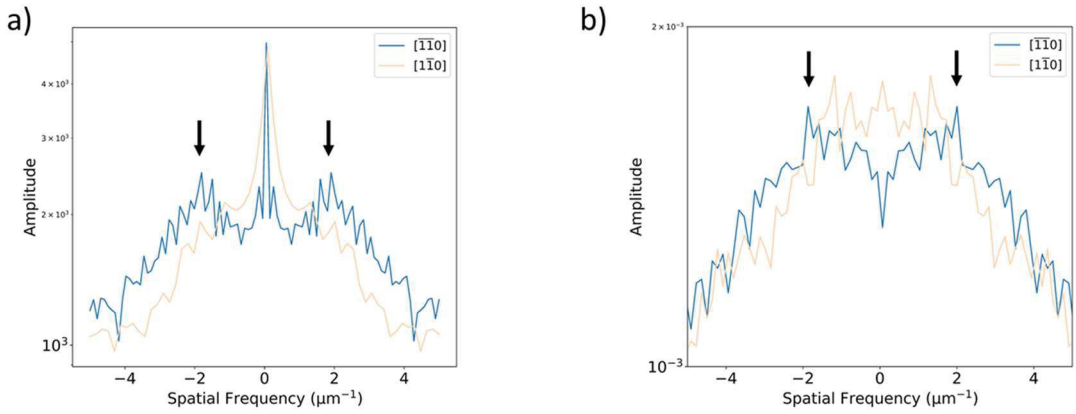


Figure 3 a) Fréquence spatiale des lignes à forte déformation suivant [-1-10] (bleu) et [1-10] (orange) dans la cartographie de déformation et b) Fréquence spatiale de l'image de AFM selon [-1-10] (bleu) et [1-10] (orange).

Au chapitre 4, le CIGS développé sur un pseudo-substrat GaP / Si pour application photovoltaïque est présenté. Cette structure consiste à explorer les jonctions tandem associées à la cellule inférieure en silicium monocristallin, à une bande interdite de 1,12 eV et à la cellule supérieure CIGS, spécialement optimisées pour augmenter l'absorption dans le bleu et l'UV (bande interdite autour de 1,7 eV), avec une approche basée sur l'utilisation de couches de GaP intermédiaires.

Les échantillons utilisés dans cette étude consistent en une couche de Cu ($In_xGa_{1-x}$) $Se_2$ (CIGS) développée sur deux pseudo-substrats GaP / Si (4 ° *de miscut*) différents, et sur du Mo / verre à des fins de comparaison, en utilisant la co-évaporation dans une chambre à haute vitesse de croissance. L'épaisseur de GaP pour les deux échantillons est respectivement de 90 nm (S554) et 600 nm (S597). Les deux pseudo-substrats GaP / Si sont tous deux coupés en plusieurs parties pour mettre en œuvre deux méthodes de dépôt différentes du CIGS, par exemple l'isotherme à 3 étapes (avec recristallisation post-recuit) et l'isotherme à une étape (sans recristallisation).

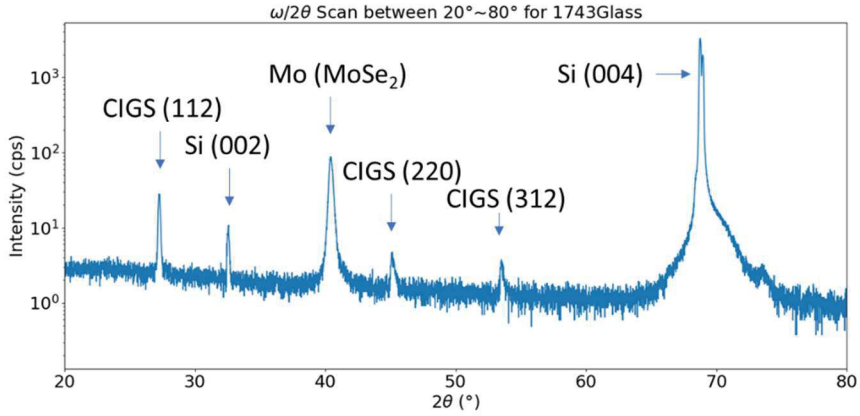


Figure 4 ω / 2θ balayages avec 2θ compris entre 20 ° et 80 ° pour l'échantillon 1743/Glass.

La qualité de l'épitaxie des échantillons est analysée sur la base de balayages ω / 2θ, de cartographies de l'espace réciproque (RSM) et de figures de pôles en DRX de laboratoire. Dans le ω / 2θ, les diagrammes de diffraction des échantillons sur verre présentent les pics de diffraction (112), (220) et (312) du CIGS (illustré à la figure 4), alors que les diagrammes de diffraction de l'échantillon élaboré sur du GaP / Si montrent principalement les pics CIGS (004) et CIGS (008) de Bragg (illustrées à la figure 5), qui révèlent d'une texture de type fortement fibrée ou une épitaxie.

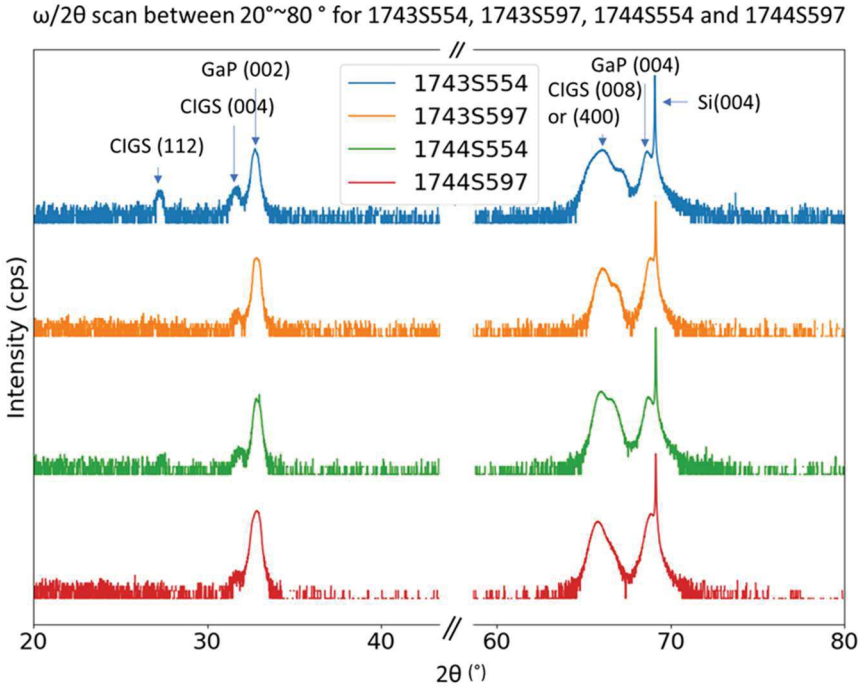


Figure 5 ω / 2θ balayages avec 2θ compris entre 20 ° et 80 ° pour les échantillons 1743/S554, 1743/S597, 1744/S554 et 1744/S597.

La RSM est réalisée autour de la diffraction GaP / Si (115) sur l'un des échantillons de CIGS élaboré sur GaP / Si, comme le montre la figure 6.

L'observation de la diffraction de Bragg CIGS (1 1 10) dans le RSM contenant à la fois le Si (115) et le GaP (115), montre que le CIGS est orienté (008) dans le sens de la croissance.

La croissance épitaxiale du CIGS sur le pseudo-substrat GaP / Si est également illustrée par des images de structure locale par HRTEM et par des figures de pôles, illustrées à la figure 7. Dans la figure de pôles, une diffraction claire en CIGS (112) est montrée, ainsi que les MT formés dans la couche CIGS. Un balayage longitudinal autour de la position du CIGS (112) a confirmé qu'il ne s'agissait pas d'une contribution d'artefact de GaP & Si (111). Le mécanisme de formation a été discuté avec les résultats expérimentaux et basé sur les hypothèses proposées dans la littérature. Les valeurs χ des MT en PF sont calculées comme étant de 15,2 ° et 78,2 °, ce qui correspond bien aux résultats expérimentaux.

Enfin, un premier essai de cellule solaire CIGS sur un pseudo-substrat GaP / Si non optimisé a été réalisé. L'efficacité quantique externe (EQE) a été mesuré pour la cellule solaire CIGS / GaP / Si, puis comparé à une cellule photovoltaïque de CIGS développée sur des substrats de verre

dans les mêmes conditions, comme illustré à la figure 8. La cellule solaire CIGS développée sur Le GaP / Si présente un EQE similaire à celui du verre, dans l'ensemble du spectre de travail. Cela ouvre des perspectives prometteuses pour la future couche développée sur des pseudo-substrats GaP / Si optimisés.

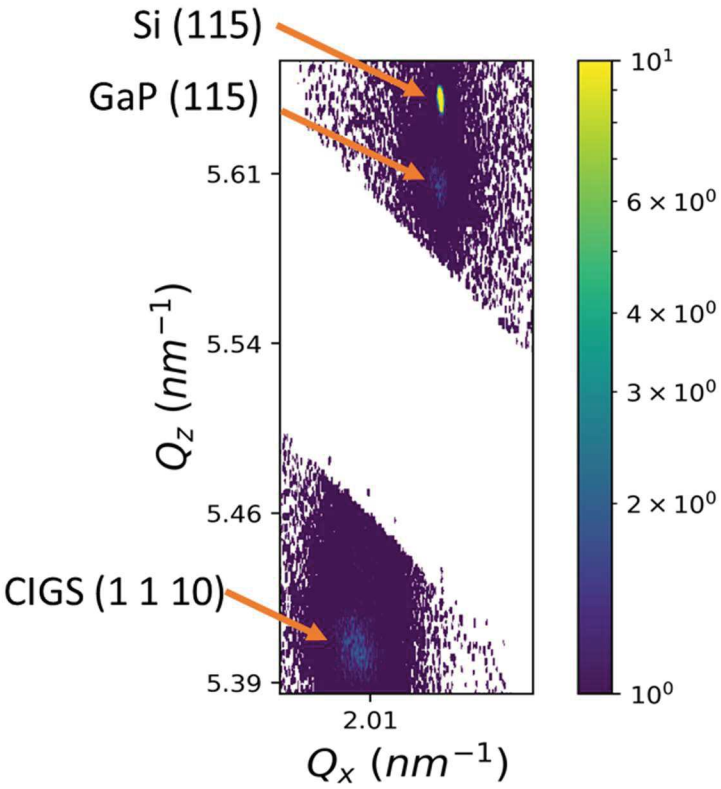


Figure 6 Image de RSM de la diffraction CIGS (1 1 10) et GaP / Si (115).

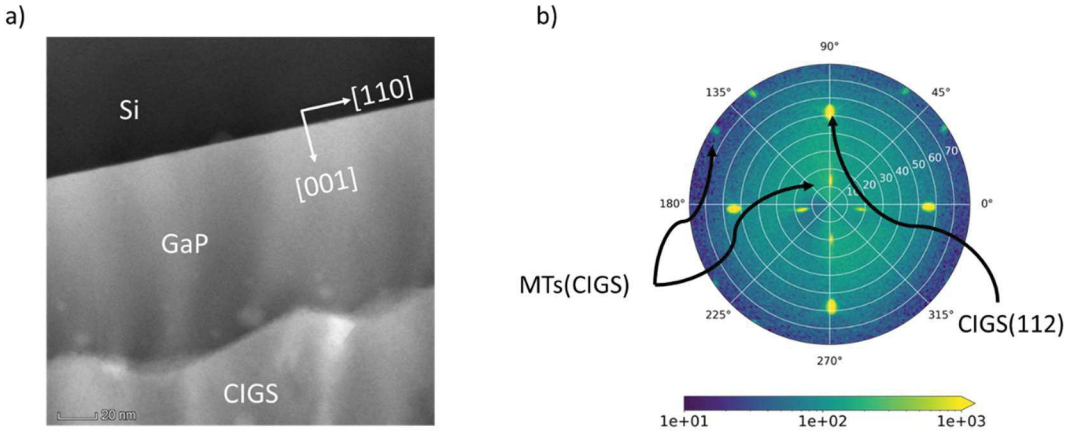


Figure 7 a) Images de TEM de CIGS / GaP / Si b) la figure de pôle de CIGS / GaP / Si, qui montrent une diffraction nette de CIGS (112), ainsi que les formes de formation de MT dans la couche

CIGS. Un balayage transversal autour de la position du CIGS (112) a confirmé que la diffraction n'est pas un artefact de la contribution dûe au raie MT de type GaP (111).

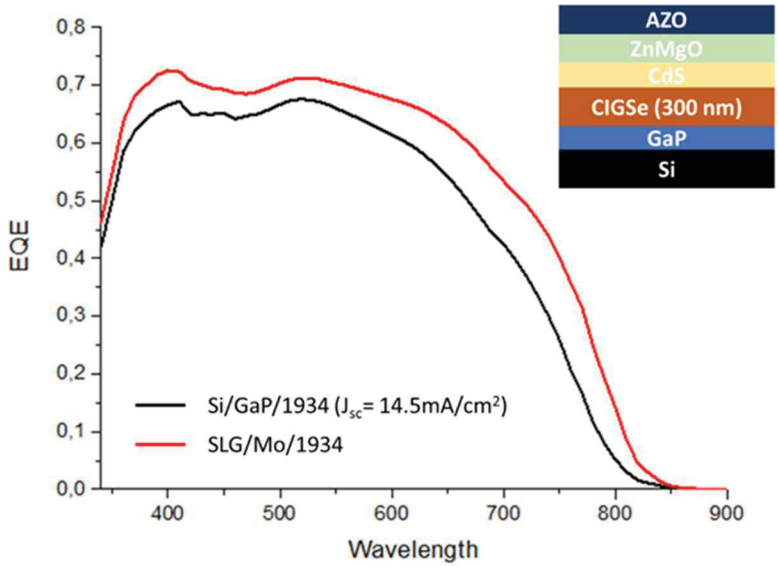


Figure 8 140/5000

Figure 8 Efficacité quantique externe de la cellule solaire CIGS sur un pseudo-substrat GaP / Si non optimisé par rapport à la cellule solaire CIGS sur substrat de verre (Mo).

En conclusion, une nouvelle méthode rapide et non destructive pour quantifier la qualité structurelle locale de la plate-forme GaP / Si avec DRX avec une résolution sub-micrométrique est proposée, qui peut être utilisée pour optimiser les conditions de croissance pour la fabrication. Cette plate-forme est utilisée pour la fabrication de cellules solaires tandem CIGS / GaP / Si, qui explore une voie alternative peu coûteuse dans la fabrication de cellules solaires tandem à haute efficacité. De plus, une combinaison de la DRX avec une résolution sub-micrométrique et d'autres expériences électro-optiques, par exemple la microscopie électronique à balayage, peut en outre révéler l'influence des paquets de dislocations sur les propriétés électro-optiques. La relation entre la mécanique de formation des grappes de dislocation et les substrats vicinaux exige également une discussion plus complète. Enfin, les propriétés électro-optiques des cellules solaires tandem CIGS / GaP / Si avec des conditions de croissance améliorées sont en cours de caractérisation.

Les travaux sur la DRX avec une résolution sub-micrométrique pour la caractérisation de la structure locale sont publiés dans un article intitulé « A study of the strain distribution by scanning X-ray diffraction on GaP/Si for III-V monolithic integration on silicon », J. Appl. Crystallogr., Vol. 52, non. 4, pages 809 à 815, août 2019.

Une autre partie du travail a été présentée lors de conférences scientifiques :

1. A. Zhou, Y. Ping Wang, A. Létoublon, I. Lucci, C. Cornet, V. Favre-Nicolin, G. Chahine, J. Eymery, Y. Léger, M. Bahri, L. Largeau, G. Patriarche, L. Pedesseau, P. Turban, S. Charbonnier, T. Schülli, and O. Durand, « Nano Beam X-ray Scattering on GaP/Si for III-V Monolithic Integration on Silicon », E-MRS 2018 Spring Meeting, June 18 to 22, 2018, Strasbourg, France. Oral presentation.

2- O. Durand, A. Létoublon, C. Cornet, A. Zhou, N. Barreau, M. Balestrieri, D. Coutancier and D. Lincot. « CIGSe growth on a GaP/Si(001) platform : towards CIGS/Si tandem solar cells », Journées Nationales du Photovoltaique 2018 (JNPV 2018), Dourdan, 4-7 Décembre 2018. Poster

3. O. Durand, A. Létoublon, C. Cornet, A. Zhou, N. Barreau, M. Balestrieri, D. Coutancier and D. Lincot, « CIGS growth on a GaP/Si(001) platform : towards CIGS/Si tandem solar cells », E-MRS 2019 Spring Meeting, May 27 to 31, 2019, Nice, France. Oral presentation.

4. O. Durand, A. Létoublon, C. Cornet, A. Zhou, N. Barreau, M. Balestrieri, A. B. Slimane, T. Bidaud, S. Collin, M. Feifel, F. Dimroth, S. Bechu, M. Bouttemy, A. Etcheberry, M. A. Pinault-Thaury, F. Jomard, D. Lincot, « Studies on Si/CIGS Epitaxial Tandem Solar Cells », E-MRS 2019 Spring Meeting, May 27 to 31, 2019, Nice, France. Poster presentation.

5. O. Durand, A. Létoublon, C. Cornet, A. Zhou, N. Barreau, E. Gautron, M. Balestrieri, A. B. Slimane, T. Bidaud, S. Collin, M. Feifel, F. Dimroth, S. Bechu, M. Bouttemy, A. Etcheberry, M. A. Pinault-Thaury, F. Jomard, D. Coutancier, D. Lincot, « CIGS growth on a III-V/Si(001) platform : towards CIGS/Si tandem solar cells », proc. Of the EU PVSEC 2019, 9-13 September 2019, Marseille, France. Poster presentation

INSA de RENNES
Service des Formations

# AVIS DU JURY SUR LA REPRODUCTION DE LA THESE SOUTENUE

**Titre de la thèse:**
Analyse structurales de pseudo-substrats GaP/Si et d'hétérostructures CIGS/GaP/Si pour des applications photovoltaïques

**Nom Prénom de l'auteur : ZHOU ANG**

Membres du jury :
- Madame ESCOUBAS Stéphanie
- Monsieur LINCOT Daniel
- Monsieur BARREAU Nicolas
- Monsieur DURAND Olivier
- Monsieur LETOUBLON Antoine
- Monsieur LE BRIZOUAL Laurent

Président du jury : Daniel LINCOT

Date de la soutenance : 13 Décembre 2019

Reproduction de la these soutenue

☒ Thèse pouvant être reproduite en l'état
☐ Thèse pouvant être reproduite après corrections suggérées

Fait à Rennes, le 13 Décembre 2019

Signature du président de jury

Le Directeur,

M'hamed DRISSI

UNIVERSITE BRETAGNE LOIRE / MATIERE MOLECULES ET MATERIAUX

INSA RENNES

Titre : Analyses structurales de pseudo-substrats GaP/Si et d'hétérostructures CIGS/GaP/Si pour des applications photovoltaïques

**Mots clés :** GaP / Si, MBE, DRX avec une résolution sub-micrométrique, synchrotron, dislocations d'adaptation, cellule solaire tandem.

**Résumé :**
Cette thèse porte sur l'analyse des défauts structuraux d'un pseudo-substrat GaP/Si. L'objectif principal concerne la qualité structurale de la couche épitaxiale de GaP sur un substrat de Si, en tant que pierre angulaire du développement d'une cellule solaire à haut rendement avec des dispositifs optoélectroniques à coût relativement bas et III-V.
Tout d'abord, l'étude porte sur la caractérisation de la distribution des dislocations dans le pseudo-substrat vicinal GaP sur Si(001), à l'aide d'une méthode, appelée K-Map, utilisant la diffusion des rayons X en rayonnement synchrotron et avec une résolution sub-micrométrique. Les informations locales d'inclinaison et de déformation sont obtenues par une analyse de l'ensemble de données complexes 5D.
Cette étude révèle une distribution anisotrope des dislocations dans différentes directions du cristal, liée aux marches à la surface du substrat de Si ainsi qu'une tendance au regroupement de ces dislocations.

La deuxième partie de l'étude porte sur la croissance et la caractérisation de CIGS sur GaP/Si, en vue de développer des cellules solaires tandems associant une cellule du dessous en silicium monocristallin et une cellule du dessus en CIGS. On observe (par XRD, EDX et HRTEM) que le CIGS est déposé par croissance épitaxiale sur le pseudo substrat GaP/Si et présente une qualité structurale proche d'un monocristal. Le premier essai, non optimisé, d'une cellule solaire simple jonction de CIGS sur pseudo-substrat GaP/Si, permet d'obtenir un EQE très encourageant, similaire à celui obtenu avec la même cellule déposée sur substrat de verre avec des paramètres de dépôts optimisés.

Title : Structural analysis of GaP/Si platform and CIGS/GaP/Si heterostructures for photovoltaic applications

**Keywords :** GaP/Si, MBE, Sub-micrometer XRD, synchrotron, Misfit Dislocations, tandem solar cell.

**Abstract :** This thesis focuses on the characterization of the structural defects on a MBE-made GaP/Si pseudo-substrate. The main purpose concerns the structural quality of GaP epitaxial layer on Si substrate, as a cornerstone for the development of high-efficiency solar cell with relatively low cost and optoelectronic devices.

Firstly, the study focuses on the characterization of the distribution of dislocations in GaP on Si (001) vicinal substrate, with an advanced sub-micrometer-beam X-ray scattering method, K-Map. The local tilt and strain information are obtained through an analysis of the complex 5D dataset. This study reveals an anisotropic distribution of the dislocations along different crystallographic directions, linked to the steps of the surface of Si substrate, and an inhomogeneous distribution of the dislocations, linked to the tendency to form bunches.

The second part of the study is on the growth and characterization of CIGS on GaP/Si, which is used to explore tandem junctions associating single crystalline silicon bottom cell. The CIGS is observed to be epitaxially grown on the GaP/Si pseudo substrate, combining the results collected from XRD, EDX and HRTEM. A first try of a CIGS/GaP/Si solar cell is realized on a non-optimized GaP/Si pseudo-substrate. The obtained EQE is similar to the one obtained with the CIGS solar cell grown on a traditional glass substrate with the optimised deposition parameters.